Università degli Studi di Ferrara

DOCTORAL COURSE IN
ENGINEERING SCIENCE

CYCLE XXXV

Director Prof. Stefano Trillo

Advanced Methods for Volumetric Pumps Simulation and Characterization

Scientific/Disciplinary Sector ING-IND/13

Candidate
Dott. Davide Guerra

Supervisor
Prof. Emiliano Mucchi

Years 2019/2022

A Giada, mi hai sostenuto e fatto respirare

ABSTRACT

The Thesis deals with the development of advanced techniques for volumetric pumps NVH and fluidynamic behaviour characterization. The methodologies here presented constitute 3 fundamental tools for the early stages of volumetric machines design or for the implementation of enhancement strategies for existing pumps. Similar approaches represent fast and reliable tools for the evaluation of design strategies, helping the final users to detail the design just for eligible solutions.

In first instance, within the manuscript has been reported a kinetostatic approach to the design of balanced vane pumps equipped with twin lip vanes. Thanks to a deep investigation of the mechanism kinematic, a set of vane geometry admissibility maps has been developed and presented. Such maps have been obtained expressing the kinematic as function of the vane geometrical parameters. The geometrical constraints have been obtained obliging the vane lift law to respect a smooth and continuous motion. Moreover, the imposition of additional constraints, related to the contact loads arising from the pump functioning, gives the opportunity to dispose of a further indicator for the choice of the best vane solutions for a given cam-ring. The residual admissible geometries represent the vanes that reasonably ensure limited contact detachments and consequently proper NVH behaviour and limited lubricant leakages.

In parallel to a kinematic approach, a lumped parameters modelling methodology for the study of the volumetric performances has been presented. Despite such approach might as well be applied to the whole volumetric machines field, within the manuscript the application to gear pumps have been reported. The model has been validated reproducing the operative delivery pressure ripple and flowrate of a tested sample pump. Here, the Bernoulli's equation has been implemented for the continuity equations system resolution, introducing a capillary description of the exchange orifices. The orifices flow parameters tuning has been extensively described corroborating the model reliability and flexibility. With the purpose to reproduce the efficiency gain observed at increasing delivery pressure, the instantaneous shaft bending calculation has been integrated within the model. The validated model has then been deployed for the study of volumetric efficiency enhancement solutions for a helical gear pump. Several solutions have been numerically analysed thanks to the accurate model postprocessing

tool that has allowed to evaluate and resolve local issues and leakages. The most effective solutions have been implemented and the results of the consequent test campaign have confirmed the excellent efficiency improvements suggested by the model.

Aside from the analysis of the internal phenomena, the manuscript also deals with the integration of the machines within the final systems. In particular, the study has been oriented to the investigation of NVH containment solutions. For the scope a portion of a CVT has been studied with particular focus on the integration of the hydrostatic module. The NVH characterization has been performed modelling the system with a finite element approach and implementing a frequency response analysis within an adequate investigation frequency field. The model has been validated reproducing the operative natural frequencies of the system. The postprocessing of the data has been included within the manuscript. The validated model has then been adopted to evaluate the influence of different enhancement solutions. In this context the different design solutions have been implemented by means of concentrated elements. The results of the most effective enhancements have been reported and extensively discussed highlighting the reliability of the model for the design of improvement solutions and for the integration within the early stages of novel systems development.

PREFACE

I have joined the Applied Mechanic and Vibrations research group of the University of Ferrara, leaded by Prof. G. Dalpiaz and Prof. E. Mucchi, in 2018. My experience within the research group has started with an internship for the development of the master degree thesis. Here, I followed the early phases of the design of a multistage gear pump for the feeding of a dry sump lubricating system producing the thesis named *"Progettazione e Simulazione del Comportamento Dinamico di una Pompa ad Ingranaggi per Lubrificazione Motore a Carter Secco"*. I discussed my thesis in March 2019 and I graduated with a 110/110 score. Just after the graduation, I worked within the group thanks to a postgraduate fellowship until November 2019 when I started the PhD course. Since I joined the Applied Mechanic and Vibrations group, I focused my work on the volumetric machines topic with particular attention on gear pumps.

During the first year of my PhD, part of my research has concerned the development of a robust and versatile procedure for the design of gear pumps. I had the chance to deeply investigate the crucial aspects involved into a coherent pump design. Firstly, the strategy for the pump gear design which is extremely different if compared with power transmission gear design. Then, I studied the appropriate dimensions of the clearances between stationary and rotating parts, dealing with volumetric losses and wearing risks. On this topic I published the conference paper [1] and the journal paper [2]:

[1] Davide Guerra, Marco Polastri, Mattia Battarra, Alessio Suman, Emiliano Mucchi, and Michele Pinelli. "A design procedure for multistage external gear pumps." In: *BATH/ASME 2020 Symposium on Fluid Power and Motion Control, FPMC 2020* (2020), pp. 1–10. DOI: 10.1115/FPMC2020-2797.

[2] Davide Guerra, Marco Polastri, Mattia Battarra, Alessio Suman, Emiliano Mucchi, and Michele Pinelli. "Design Multistage External Gear Pumps for Dry Sump Systems: Methodology and Application." In: 2021.March (2021). ISSN: 15635147. DOI: 10.1155/2021/8888128.

This work has represented the base for the development of a lumped parameters (LP) model for the prediction of the performances and pressure ripples

of external gear pumps. The model has been validated by means of dedicated test campaigns.

Within the second year of my PhD, I had the opportunity to apply the LP model to several case studies. Among them, it is worth mentioning the study of volumetric efficiency-improving design solutions in double contact helical gears. The numerical results produced by the LP model have been supported and confirmed by means of a test campaign on improved pumps.

During the third year of PhD, I focused on balanced vane pumps. Since the majority of the balanced vane pumps are equipped with twin lip vanes (TLV), by means of a kinematic approach, I described an analytical procedure for the definition of the admissible TLV geometries. The procedure goal has been the identification of the vanes that ensure smoother motion and reduced contact loads. These aspects are essential to avoid noise, vibration and harshness (NVH) issues and wearing risks. The research carried out on this topic has led to publish the journal paper [3] and the conference paper [4]

[3] Davide Guerra, Mattia Battarra, and Emiliano Mucchi. "Kinematics and geometrical admissibility conditions of balanced vane pumps with twin lip vanes." In: *Mechanism and Machine Theory* 167.August 2021 (2022). ISSN: 0094114X. DOI: 10.1016/j.mechmachtheory.2021.104534. URL: https://doi.org/10.1016/j.mechmachtheory.2021.104534.

[4] Davide Guerra, Mattia Battarra, Emiliano Mucchi, and Giorgio Dalpiaz. "Balanced Twin Lip Vane Pumps: A Kinematic Approach to the Design." In: (2022), pp. 69–76. DOI: 10.1007/978-3-031-10776-4_9.

Furthermore, during the last year, I had the chance to study the evaluation of noise-reducing solutions in an agricultural tractor hydrostatic transmission. With the purpose to characterize the system vibroacustic behaviour, I developed a FEM model where the transmission components, such as casing and gears, have been modelled as 3D meshed solid objects. Then, the connections between hydrostat and adjacent component, such as joints, dampers and rigid connections have been modelled as 0D connectors characterized by their mechanical properties. The coherence of the modelling has been validated reproducing the vibrational signal acquired through operative test campaigns. Then, by means of numerical dynamic analysis, the impact on vibrations and noise emission reduction of several improving design solutions has been analysed and verified.

Apart from my PhD research topics, I also had the chance to deepen the knowledge of bearing tests in automotive field. In particular, I have been in

charge of designing test rigs and test procedures for quality and durability tests on tapered roller bearings. Furthermore, I had the opportunity to perform such tests within the Engineering Laboratory of the University of Ferrara and then to process the data.

This brief summary regarding the work I carried out in the last three years leads me to express a special thank to my advisor, Prof. E. Mucchi, and to Eng. E. Battarra for the precious help they dedicated me throughout this experience.

I would like to sincerely thank the research group mates that shared this experience with me and a particular thank goes to Eng. E. Soave for the helpfulness and support in every moment of this journey.

CONTENTS

LIST OF FIGURES

LIST OF TABLES

ACRONYMS

BE	Boundary Element
CV	Control Volume
CVT	Continuous Variable Transmission
DOF	Degree Of Freedom
DCP	Duality of Contact Point
FE	Finite Element
HM	Hydrostatic Module
LP	Lumped Parameters
NDF	Non dimensional frequency
NVH	Noise,Vibration and Harshness
RFD	Rise Fall Dwell
SEP	Static Equilibrium Positions
SPL	Sound Power Level
TLV	Twin Lip Vanes

1

INTRODUCTION

1.1 IMPROVEMENT STRATEGIES OF VOLUMETRIC MACHINES BEHAVIOUR

The topic of this thesis is the definition of advanced method for the volumetric pump behaviour improvement. Within this context, the term *behaviour* here adopted, does not just refer to aspects related to the elaborated flowrates and pressure but also includes Noise, Vibration and Harshness (NVH) principles, wear phenomena, lubrication aspects. The presented work mainly deals with the study of improvement solutions for gear pumps and balanced vane pumps. Such positive displacement volumetric machines are often equipped within the lubrication systems and are nowadays extensively adopted in the mechanical industry.

The widespread over the years of these type of pumps, has lead the designers to constantly improve the mechanical and fluid-dynamic layout giving to the machines an indisputable reliability. As a matter of facts, reliability, robustness, compactness and apparently simple operating principles are the most recognized key features of these pumps. The question that spontaneously arises from this general overview, may be condensed as: *why do we need further studies on these topics if the technology seems to be as mature as described?*. The answer is that the constant mechanical systems improvement drives the enhancement of the whole constituting components. Considering for example the automotive field, the vehicle electrification has shot down the noise emission and the vibration of the internal combustion engines giving a predominant role to the auxiliary components such as the pumps. In this context, focusing on the volumetric pumps, to further augment the final users comfort, it is mandatory to ensure higher quietness to these machines. On the other hand,

the pursue of the performance improvement may lead to inevitably increase the internal loads between pump components. The result might be a more impacting wearing phenomena with consequent material wastes and additional NVH problems.

The role played by the research in this context is crucial since the implementation of potential enhancements on mature technologies are the harder-to-reach outcomes. The deep knowledge of the mechanical characteristics of the machines represents a mainstay of the study of improvement solutions. In fact, the intrinsic and concealed complexity of the machines commonly leads to dealing with concurrent positive and negative implications of a novel design solution.

Considering the gear pump environment, the increment of the pump performances *e.g.* delivery pressure and delivery flowrate is usually accompanied by an internal loads increment. As a matter of fact, since gear pumps are designed to operate with extremely narrow clearances between rotating and stationary components, the increment of the pump pressurization and the reduction of these gaps are combined phenomena. It descends that a crescent oil entrapment results into the previously mentioned loading upsurge. Furthermore, the gear pump fluid-dynamic is mainly governed by the lateral balancing plates grooves. In particular, the grooves are designed with the purpose to ensure a certain pressurization arc extension and with the purpose to phase the oil release from the delivery to the suction side, within the gear meshing zone.

Focusing on the pump operating principle, the oil suctioned by the gear vain is delivered through the gear rotation from the inlet to the outlet chamber. The lubricant collected among the vain is pressurized along the pressure arc. It descends that the extension of such zone need to be properly tailored in order to both balance the vain pressurization and contain the pressure load. Within the meshing zone, the oil is carried from the high pressure delivery chamber to the inlet generating a pressurized fluid jet. Such phenomena may affect the pump performance and life causing air bubbles that could lead to cavitation issues. Furthermore, during the meshing, the high pressure oil is entrapped between gear vain and the bridge zone of the balancing plates causing a considerable pressure peak. It is worth underlining that the meshing zone phenomena are the main responsible of the pump dynamic effects and noise emission. The dimension of the clearances and of the plate bridge, its timing with the vain enclose, the design of the usually included axial drains, the shape

of the grooves, are all factors involved into the pump performance pursue. Moreover, the effects of these design choices on the pump behaviour are often in conflict. A short pressure arc may lead to contain the pressure load for a limited time, on the contrary, the pressurization and release in a shorter time may introduce dynamic oscillations. Otherwise, a short bridge would limit the pressure peak on the meshing zone but it would also be responsible of ripple increment and suction perturbations. On the same context, it is common to observe that the pursue of a performance improvement is followed by a pressure loads increment originated by the enhanced sealing of the internal gaps. To compensate the collateral effects, a solution would rely on the reduction of the pump rotational speed. In fact, the pump theoretical delivery flowrate is the result of the multiplication of the pump specific displacement for its rotational speed. Then, internal clearances, housing and plates design, tooth profiles and operating conditions are the responsible of the pump delivery flowrate and, consequently, of its efficiency. Thus, the improvement of the internal pump design might allow to achieve the same target flowrate both with a lower pump speed or a reduced specific displacement. It descends that the pump speed reduction may reflect into an attenuation of the dynamic effects, improving simultaneously the NVH behaviour. Within this framework, for the gear pump NVH characteristics improvement the designers have several opportunities to consider. Since the whole dynamic actions within gear pump are phased with the meshing frequency, aside the mentioned balancing plates updates, stronger improvement might be obtained acting on the gear design. Despite the most effective noise sources are recognizable among fluid-borne phenomena, the quality of the tooth surfaces nevertheless remains a crucial aspect to enhance the meshing smoothness containing the vibrational components. Prosecuting in this direction, the adoption of helix gears further helps to ensure quietness to the meshing. Thanks to their smoothness, helix gear pump are widely adopted. As well as for the power transmission field, such pumps are affected by the arising of axial meshing loads and pressure components. In these cases, the forces may be compensated thanks to the balancing plate grooves design which requires more effective compensation chambers. For the NVH improvement, it is then worth mentioning the design of double contact gear pumps. The definition relies on the ability of these machines to ensure a double volume isolation per vain on the meshing zone. This peculiarity allows to split the pressurization reducing the consequent pressure ripples and fluid-borne noise.

This straightforward and generic overview helps to confirm that, despite gear pump are considered simple machines, the implicit design strategy pursued by the designer requires a deep knowledge of the pumps principles.

Similarly to the gear pumps, balanced vane pumps are often considered as straightforward machines with easy to describe operating principles and simple components. However, likewise gear pumps, these positive displacement machines present very complex implication for the design and manufacture of the components.

In general, avoiding strong layout modifications, the increment of the delivery flowrate of these machines is achievable through the increment of the pump speed or with the enhancement of the pump sealing between stationary and in-motion members. As a matter of fact, both solutions are reasonably limited by the magnitude of the internal pressure loads that arise from the pump pressurization. Since the lubricant delivery at a proper pressure is ensured by the ability to isolate and pressurize a oil pocket between two consecutive vanes, the statoric ring and the rotor surface, the deletion of the leakages between vanes and stator plays a key role. It descends that similar results are achievable through the continuous push of the vanes against the stator. Since the pump essentially acts as a cam-follower mechanism, to ensure the continuous action it is worth for the designer to employ the design solution usually suggested for the mechanism. A common layout presents the inclusion of pre-loaded springs under the vanes that constantly exerts the force. Another widely adopted solution is to put into communication the delivery chamber of the pump with the slots where the vanes are located, ensuring an oscillating pressure load that urge the vanes against the stator. It clearly descends that in both cases the contact forces may be responsible of the wearing of vanes and cam ring. Furthermore, the second example suggests that the direct contribute of the delivery pressure on the internal loads obliges to reach a compromise between performances and loads. On the other hand, the spring loaded vanes layout requires the inclusion of more components which may increment the failure risks and the production costs.

From a noise and vibration point of view, the unavoidable delivery pressure ripple generated by the fluid-dynamic turbulence of the vane-to-vane oil pocket delivery is responsible of the fluid borne noise emission. Furthermore, it reflects its fluctuation on the pressure load and, in the end, it is responsible of the contact fluctuation that may generate dynamic effects on the pump

casing. Within this context, in order to minimize other sources of contact fluctuation and for the improvement of the NVH behaviour, it is mandatory for the designer to generate a mechanism eligible of proper motion. The shape of cam ring, the dimensions of the rotor, the dimension and the shape of the vanes are all aspects that concur to give to the mechanism a certain kinematic. As previously mentioned and further detailed within Chapter 2, vane pumps need to be considered as cam follower mechanism. Ensuring to the mechanism a proper kinematic represents the base of the design of a good pump which needs to be integrated with proper design of side plates, grooves and inlet or outlet ports that affects the fluid-dynamic behaviour. A coherent kinematics ensure the regularity of the motion without vane detachment risks, acting also as a sealing enhancement strategy. At the same time, the study of vane solutions that allow to reduce the contact loads represents a reliable strategy to improve the NVH pump behaviour. In particular, the twin lip vane design gives the chance to neglect the pressure loads components thanks to balancing bores machined among the vane lips and simultaneously allows to smooth the radial contact action widening the contact pressure angle.

Focusing on the volumetric machines improvement, the overview shows that the designers may choose among a wide spectrum of solutions and reliable tools. Despite the pump design may lead to achieve satisfactory performance and dynamic effects containment, the subsequent integration of the pump into articulate mechanical systems may lead to unpredicted issues. As it happens, the excitations arising from pressure and loads ripples of the pump, are then transferred to the machine casing. With the purpose to avoid the excitation of structural resonance frequencies, the designers are called to provide to the casing a coherent shape with dedicated study. The integration of computational modal analysis among the design phases are nowadays a mandatory requirement. The robustness and reliability of the available numerical tools allows to avoid, at least, the structural-borne emission of the machines. Thus, such machines needs to be integrated into the final mechanical systems. Here, the connections of the pump, if is not properly designed, transfer the vibrations arising from the pump operating to the whole system. The risk connected to this, essentially relies on the probability to excite the natural frequency of one of the system components, which increases in parallel with the number of components. The results of this occurrence may include annoying vibrations or noise for the end users but also unforeseen failures due

to fatigue phenomena. In sight of this possible scenarios, it is then mandatory for the designers to have a clear overview of the system and possibly implement numerical models for the monitoring in the early phases.

It descends that having validated finite element (FE) or multibody models represents a key aspect on the design of novel systems or for the implementation of existing system enhancements. Such models let to evaluate the vibrational modes of the integrated system, the response to statics loads and, most important for the NVH field, the response to dynamic actions. Citing some of the possible implications of the adoption of numerical reproductions, the results may guide to the introduction of dampers for the attenuation of the excitation coming from specific components or to the strengthening of connections. In addition, it allows to evaluate different materials for the components, may also suggest the variation of the components placement to better respond to excitations.

Concluding this preliminary and general dissertation on the volumetric machines design process, it is worth to further underline that introducing enhancement or designing *ex-novo* solutions requires a deep knowledge of the topics and the research in this field constantly acts a primary role. The ongoing product and process optimization rush requires sustainability and low impact features that prevent as much as possible undesired issues. Within this framework, the development of sophisticated, robust and reliable techniques for the numerical treatment of the design issue represents a need that can not be ignored by the nowadays industry.

1.2 OVERVIEW OF THE THESIS

The presented manuscript has been developed with the purpose to respond to the implications detailed within the previous section. The dissertation follows the framework of the introducing section presenting different approaches for the improvement of different volumetric machines behaviour. In particular, two chapters are dedicated to the study of pumps enhancement solutions acting on the design of the internal parts of the machines. Otherwise, the last chapter deals with the NVH improvement of the system where a volumetric machine is integrated. To address the investigation of the phenomena involved within the different activities, different techniques have been implemented. For the study of vane pumps design strategy, an analytical kinematic based

numerical model have been implemented. On the other hand, the analysis of gear pumps has been carried out thanks to the development of a validated lumped parameter (LP) model. The tool has proven to be reliable both for the reproduction of existing pump behaviour and for the prediction of novel models performances. A validated FE model has been then implemented for the analysis of the interactions between an hydrostat and the connected system components.

The study on the vane pumps kinematic has been included within Chapter 2. In particular, with the purpose to develop a reliable tool for the early stages of pump design, the dissertation deals with the implications of the twin lip vanes equipment on balanced vane pump. The first part of the Chapter is devoted to the description of the operating principles of the balanced vane pumps with a particular focus on the differences that arise using twin lip vanes instead of traditional circular single lip vanes. It highlight that the particular lip design ensure the possibility to include balancing bores that drastically reduces the radial contact loads between vanes and cam ring. Then, the study of the kinematic of the cam-follower mechanism associated to the vane-cam ring system has been included with the purpose to deeply comprise the vane motion. Within this content, the description of the kinematic rings through the vane geometrical features, leads to obtain the kinematic-based geometrical constraints. Furthermore, keeping the reference to the geometrical parameters, the analytical model deals with the description of the loads that affects the vain. This lead to define further constraints to the admissible geometries.

The assessment of the analytical dissertation has been performed implementing a numerical study, included in the second part of Chapter 2. The model additionally allows to define the twin lip vanes admissibility map for a given cam ring family. A particular mention goes to Section 2.5.3 which has been reserved to the description of the pre-compression cam ring layouts. Here, two method for the enhancement of the pre-compressive profiles are included showing the relative admissibility maps. The last part of the chapter has been dedicated to the implementation of the loads calculation for the admissible vanes. The study provides the characterization of the influence of the vane geometry on the radial loads giving the opportunity to have an indicator of the dynamic behaviour in the early stages of the design.

As mentioned, the study of the kinematic helps to identify potential sources of volumetric efficiency drop and avoid it discarding the geometries responsible

of such negative implications. Despite the methodology acts a fundamental role especially in the early stages of the design, there are several advanced techniques that may be integrated to better describe the pump behaviour. In particular, within the manuscript the lumped parameter approach has been discussed and implemented for the reproduction and prediction of the performances of volumetric pumps. In particular, Chapter 3, that represents the major section of the manuscript, deals with the description of the LP model developed for the analysis of gear pumps performance in terms of pressure ripples and volumetric efficiency. It is worth underlining that the approach might as well be applied to the whole volumetric machines population such as vane pumps or piston pumps giving satisfactory results. The model has been implemented and validated with the purpose to dispose of a reliable and accurate tool that permits to evaluate the influence of different design solutions on the pumps behaviour. The initial part of the Chapter is devoted to the illustration of the novelty aspects of this LP model with respect to previous versions. In particular, despite the model follows the previous iterative scheme for the resolution of the continuity equation, it includes a different method for the flowrate calculation. The method, avoiding the *a priori* imposition of the flows nature, ensures a smooth transition from turbulent to laminar flow and vice-versa. The shift is ensured by the flow numbers and flow coefficients included within the Bernoulli's formulation of the flowrate. The pump internal orifices subjected to lubricant exchange between control volumes have been characterized through proper values of these coefficients, accurately tailored in the validation phase. The result is an improved accuracy and stability of the simulation outcomes. The validation procedure, performed on a spur gears pump, has been included within Section 3.5. Then, the potentialities of the tool have been deployed through the application on a performance improvement study carried out on a helical gear pump. Within Section 3.6, is included the benchmark pump characterization, the improving solutions study with numerical results and finally the comparison with the experimental data of the suggested design improvements. Within the section devoted to the description of the proposed enhancement solutions, it is possible to have a demonstration of the monitorable phenomena with the proposed LP model. The final part of the Chapter includes the description of the gear design tool that constitutes the basis of the LP model. In addition, is here reported a comprehensive design

procedure that guide the design of a novel gear pump and might be integrated with the simulation tool.

Despite the first two Chapters have presented studies that deal with the representation of the internal phenomena of the machines, highlighting the implementation of advanced techniques for the prediction of pump performances, it is mandatory to investigate also the integration of these machines within the final systems. Chapter 4, unlike the previous two, deals with the implementation of novel investigation methodologies for the improvement of the NVH behaviour of the systems where the volumetric machines are integrated. It deals with the study of NVH improvement solutions for an agricultural hybrid continuous variable transmission (CVT). In particular, since the CVT systems integrates an hydraulic module, constituted by two axial pistons machines, with the mechanical transmission, the characteristic dynamic excitation of the hydrostat are usually responsible of the increment of the noise and vibration levels. The activity has been carried out considering the hydrostat as a black box connected to the frame of the driveline and then closed by a cover plate. The connections of the hydrostat have been modelled by means of 1D elements, properly tailored to reproduce the system vibrational behaviour observed in a dedicated test campaign. The validation of the FE model has allowed to use it for study of NVH improvement solutions such as the introduction of dampers or the increment of connections stiffness.

The concluding Chapter has been devoted to final remarks. For sake of clarity, a dedicated nomenclature section has been included within each Chapter avoiding redundancy of subscripts and articulate characters.

2

A KINEMATIC APPROACH TO THE DESIGN OF TLV BALANCED VANE PUMPS

The chapter presents a kinematic based study oriented to the definition of the TLVs design boundaries for a given cam-ring. The study has been carried out considering the vane pump as an inverse cam-follower mechanism. While the body of the pump represents a statoric cam-shaped ring, vanes are considered as followers with two symmetrical half-circular tips. Vanes are characterized by a tern of geometrical parameters such as tip radius, lip eccentricity and vane half width. Through the definition of the kinematic ring equations, the explicit form of the vane geometrical constraints have been formalized. Such approach allows to identify kinematically admissible TLVs discarding incoherent geometries. With the purpose to define a set of vane geometries capable of adequate NVH behaviour, the TLVs are subjected to the fundamental law of cam design which dramatically reduces the admissibility domain. Moreover, the study deals with the analytical definition of the radial loads acting on the vanes. The goal is to avoid from the domain the vanes that are affected by detachment risk or by localized contact load peaks possibly responsible of uncontrolled wear phenomena. The proposed study also includes an extended dissertation over the opportunity to introduce pre-compression zones along the cam ring in balanced vane pump equipped with TLV. Vane admissibility domains have been extrapolated for a given cam ring, through the application of a numerical approach. Such domains have also been presented for pre-compressive cam ring.

2.1 CHAPTER NOMENCLATURE

Latin symbols

A	frontal vane surface
c	damping coefficient
d	vane lip eccentricity
$\hat{e}$	ratio between maximum and minimum cam ring radius
f_c	centrifugal force
f_k	contact force
h_v	vane lip half width
H	vane height dimension
m	mass
r_c	radius of the vane circular tip center
r_G	radial position of vane center of gravity
r_s	cam ring radius
r_v	vane circular lip tip radius
$r*$	radius of the inactive hypothetical point of contact
R_θ	vane lift radius
$\hat{V}$	pump specific displacement
W	gear facewidth
x	distance between vane center and contact point
z_b	number of vane balancing bores

Greek symbols

α	angular span between contact point and lift radius
β	pressure angle
γ	contact point angular coordinate
δ	angular span between contact point and vane lip center radius
Φ	diameter of balancing bores
Θ	angular free coordinate
ρ	oil density

ξ	pre-compression ratio
ψ	angle of the tangent to the contact point
ω	angular speed

Subscripts & superscripts

a, b, c	denote different sub-areas of the vane frontal surface
r, l	denote right or left vane kinematic ring, respectively
lim	denote the limit existence value
G	denotes dimension referred to the center of gravity
v	denotes dimension referred to the vane
$1, 2$	denote the distinct 2^{nd} order equation solutions

2.2 INTRODUCTION

The adoption of vane pumps in lubrication systems is consistently increasing thanks to their compactness, robustness and good performances combined with a characteristic low noise emission compared with other volumetric machines. According to Neukirchner et al. [5], vane-type oil pumps combine the higher values of displacement and mechanical efficiency with respect to compactness, within the context of positive displacement machines. In addition, they typically ensure low noise emissions as a consequence of a small amplitude flow ripple and reduced mechanical loads. Taking into consideration the automotive field, the progressive substitution of combustion engines with the more smooth electric units, has emphasized the noise emission of auxiliary components. Consequently, the designer have been called to answer to the request of contain the noise emission of such components. Within this framework, considering the relevance assumed by such volumetric machines, several studies are nowadays arising with the purpose to characterize the machine operating principles and consequently improve efficiency and smoothness.

From a dedicated literature survey, arises that Kojima et al. in [6] proposed one of the first theoretical study of the fluid-borne noise emission. From this work, the strict correlation between flow oscillations and noise. On the other hand, one of the earliest numerical models developed for the prediction of flow ripples has been presented by Seet et al. in [7]. The tool was validated by

a test campaign and was adopted for the estimation of the potential benefits of silencing grooves on pump plates sides. The grooves play a fundamental role in vane pump allowing to reduce the flow ripple amplitude with great impact on the fluid-borne noise containment. Following an analogue strategy, authors in ref. [8] developed a novel numerical model for the design of a small-ripple pump cam ring. the study suggests that controlling vane velocity it is possible to reduce the number of vanes containing the pressure fluctuation. Later, Nakamura et al. in [9] presented a validated mathematical model for the delivery pressure ripple description, which included the effects of leakage flows on pressure ripple. The model was further improved by Inaguma and Nakamura in [10]. Afterwards, Dickinson et al. in [11] introduced the Secondary Source Method for the experimental measure of the fluid-borne noise in balanced vane pump. Thus, the method has been adopted by Jones et al. in [12] for the validation of the proposed numerical model for the prediction of suction flow ripples and consequential noise emission. Within the experimental field, Mucchi et al. in [13] developed advanced and robust experimental methodologies for pressure ripple measurement within the pockets of vane pumps. As well as for other volumetric machines, the literature shows methodologies for the performance estimation based on CFD. Lobsinger et al. in [14] presented a CFD approach to analyse leakage flows and to provide an estimation of the volumetric efficiency. Within this field, is worth noticing the work presented by Hyeronimus et al. in [15] where FEM and CFD approaches are combined to identify the correlation between structural-borne noise and flow ripple.

In parallel with the noise and performance characterization, authors developed methods for the study of the contact between vanes and cam ring. Similarly to other volumetric machines, with the purpose to increase the volumetric efficiency, balanced vane pumps are required to reduce the internal leakages between moving parts. The major responsible of the internal leakages is the clearance between vane and cam ring, where the pressurized oil flows toward the lower pressure chambers of the pump. Despite the centrifugal action of the rotor pushing the vane outward the pocket helps to reduce the leakage, the complete sealing effect is achieved by the application of an additional radial load to the vane. Such force might be applied by means of a pre-loaded spring or directly by the pressurized oil, both located within the under-vane pockets. Watton et al. in [16] correlated pressure loads and flowrates with the cam ring profile by means of a mathematical model, including the effects of

the pre-compression zone on pump internal loads. Within ref. [17, 18], the motion of the vane, the loads applied and the efficiency losses due to the vane detachment from the cam ring have been deeply investigated. As a matter of fact, the vane forcing against the stator generates unavoidably wear phenomena. Within this framework, Kunz et al. in [19] presented a theoretical study of the contact between vanes and cam ring with the purpose to predict wear problems in vane pumps. The study was supported by a test campaign described in [20]. For the same purpose, alternative vane designs have been developed and extensively spread through the years [21], e.g. splitted vanes, intra-vanes mechanism or twin lip vanes, however, the literature lacks in the characterizations of such solutions.

As well as volumetric efficiency, mechanical efficiency has been investigated by scientists and the main influence factors have been characterized. Inaguma and Hibi in [22] outlined the strong correlation between mechanical efficiency and vanes width. In addition, the same authors in [23] described the influence of the cam ring inner surface roughness on friction torque arising from vane tip and cam contour. Later, Inaguma et al. in [24] analysed the effects of the number of vanes on friction torque. On the other hand, within [25] the wearing phenomena and the tribological behaviour of pump components in contact, have been evaluated by means of a test campaign. Wang et al. in [26] studied the incidence of the oil film between vane and cam ring on the mechanical efficiency identifying the influence factors on the oil leakages. All these studies led to support the idea that thinner vanes and a high quality of the cam ring surface contribute to reduce friction forces and torque with direct benefits on mechanical efficiency. In addition, a lower number of vanes reduces the mean value of the friction torque while the ripple is amplified.

This brief literature survey, despite not entirely comprehensive of the overall amount of studies on balanced vane pumps, demonstrates how the majority of the research has been focused on the estimation of the performance of the machine, mainly in terms of volumetric efficiency, mechanical efficiency and NVH behaviour. In parallel with this trend, during the last decade research started focusing the attention also on such machines as linkage mechanisms, detailing its kinematic features and design properties. In this scenario, Giuffrida et al. in [27] presented a theoretical dissertation of the cam ring design and its influence on the pump flow ripple. Following the same trend, Battarra et al. in [28] detailed the kinematics of balanced vane pumps in the common

configuration of circular tip vanes. The work outlined the crucial influence of the vane geometrical parameters on the vane motion. In addition, the paper presents a design guideline defining the kinematic admissibility of vanes for a given cam ring profile. Later, Battarra and Mucchi in [29] dealt with the kinematic flow ripple in balanced vane pumps with single circular tip vanes, discussing the influence of the vane geometry on the oscillation of the flow rate. Furthermore, the vane geometry has been shown to affect the pressure radial loads as stated in Ref. [30] by the same authors.

According to this last branch of investigation, the specialized literature is still not widespread to the large variety of machine configurations available in the actual market, since specialized papers focused exclusively on balanced vane pumps equipped with single tip vanes in squared shape [27] and circular shape [28]. Based on this background, the aim of the present work is the formalization of the kinematics for balanced vane pumps equipped with twin lip vanes. Their peculiar design provides the chance to reach high delivery pressure values without overloading the vanes against the cam ring. For this reason, these machines find prevalent adoption in heavy-duty applications, where reliability represents the fundamental characteristic of such pumps. Despite widely popular and mentioned in the book Ivantysyn J. and Ivantysynova M. in Ref. [21], a detailed analysis of their design properties is not available in the literature. On the basis of these considerations, this study investigates the consequences that the adoption of twin lip vanes produces on the kinematic behaviour of the machine, with the purpose to provide design guidelines regarding the choice of the vane design parameters. The duality of the point of contact between vane and cam ring is deeply analysed as well as the transition of the point of contact when switching from the rise/fall phase to the dwell phase. Admissibility limits on the vane geometry are analytically deduced by the machine kinematics and they are intersected with restrictions based on the fundamental law of cam design [31]. The procedure provides the set of vane geometrical parameters that guarantee a kinematically consistent working behaviour. It is worth clarifying that the main goal of the present work is the definition of tools that can help designers in determining the mechanical properties of the mechanism, such as the correct choice of the vane geometry in order to obtain a conforming contact with the cam ring profile. Based on this purpose, results will not involve considerations regarding the fluid-dynamic performance of this machine category, even though the

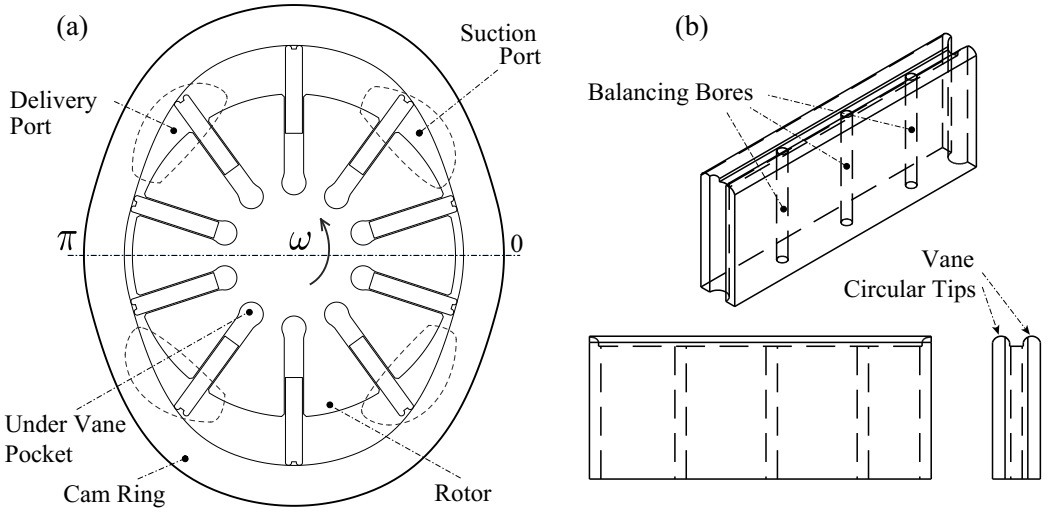

Figure 1: Representation of a generic balanced vane pump(a) and a detailed view of a TLV with circular tips(b)

proposed kinematic laws may be considered as preparatory to the definition of numerical models focused on the prediction of pump leakages, delivery flow rate ripple and delivery pressure ripple. Similarly, the obtained equations may be straightforwardly implemented in the procedure described in ref. [29] to calculate the theoretical flow rate ripple associated to twin lip vanes. On the other hand, with the purpose to fulfil the description of the TLV admissibility domain, the analysis of the loads acting on the vane has been formalized and discussed. Within this framework, the design tool assumes a crescent relevance thanks to the opportunity to compare different vane designs in terms of motion regularity and in terms of arising loads during the pump operating.

2.3 OPERATING PRINCIPLE OF THE BALANCED TLV PUMPS

As mentioned within previous Chapter, balanced vane pump are reliable volumetric machines, constituted by a limited number of components, working in a fairly simple way. However, an exhaustive brief description of such machines would be necessary to deal with the proposed study. A balanced vane pump is essentially constituted by an external stationary casing, namely the cam ring,

and an internal cartridge. Figure 1(a) reports a schematic frontal view of a generic balanced vane pump which helps to identify the main components.

The cartridge consists into a central slotted rotor and a discrete number of vanes, housed into the slots. Since the rotor is put in rotation, the vanes are urged outward their slots by the centrifugal action. Furthermore, the pockets under the vanes are always filled with pressurized oil which actively contributes to force the vanes against the pump casing. With the purpose to drive the vanes to describe a certain trajectory during the cartridge rotation, the casing is internally shaped as a cam profile. From a kinematic point of view, the casing acts as a cam while the vanes represent the mechanism followers. Concurrently, the cam profile needs to be designed in order to ensure proper pump displacement and pressurization to the oil bounded by consecutive vanes. In addition to the components outlined within Figure 1(a), vane pumps are closed by means of two lateral plates where are located the suction and delivery ports.

The operating principles of a balanced vane pump might be easily described following an entire rotor revolution. As primary step, the oil is suctioned through the inlet port. Here, two consecutive vanes in contact with the statoric cam ring, bound an oil pocket and guide it along the cam ring profile. This first phase is named rise phase because the vanes tend to exit from the rotor pockets following the cam profile. The trapped oil volume tends to expand during such phase. Thus, the case profile tends to decrease its radial dimension generating a convergent profile. Here starts the precompression phase where the pocket volume decreases pressurizing the bounded oil. Finally, the rotor guides the consecutive vanes in the delivery zone where the oil is drained through the outlet port during the cam ring fall phase. In order to ensure the machine radial balancing and a higher pump efficiency, the pumping process is simmetrically repeated twice per revolution.

Along the entire pumping process, the vanes are continuously forced against the inner profile of the cam ring thanks to the centrifugal action generated by the cartridge rotation. This behaviour, that is mandatory to guarantee the tangential sealing between the oil pockets, is further promoted by the radial load arising from the pressurized oil located in the under-vane pockets, which usually reaches pressure values close to the delivery pressure. In particular, according to the analysis in Ref. [30], this term overcomes the centrifugal force by some orders of magnitude as the pump speed decreases and the

delivery pressure increases. This characteristic represents a critical aspect for the structural design of the pump, since the overall radial load applied to the vane determines the contact pressure between the tip of the vanes and the cam ring profile. Therefore, on one side, the vane radial load should be enough to guarantee the sealing between pockets and, on the other side, it has to be limited in order to reduce wear and surface fatigue related phenomena. As an example, this is the common scenario for heavy-duty applications, in which the pump is designed to work safely at low speed an to provide hundreds of bars regarding the pump head.

In order to achieve this purpose, the standard design of circular tip vanes is overcome by the adoption of twin lip vanes, which are described by the schematic in Fig. 1(b). As it may be recognized, twin lip vanes are constituted by a double circular tip producing a small pocket between the vane tip and the cam ring. This pocket is hydraulically connected to the under vane pocket by means of balancing bores, neutralizing the pressure force acting on the vane along the radial direction. As a final results, the vanes are maintained against the cam ring by the exclusive contribution of the centrifugal force and the contact pressure is limited to acceptable values with no dependence on the pump head. Despite the balancing of the pressure radial load constitutes the main objective of this design solution, the modification applied to the vane tip with respect to the standard design given by the circular tip vane produces consequences also on the kinematic properties of the mechanism.

2.4 KINETOSTATIC ANALYSIS OF THE VANE-CAM RING MECHANISM

According to Ref. [28], a balanced vane pump is an inverse cam-follower mechanism where the stator represents a fixed cam and every single vane acts as a rotating follower. The cam profile is shaped in order to assign to the vane the motion that guarantees the desired pumping action and, in general, such a motion may be described by a rise, fall and dwell law, hereinafter named as RFD law, as the one reported in Fig. 2.

In agreement with this considerations, Figure 3(a) reports the conceptual representation of the pump mechanical linkage, where the two circles pertaining to link #2 describe the two characteristic rounded tips of twin lip vanes, while link #1 represents the rotor and link #3 is the cam ring. The mechanism is outlined as a singular degree of freedom (DOF) mechanism where the angular

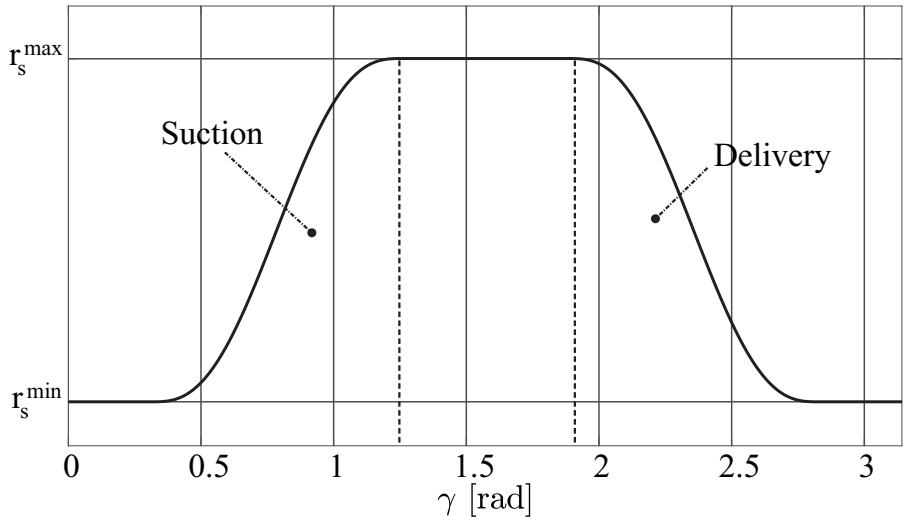

Figure 2: Generic representations of a cam ring profile on a Cartesian plane

position of the vane θ represents the unique free coordinate. For the purpose of the dissertation, the vane is provided with two circular tips with same radius, spaced from the vane axis by the same eccentricity value.

Figure 3(b) shows the kinematic rings which may be described for a singular contact point. Such condition is a TLV characteristic which arises from the presence of equally spaced tips. For a given angular coordinate θ the vane is forced against cam-ring reaching a coherent vane lift described by the radius R_θ, comprehensive of the rotor radius and the vane displacement. From a mathematical point of view, it is absolutely admissible to generate two specular kinematic rings connecting the rotation center O to the hypothetical contact point P. As it may be easily deduced, this design introduces a problem of duality of contact point (DCP). The point P might lay on one lip or the other (or both) depending on the linkage position. Based on this observation, according to Fig. 3(b), two analogous but distinct closure equations may be defined for each vane angular position, one referring to the right lip and one referring to the left lip:

$$\begin{cases} R_\theta e^{i\theta} + d e^{i(\theta-\pi/2)} + r_v e^{i(\theta+\beta_r)} = r_s(\gamma_r) e^{i\gamma_r} \\ R_\theta e^{i\theta} + d e^{i(\theta+\pi/2)} + r_v e^{i(\theta+\beta_l)} = r_s(\gamma_l) e^{i\gamma_l} \end{cases} \tag{1}$$

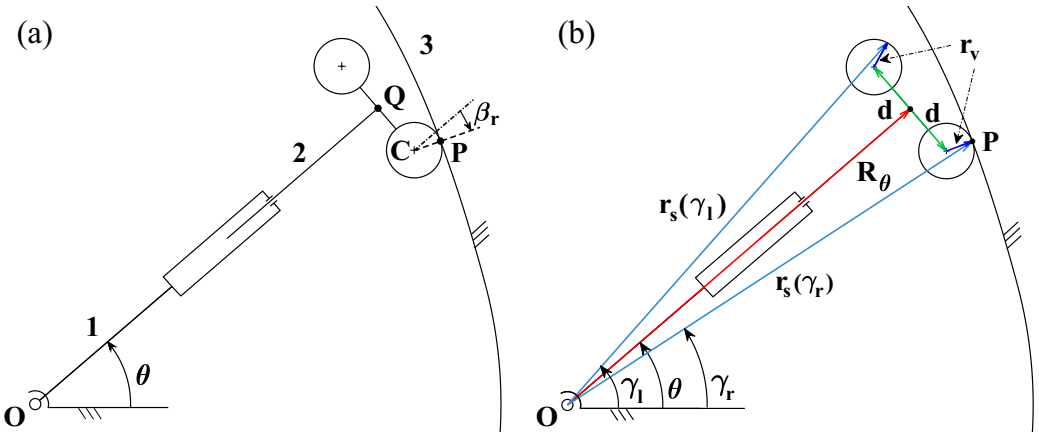

Figure 3: Equivalent mechanical linkage representing the twin lip vane-cam ring mechanism (a) and schematic representation of the closure equations of a single TLV (b)

where d is the vane eccentricity, r_v is the tip radius of the vane lips and term β represents the pressure angle, i.e. the angle between R_θ and the normal direction with respect to the cam ring profile tangent in *P*. As a consequence of the duality of the contact point problem, β is distinguished for the right lip as β_r and for the left lip as β_l. Finally, parameters γ and r_s are the angular and radial polar coordinates of the contact point, respectively. It has to be underlined that the unknowns for each closure equation are represented by lift radius R_θ and pressure angle β_r or β_l, respectively, meaning that the designer is interested in determining the follower motion while the cam profile is give within the input data. This objective constitutes a reversal of the classical point of view characterizing the cam design, where the follower motion is an input data and the cam profile needs to be obtained. Due to the defined approach, it is not possible to define a priori whether both correlations in the system in Eq. 1 admit a solution. As an example, it is possible to refer to Fig. 3, where the contact point lays on the right vane lip exclusively. In this configuration, the second line in Eq. 1 does not provide physical solutions.

With the purpose to find a solution to DCP issue and to provide an analytical solution to the closure equation, it is fundamental to deeply investigate the geometrical connection between the involved members. A crucial role in the definition of the vane kinematics is played by the pressure angle β. As a matter of fact, an explicit formulation of β gives the opportunity to identify which

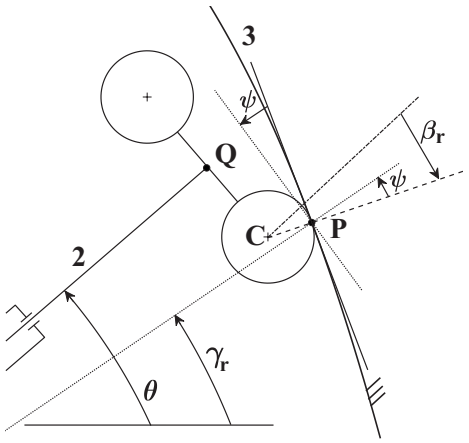

Figure 4: Focus on the relationship between the characteristics angles on the contact zone

kinematic ring is eligible solving the DCP problem. Exploiting the geometry of the given cam ring, arise that is possible to correlate the vane angular position to the pressure angle. The lift angle of the cam ring profile at contact point P might be calculated performing the derivative of cam ring radius r_s with respect to its angular coordinate γ as follow:

$$\psi|_P = \tan^{-1}\left[\frac{1}{r_s^{min}} \cdot \left.\frac{\delta r_s}{\delta \gamma}\right|_P\right] \tag{2}$$

The analysis of the path of contact shown within Fig. 4, suggests that for every contact point the relationship between pressure angle β_r and vane angular position θ might be defined as:

$$\theta + \beta_r = \gamma_r - \psi|_P \tag{3}$$

The same correlation may be deduced for β_l by simply substituting all the subscripts. By the assumption of an angle reference frame where counterclockwise rotations define the negative sign of the angles, Eq. 3 may be applied on both lips of the vane and consequently included in Eq. 1 as follows:

$$\begin{cases} R_\theta e^{i\theta} + d e^{i(\theta-\pi/2)} + r_v e^{i(\gamma_r-\psi)} = r_s(\gamma_r) e^{i\gamma_r} \\ R_\theta e^{i\theta} + d e^{i(\theta+\pi/2)} + r_v e^{i(\gamma_l-\psi)} = r_s(\gamma_l) e^{i\gamma_l} \end{cases} \tag{4}$$

Given the cam ring profile and the vane geometry, the solution of Eq. 4 provides the vane radial displacement with respect to its angular position. It

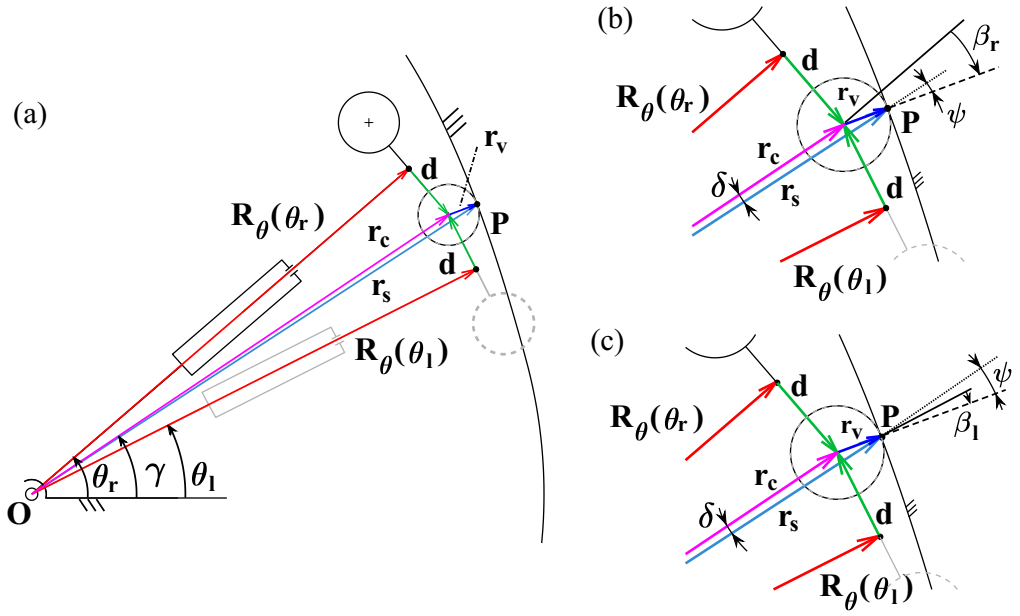

Figure 5: Vectorial representation of the closure equations for a generic point of contact (a), focus on the angles relationship for the vane right lip in contact (b) and focus on the angles relationship for the vane left lip in contact (c)

is worth noticing that, since Eq. 4 cannot be arranged into an explicit form, a numerical approach is mandatory to solve the problem. This aspect is further made less straightforward by the impossibility to define in advance the number of admissible solutions, which depend on the number of lips concurrently touching the cam ring at a given angular position. In particular, for each angle θ, if both vane lips are in contact with the cam ring profile, e.g. during dwell phase, then both lines in Eq. 4 admit a real solution indicating that two distinct contact points concurrently exists. On the other hand, if a single vane lip is in contact with the cam ring profile, e.g. during the most of rise and fall phases, then only one of the two closure equations in Eq. 4 admits a real solution.

Based on these considerations, it is fundamental to explore an alternative approach which is hereinafter proposed to determine the pump kinematics by taking advantage of the available geometrical correlations. Considering the scenario shown within Fig. 5(a), the contact point P identified by r_s and γ, might as well be considered as belonging to the right lip of the j^{th} vane or to the left lip of the $j^{th} - 1$ vane. Within this framework, the two vane

tips are treated as separate linkages, calculate their motion and consequently deduce the actual vane displacement. This approach reduces dramatically the complexity of the computation procedure since each linkage always admits a solution. Figure 5(a) shows the left and right mathematically admissible kinematic rings, composed by the vectors $R_\theta(\theta_r)$ and $R_\theta(\theta_l)$, equal in modulus. Each vane lift is described by its relative angular coordinate θ. The geometrical analysis of the kinematic rings highlight the necessity to define a parameter which give the chance to express the vane radial positions in an explicit form. Such parameter is the vector expressed as r_c. Its modulus may be calculated either considering r_c as the hypotenuse of the triangle formed by R_θ and d or as a catheter of the triangle formed by r_s and r_v:

$$\begin{cases} {r_c}^2 = {R_\theta}^2 + d^2 \\ {r_c}^2 = {r_v}^2 + {r_s}^2 - 2 r_v r_s \cos\psi \end{cases} \tag{5}$$

The combination of the two expressions, leads to an explicit form of the vane radial position which depends only on known geometrical data:

$$R_\theta^2 = {r_v}^2 + {r_s}^2 - d^2 - 2 r_v r_s \cos\psi \tag{6}$$

Since for a given positive value of parameter R_θ, two values of the vane angular position are theoretically admissible, the value of R_θ obtained with Eq. 6 refers to two different angular positions of the right and left linkage of the vane. According to the schemes in Figures 5(b) and 5(c), angle δ between r_c and the radial coordinate of the contact point r_s may be calculated as:

$$\delta = \sin^{-1}\left(\frac{r_v \sin\psi}{r_c}\right) \tag{7}$$

similarly, angle α between the vane lift radius R_θ and r_c may be obtained as:

$$\alpha = \sin^{-1}\left(\frac{d}{r_c}\right) \tag{8}$$

Equations 7 and 8 provide the chance to calculate both possible values of the vane angular position referring to the same R_θ:

$$\theta_r = \gamma + \alpha + \delta \tag{9}$$

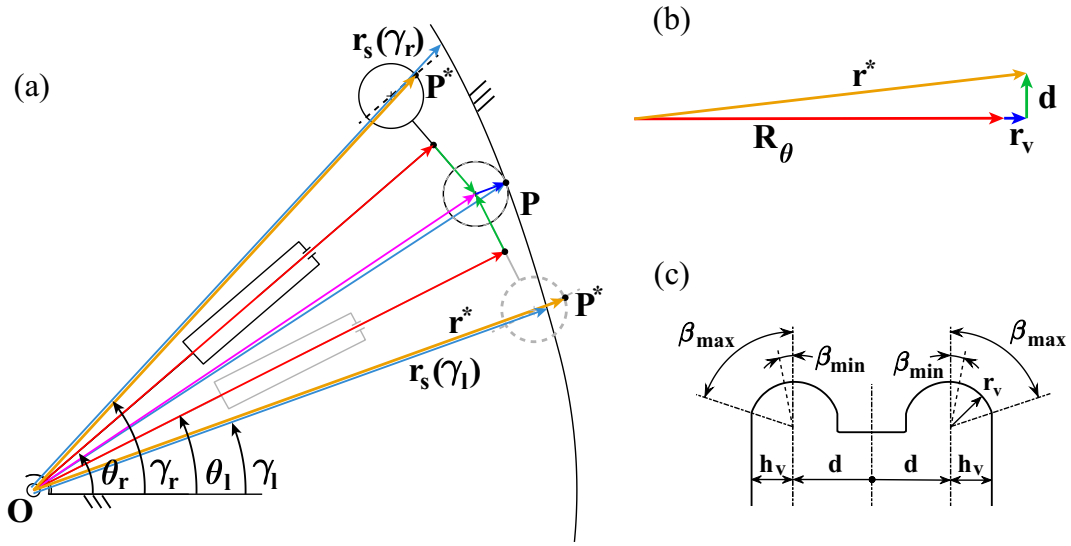

Figure 6: Vectorial representation of the closure equations including inactive radii r^* (a), Focus on the triangle adopted to determine r^* module (b), twin lip vane scheme with maximum pressure angle β_{max} on both lips (c)

$$\theta_l = \gamma - \alpha + \delta \tag{10}$$

It is worth clarifying that, from a practical perspective, only one angle between θ_r and θ_l represents a feasible configuration and consequently one of them must be rejected during calculation. The calculation of coordinate θ for both the kinematic rings gives the chance to describe the discarding process through the introduction of a set of new parameters. Figure 6(a) shows the vectors r^* and the related angular coordinates γ_R and γ_L. The vectors are representative of the maximum distance between the rotor axis O and the inactive lip of the vanes potentially involved in the contact situation. As a matter of facts, the farthest point on the inactive lip P^* lies on the middle of the vane tip and the length of r^* is equal on both vanes. For sake of clarity, the subscript l is referred to the $j^{th} - 1$ vane which is potentially in contact with the left lip, analogue consideration might be done for the r subscript. According to the

scheme depicted within Fig. 6(b), the module of the inactive radius vectors might be calculated as follow:

$$r^* = \sqrt{d^2 + (R_\theta + r_v)^2} \tag{11}$$

Thus, the angular coordinates of such angles are determined through the following expressions:

$$\gamma_r = \theta_r + \sin^{-1}\left(\frac{d}{r^*}\right) \tag{12}$$

$$\gamma_l = \theta_l - \sin^{-1}\left(\frac{d}{r^*}\right) \tag{13}$$

Since the cam ring radius is known for every generic angular coordinate it is now possible to identify the cam ring radius corresponding to the just calculated angles. The DCP issue find its solution through the comparison between inactive radius and the expected cam ring radius at the same angular coordinate. As a matter of fact, the ineligible vanes shows a inactive radius higher than the cam ring radius and for such reason will be discarded. The discarding criterion might be formalized for both the kinematic rings as:

$$\theta_r = \theta \Leftrightarrow r^* \leqslant r_s(\gamma_r) \tag{14}$$

$$\theta_l = \theta \Leftrightarrow r^* \leqslant r_s(\gamma_l) \tag{15}$$

In order to complete the assessment of the pump kinematics, it is therefore mandatory to compute the pressure angle, which represents a key design parameter to evaluate also vane contact pressure and mechanical performances [30, 32]. Within this context, the definition of the pressure angle boundaries might be crucial. While, in agreement with Fig. 6(c), the maximum value of β is given by the geometrical relationship:

$$\beta_{max} = \sin^{-1}\left(\frac{h_v}{r_v}\right) \tag{16}$$

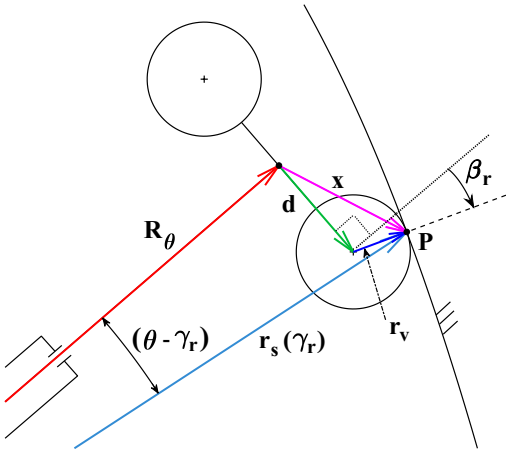

Figure 7: Focus on the path of contact with indication of vector x

its minimum value requires a further step. Actually, β_{min} is given by the value of the pressure angle during the upper-dwell phase. It has to be underlined that β_{min} may be straightforwardly computed by considering that during dwell phase angle ψ has zero value, in agreement with Fig. 4. In this scenario, with reference to Fig. 3, points O, C and P are aligned and therefore β_{min} coincides with angle $Q\hat{O}C$:

$$\beta_{min} = \sin^{-1}\left(\frac{d}{{r_s}^{min} - r_v}\right) \tag{17}$$

Then the study of the pressure angle needs to be extended to the definition of its variability through the entire pump revolution. To reach this purpose, it is required to determine the auxiliary vector x depicted in Fig. 7 by means of the Law of Cosines (for the sake of compactness, subscripts l and r are hereinafter omitted since the procedure remains valid for both sides of the vane tip):

$$\begin{cases} x^2 = {R_\theta}^2 + {r_s}^2 - 2R_\theta r_s \cos(\theta - \gamma) \\ x^2 = {r_v}^2 + d^2 - 2r_v d \cos(\pi/2 + \beta) \end{cases} \tag{18}$$

then, the explicit form of β is given as:

$$\beta = \sin^{-1}\left[\frac{{R_\theta}^2 + {r_s}^2 - {r_v}^2 - d^2 - 2R_\theta r_s \cos(\theta - \gamma)}{2r_v d}\right] \tag{19}$$

By substituting Eq. 6 in Eq. 19, the pressure angle could be finally expressed as:

$$\beta = \sin^{-1}\left[\frac{{r_s}^2 - d^2 - 2r_v r_s \cos\psi\,(1 + r_s\cos(\theta-\gamma))}{2r_v d}\right] \tag{20}$$

It is worth noticing that Eq. 20 may be also used to detail the dependence between pressure angle β and the vane geometry by r_v and d, the cam ring profile through γ, r_s and ψ and vane angular position θ.

2.4.1 *Kinematic Admissibility of TLV Geometry*

The kinematics of the machine and its coupling with practical limitations may represent an extensive source of information regarding feasibility and reliability of the design choices. Current Section is devoted to formalize the constraints to the vane geometry descending from the vane-cam ring mechanism kinematic. As first step, the analysis of the pressure angle limits gives the chance to extrapolate important indications over the vane kinematic admissibility for a given cam ring profile. With reference to Fig.6(c), is clear that the pressure angle must stand within the range:

$$0 \leqslant \beta \leqslant \beta_{max} \tag{21}$$

which may be transformed into two distinct limits. Considering the sine of the angles, Eq. 21 could be rewritten as:

$$\begin{cases} \sin\beta_{max} \geqslant \sin\beta \\ \quad 0 \leqslant \sin\beta \end{cases} \tag{22}$$

Hence, the substitution of Equations 21 and 16 into Eq. 22 provides the chance to define two design constraints correlating the geometrical vane parameters with the cam ring:

$$\begin{cases} 2dh_v \geqslant {R_\theta}^2 + {r_s}^2 - {r_v}^2 - d^2 - 2R_\theta r_s\cos(\theta-\gamma) \\ 0 \leqslant {r_s}^2 - d^2 - 2r_v r_s\cos\psi\,(1 + r_s\cos(\theta-\gamma)) \end{cases} \tag{23}$$

The second condition in Eq. 22 is always satisfied by construction, since according to Eq. 17 the pressure angle never reaches the zero value as long as

some eccentricity exists. On the contrary, the first line in Eq. 23 allows us to extract the limit values of the tip radius. By referring to the inequality as a tip radius function, its standard form becomes:

$$r_v{}^2 - \left[R_\theta{}^2 + r_s{}^2 - d^2 - 2dh_v - 2R_\theta r_s \cos(\theta - \gamma)\right] \geqslant 0 \tag{24}$$

Therefore, the analytical expression of the polynomial roots is derived from Eq. 24 as follows:

$$r_{v,\lim}^{1,2} = \pm\sqrt{R_\theta{}^2 + r_s{}^2 - d^2 - 2dh_v - 2R_\theta r_s \cos(\theta - \gamma)} \tag{25}$$

thus, the set defining the solution of the inequality in Eq. 24 is:

$$\left(-\infty, \min\left(r_{v,\lim}^{1,2}\right)\right] \wedge \left[\max\left(r_{v,\lim}^{1,2}\right), +\infty\right) \tag{26}$$

It is worth underlining that the negative terms may be discarded since they do not refer to practical scenarios. As a consequence, the solution of Eq. 25 gives the opportunity to establish the minimum allowable value for the tip radius:

$$r_v \geqslant \max\left(r_{v,\lim}^{1,2}\right) \tag{27}$$

It has to be clarified that the limit value $\max\left(r_{v,\lim}^{1,2}\right)$ depends on term r_v itself. As a matter of fact, Eq. 25 demonstrates that the knowledge of parameter R_θ is mandatory to calculate the limit value for tip radius r_v. However, r_v must be known a priori in order to determine R_θ. These observations highlights that Eq. 27 represents an implicit limit and its boundary needs to be computed numerically.

The upper limit of parameter r_v may be roughly estimated by considering that the radius of each vane lip must be surely smaller that the minimum cam ring radius, otherwise interference between the two components becomes inevitable. In addition to this consideration, a refinement of the upper limit may be obtained by evaluating the existence of the square root argument in Eq. 25, which leads to the following inequality:

$$d^2 + 2dh_v - \left[R_\theta{}^2 + r_s{}^2 - 2R_\theta r_s \cos(\theta - \gamma)\right] < 0 \tag{28}$$

The roots of the related polynomial are expressed as:

$$d_{\lim}^{1,2} = -h_v \pm \sqrt{R_\theta{}^2 + r_s{}^2 - 2R_\theta r_s \cos(\theta - \gamma) + h_v{}^2} \tag{29}$$

which allows to identify the existence range for d:

$$\left(-h_v - \sqrt{{R_\theta}^2 + {r_s}^2 - 2R_\theta r_s \cos(\theta - \gamma) + {h_v}^2} \quad , \quad -h_v + \sqrt{{R_\theta}^2 + {r_s}^2 - 2R_\theta r_s \cos(\theta - \gamma) + {h_v}^2}\right) \tag{30}$$

In analogy with the tip radius acceptance considerations, the negative values of eccentricity do not relate to practical designs and therefore the resultant set of admissible values becomes:

$$\left(0 \quad , \quad -h_v + \sqrt{{R_\theta}^2 + {r_s}^2 - 2R_\theta r_s \cos(\theta - \gamma) + {h_v}^2}\right) \tag{31}$$

As observed regarding $max\left(r_{v,lim}^{1,2}\right)$, Eq. 31 does not allow to define an explicit boundary for the set of allowable designs since the calculation of such a limit depends on term R_θ, which may be defined once both parameters r_v and d are defined. Based on this considerations, both boundaries defined by Eq. 27 and Eq. 31 need to be calculated numerically.

2.4.2 *Assessment of the Vane Motion Regularity*

The pressure angle investigation carried out within Chapter 2.4 has led to solve the duality of the point of contact and it has lastly suggested that the point of contact shifts from the right lip to the left one when moving from rise to fall phase. This characteristic represents a critical aspect in twin lip vanes, since it may lead to follower motion profiles that do not satisfy the fundamental law of cam design, stating that the follower motion must be continuous through its first and second derivative [31]. This inconvenience is further promoted by the design procedure commonly adopted for this type of mechanism. Classic cam profiles are designed in order to reproduce an a priori defined follower motion law, therefore such a law represents an input for the cam design. In this scenario, the fundamental law of cam design may be easily fulfilled by choosing appropriate mathematical laws for the rise and fall phases. On the other hand, balanced vane pumps are designed by directly choosing the cam ring profile on the basis of fluid dynamic requirements. In this scenario, the follower motion represents an outcome of the design

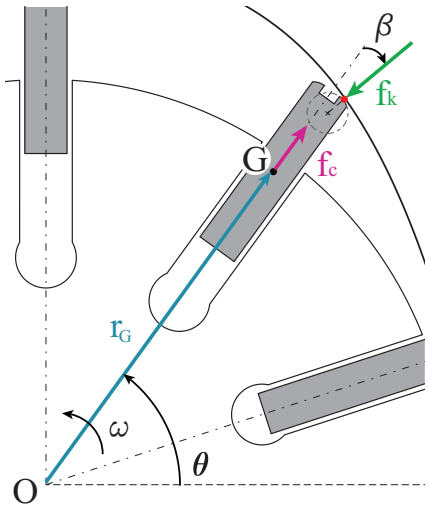

Figure 8: Schematic of the loads acting on TLV

procedure and therefore the satisfaction of the fundamental law of cam design needs be checked retrospectively.

For the sake of completeness, as explained by Norton et al. in [31], it has to be clarified that such a law does not represent a mandatory restriction for the linkage functioning, meaning that the pump might be able to operate even if its design does not satisfy the fundamental law of cam design. The drawbacks of this condition are mainly related to the NVH behaviour of the machine and the promotion of wear and undesired nonlinear dynamic phenomena such as vane detachments. Based on these considerations, it appears to be clear that the adoption of twin lip vanes contributes to increase the mechanism design complexity. While the kinematic admissibility analysis provides the chance to define the twin lip vane geometries that might be successfully implemented for a given cam ring, the analysis of the vane motion regularity allows to identify the subset of geometries that ensure a satisfactory motion and NVH behaviour.

2.4.3 *Analytical Determination of the Vane Loads*

The analytical procedure to identify the TLV admissibility domain so far discussed, has been formalized considering the impact of the restriction introduced by the pursue of a proper kinematic of the vane-cam ring mechanism.

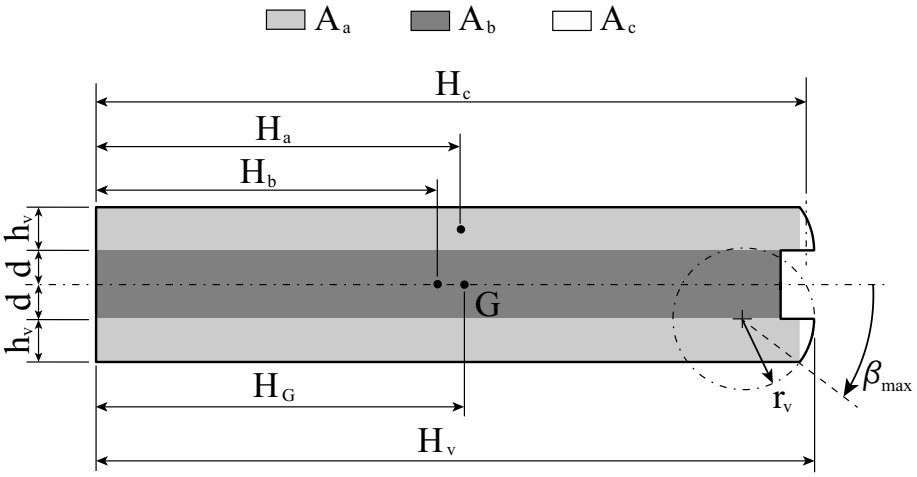

Figure 9: TLV geometrical parameters

With the purpose to complete the description and include a further confrontation parameter, within this Section the analytical estimation of the loads acting on the vane is proposed and discussed. Following the procedure exposed in [28], it is possible to express the equation which govern the vane dynamics as:

$$m\ddot{r}_G + c\dot{r}_G + f_k \cos(\beta) = f_c \tag{32}$$

where m is the vane mass, c is the damping coefficient which includes both structural and viscous damping, $\ddot{r}_G$ and $\dot{r}_G$ represent the first and second derivative of the instantaneous radial position of the vane center of gravity r_G. Such terms represents the components connected to the vane kinematics. In addition, f_k is the reaction force between cam ring and vane and f_c is the centrifugal component of the radial force. It is worth underline that for such vane design, since the under vane pockets and the pressurized chamber are connected by means of radial bores, the pressure components of the radial load are mutually compensated. Figure 8 gives a view of the loading scheme rising during the pump operation. The terms contained within Eq. 32 confirms the absolute importance of describe the vane kinematics to analytically predict the loads arising during the operation.

The description of the Eq. 32 terms should begin from the definition of the load components generated by the vane kinematic motion. Such terms represent the inertia force generated by the vane mass and the damping force

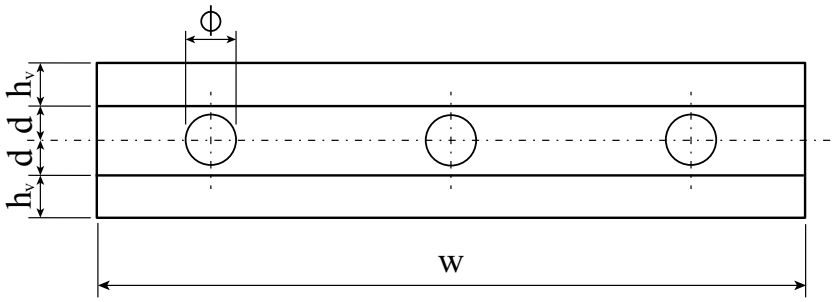

Figure 10: TLV geometrical parameters

influenced by oil and structural damping included within c. The first step of the study is the analytical formulation of the vane mass as function of the main TLV geometrical features. For sake of clarity, an example of the TLV implemented for the scope is depicted within Fig. 9 where are additionally reported the salient geometrical features necessary to describe the effective vane geometry.

In order to relate the mass of the vane to the geometrical parameters, it is worth to calculate the frontal area of the vane. With reference to Fig. 9, the total area of the vane A_v should be calculated as the sum of three elementary areas. The rectangular areas A_a and A_b should be calculated as follow:

$$A_a = 2h_v \left[H_v - r_v \left(1 - \cos \beta_{max}\right)\right] \tag{33}$$

$$A_b = 2d \left(H_v - d\right) \tag{34}$$

The remaining area A_c of the circular segment is given by:

$$A_c = \frac{{r_v}^2}{2} \left(\beta_{max} - \sin \beta_{max} \cos \beta_{max}\right) \tag{35}$$

Thus, the total area of the vane should be calculated as:

$$A_v = A_a + A_b + A_c \tag{36}$$

Since the vane frontal surface is determined, it is possible to calculate the vane mass taking into account the presence of the balancing bores along the

vane facewidth W. Figure 10 shows the topper view of a TLV and helps to identify the balancing bores and their diameter ϕ Considering a generic material with density ρ, it is possible to calculate the vane mass as function of the geometrical representative parameters:

$$m = \rho \left\{ A \cdot W - z_b \frac{\pi \phi^2}{4} \left[l_v - 1.5 \cdot r_v \left(1 - \cos \beta_{max} \right) \right] \right\} \tag{37}$$

As mentioned before, with the purpose to calculate the inertia term of Eq.32 it is now fundamental to identify the expression of r_G which represent the radial position of the vane center of gravity with respect of the pump axis of rotation. Its value may be straightforwardly calculated from the vane lift radius R_θ combined with the position of the vane geometrical center of gravity H_G. For sake of clarity it is worth express the position of the center of gravity of the three elementary areas depicted within Fig. 10. Since the vane geometry is symmetrical with respect to the horizontal axes, only the expression of the abscissa will be reported within the following expressions:

$$H_a = \frac{H_v - r_v \left(1 - \cos \beta_{max} \right)}{2} \tag{38}$$

$$H_b = \frac{H_v - d}{2} \tag{39}$$

$$H_c = H_v - r_v + \frac{\left(2 r_v \sin \beta_{max} \right)^3}{12 A_3} \tag{40}$$

Then, H_G might be calculated as:

$$H_G = \frac{A_a H_a + A_b H_b + A_c H_c}{A_v} \tag{41}$$

Finally, with a look on Figures 3 and 9 it is possible to formalize the expression of the vane center of gravity radial position:

$$r_G = R_\theta + r_v - H_v + H_G \tag{42}$$

As a matter of fact, among the terms contained in Eq. 42, the only angle dependent term is R_θ. Therefore, the derivative of r_G becomes the derivative

of the explicit expression of R_θ contained in 6. It results that the first derivative might be expressed as:

$$\dot{\bar{r}}_G = \omega R'_\theta \tag{43}$$

while the second derivative becomes:

$$\ddot{\bar{r}}_G = \omega^2 R''_\theta \tag{44}$$

where ω represents the pump working speed, which is considered as constant for the purpose of the proposed study. It is worth underline that, with reference to Eq.6, persist a strict connection between R_{theta} and both TLV and cam ring geometry. Such consideration suggests that within a design procedure, the estimation of the loads arising during the operation plays a crucial role for the choice of the cam ring mathematical law and for the TLV dimensions.

With the purpose to properly seal the oil trapped between two consecutive vanes and operate its pressurization, it is fundamental for the vanes to maintain the contact with the cam ring for the entire rotor revolution. Within this framework, for the vanes is required to overcome the inertial and damping actions formerly described. Since the pressure action is nullified by the vane balancing bores, the only load components responsible to urge outward from the rotor slots the vanes is the centrifugal force f_c. As known, for definition the centrifugal force should be calculated as follow:

$$f_c = m\omega^2 \bar{r_G} \tag{45}$$

After the formalization of the centrifugal force, it is now possible to calculate the instantaneous contact force between cam ring and vanes for every angular coordinate. It gives the chance to study the magnitude of the loads through an entire revolution, identifying if the designed vane-cam ring mechanism is suitable or if it introduces detachment risks.

2.5 APPLICATION OF A PARAMETRIC STUDY TO THE VANE-CAM RING MECHANISM

The current Section is devoted to the application of the analytical equations formerly described in Chapter 2.4. The purpose of this work is to present a general discussion on the admissibility of the twin lip vane design. In order

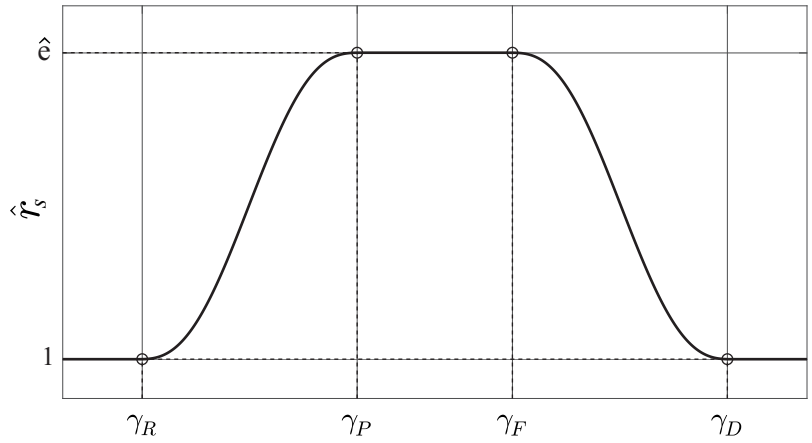

Figure 11: Reference cam ring profile where $\gamma_R = 18°$ and $\gamma_P = 72°$ respectively represent the firs and the last angular instants of the rising phase, $\gamma_F = 108°$ is the initial angular instant of the falling phase and $\gamma_D = 162°$ indicates the dwell phase starting point

to fulfil this purpose, according to Buckingham's Theorem, the geometrical parameters involved into the pump study are dimensionally reduced with respect to a specific geometrical feature. For the scope of this study, the minimum cam ring radius r_s^{min} has been taken as a reference parameter. As already discussed in [28, 29, 30], this expedient provides the chance to extend the analysis to families of similar pumps sharing same design and same non-dimensional specific displacement $\hat{V}$:

$$\hat{V} = \frac{2\pi}{{r_s^{min}}^2}\left(r_s^{max} - r_s^{min}\right)\left(r_s^{max} + r_s^{min}\right) = 2\pi\left(\hat{e}^2 - 1\right) \tag{46}$$

where $\hat{e}$ represents the ratio between r_s^{max} and r_s^{min}. With the purpose to deduce general information with wide applicability, all the parameters are hereinafter considered in their non-dimensional form and identified by the hat symbol $\hat{\cdot}$.

2.5.1 *Geometrical domain for twin lip vanes*

The kinematic analysis detailed in Chapter 2.4 provides the necessary tool to determine the vane motion given the pump geometry. As it is well known, this

aspect constitutes the starting point to deduce important information on the pump performance such as the theoretical flow rate ripple. However, within the framework of the present work, attention will be mainly focused on how the proposed dissertation may be used to calculate the set of admissible vane geometries. In particular, a detailed description regarding how to compute the limits defined within Chapters 2.4.1 and 2.4.3 will be provided together with the considerations achievable from the obtained results. The analysis involves a reference cam ring profile, characterized by equal rise and fall phases, obtained with a 5^{th} order polynomial law and non-dimensional specific displacement equal to 0.5, so that $\hat{e} = \sqrt{1 + 1/(4\pi)}$. Figure 11 shows the RFD law of the cam ring as function of the angular coordinate γ. For the first part of the dissertation, the cam ring is not designed with pre-compression zones. It is worth noticing that this cam ring coincides with the one adopted in [28, 29, 30] and it has the same timing of the one adopted by Giuffrida et al. in [27]. Thanks to this approach, it is possible to perform a comparison between the different vane designs.

In agreement with Fig. 6(c), from a kinematic standpoint the twin lip vane geometry is considered as fully described by three fundamental parameters expressed in their non-dimensional form: the tip radius $\hat{r}_v$, the lip eccentricity $\hat{d}$ and the lip half width $\hat{h}_v$. Since the computation of the vane geometry admissible domain needs to be achieved numerically, the first step to fulfil this purpose requires to define the set of parameters $(\hat{d}, \hat{r}_v, \hat{h}_v)$ in which the calculus should be performed. In this framework, it may be easily deduced that the three parameters stay within the following limits:

$$\begin{cases} 0 \leqslant \hat{d} \leqslant 1 \\ 0 \leqslant \hat{h}_v \leqslant 1 \\ \hat{h}_v \leqslant \hat{r}_v \leqslant 1 \end{cases} \tag{47}$$

It is worth noticing that, thanks to the dimensional reduction, this definition does not depend on the pump actual dimensions and it remains valid for whatever cam ring design. Indeed, the first two lines in Eq. 47 state that vane lip eccentricity and vane lip half width must be positive and smaller than the minimum value of the cam ring radius. The third line in Eq. 47 is based on the practical assumption that the vane radius cannot be smaller than the vane lip half width. Given the domain of investigation, it is necessary to compute vane motion R_θ for each point pertaining to the cam ring profile by using Eq. 6.

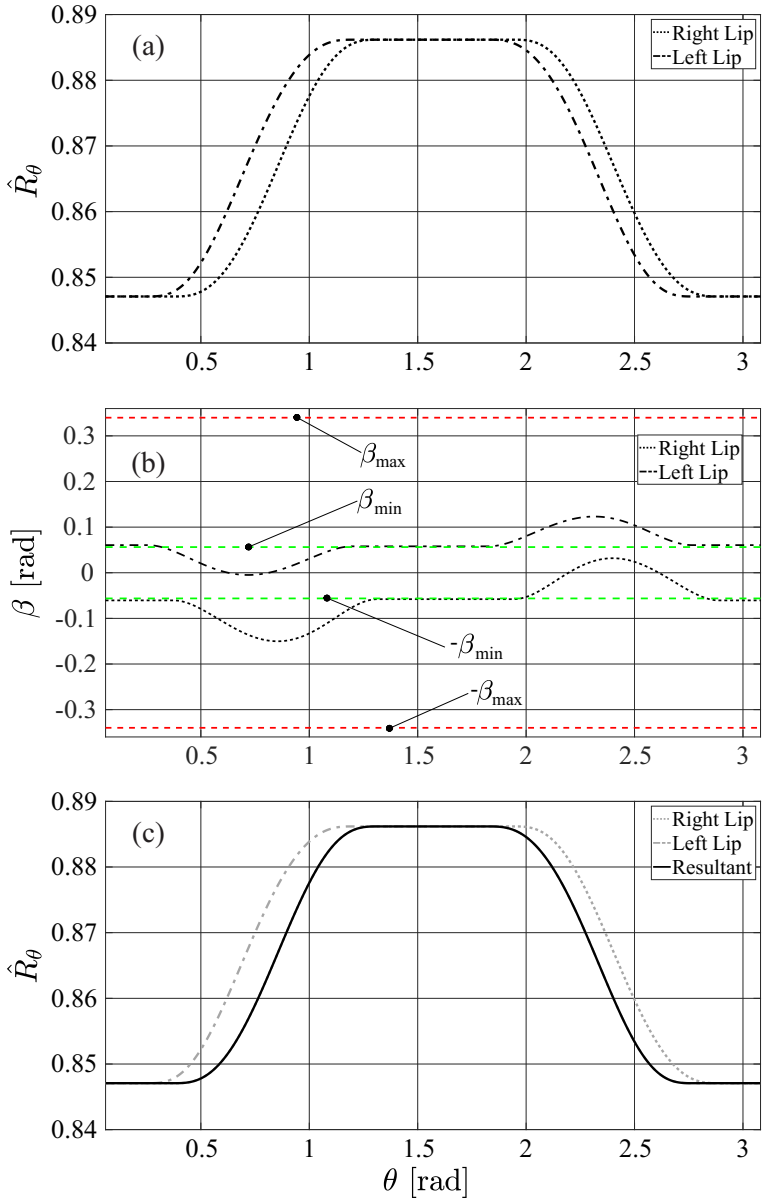

Figure 12: Right lip and left lip vane lift laws described by a twin lip vane characterized by $\hat{h}_v = 0.050$, $\hat{r}_v = 0.150$ and $\hat{d} = 0.050$ (a), description of the pressure angle trends for the contact points with maximum and minimum achievable values of β (b) and resultant vane lift law (c)

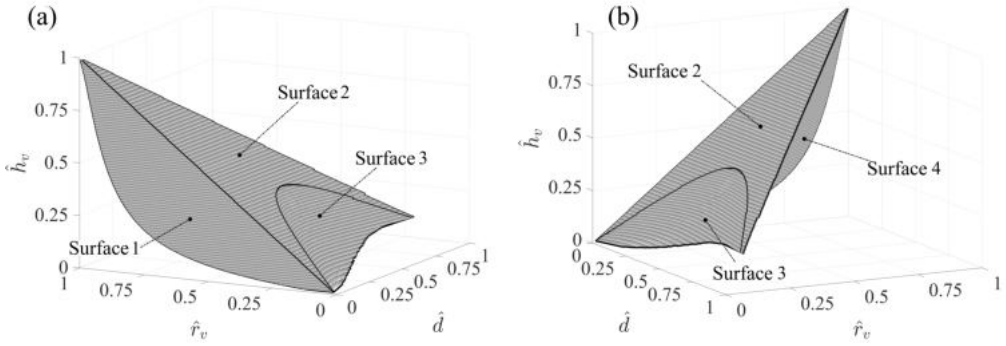

Figure 13: Different perspectives of the set of admissible TLV geometries for the cam ring profile in Fig. 11.

Once the vane displacement is known, the procedure may be used to calculate the two possible angle values θ_r and θ_l associated to R_θ thanks to Eq. 9 and Eq. 10, respectively. In order to clarify the results of this first step, it is possible to refer to Fig. 12(a) where the two solutions referring to a vane geometry with $\hat{h}_v = 0.05$, $\hat{r}_v = 0.15$ and $\hat{d} = 0.05$ are reported in the same plot. As explained in Chapter 2.4, the actual twin lip vane motion may be deduced by focusing the attention on the pressure angle associated to each solution and by keeping, for each angular position, the value of the vane lift that lead to an admissible β. By referring to the example in Fig. 12, it is possible to observe that during the rise phase the effective lift is governed by the right lip, while during the fall phase the left lip controls the vane motion. On the other hand, during dwell phases both solutions appear to be admissible in agreement with the real scenario, in which both vane lips touch the cam ring with two pressure angles sharing the same absolute value.

Once the actual vane displacement and angular position have been determined, the dissertation in Chapter 2.4.1 provides the chance to verify the kinematic acceptability of the adopted vane geometry. For each point of the vane lift, the limits defined in Eq. 26 and Eq. 31 need to be calculated and the two most restrictive conditions must be compared with the chosen combination of $\hat{h}_v$, $\hat{r}_v$ and $\hat{d}$. If this procedure is repeated for the entire domain defined in Eq. 47, the computation leads to the determination of the set in Fig. 13, which is comprehensive of all the vane geometries that meet the mandatory kinematic requirements. As it may be observed in Eq. 47.a and Eq. 47.b, the

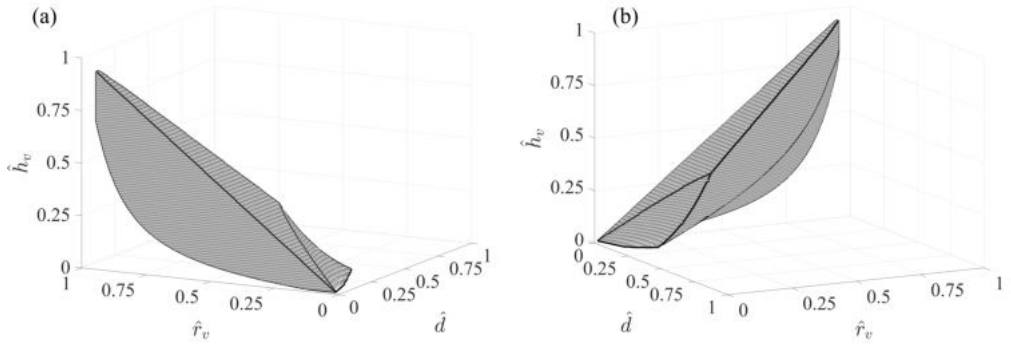

Figure 14: Different perspectives of the set of admissible TLV, coherent with the fundamental law of cam design (a,b)

domain is bounded by four surfaces: surface #1 and #2 are intrinsically defined by the computational domain in Eq. 47, surface #3 is generated by the limit interval in Eq. 31 and surface #4 is given by the limit interval in Eq. 27. For the sake of completeness, it should be clarified that practical design solutions are usually characterized by values of $\hat{d}$ less than 0.25 and values of $\hat{h}_v$ less than 0.1, with $\hat{d}$ typically greater than $\hat{h}_v$. This choice comes from the need to keep the diameter of the balancing bores (governed by $\hat{d}$) as big as possible and concurrently restrain the overall vane width.

2.5.2 *Vane Motion Regularity*

The former Subsection has led to define an explicit vane geometry existence domain on the basis of all the mandatory kinematic requirements that certify the linkage feasibility. However, such requirements do not provide sufficient guarantees regarding the resultant NVH behaviour of the machine, since no restrictions based on the fundamental law of cam design have still been applied. According to Chapter 2.4.3, additional investigations on the vane motion are therefore needed with the purpose to discard the vane geometries possibly responsible of an inappropriate pump NVH behaviour. In order to fulfil this purpose, all the vane geometries defined by the set in Fig. 13 should be further checked by computing the first and second derivatives of vane motion R_θ and looking for discontinuities. By following this approach, the set of admissible vane geometries reduces to the region reported in Figures 14(a) and 14(b),

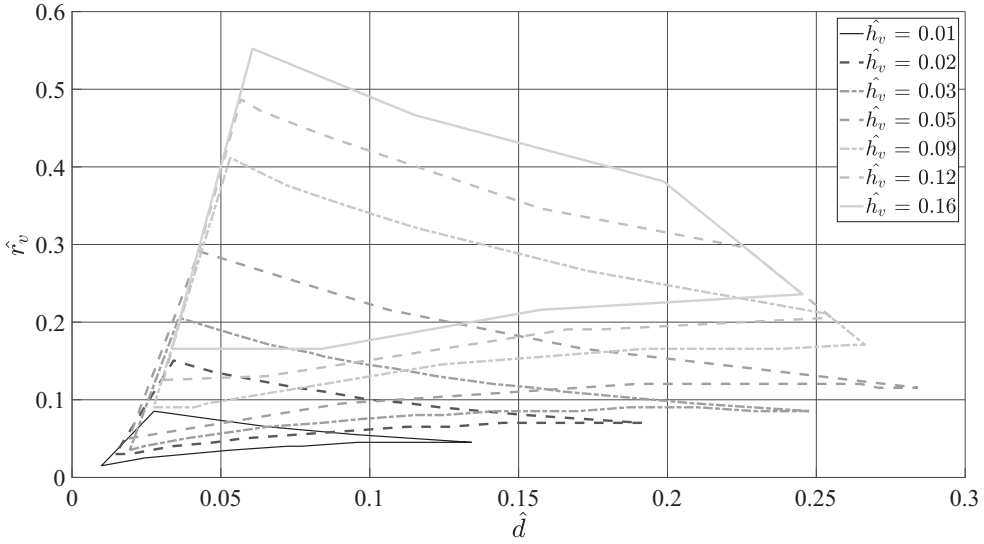

Figure 15: Isolines at discrete values of $\hat{h}_v$, representing the admissible TLV domain projected on the $\hat{d}$ $\hat{r}_v$ plane (c)

where the resulting subset is displayed from two different perspectives. As it may be appreciated from Fig. 14 and from the isolines in Fig. 15, the application of the restrictions connected to the fundamental law of cam design leads to discard all the vane geometries characterized by high values of $\hat{d}$. As a matter of fact, the main outcome of the integration between this latter limitation and the kinematic admissibility is the considerable curtailment of the twin lip vane existence domain, with a specific reference to the part of the set involving high values of $\hat{d}$. Within this context, it is worth noticing that the obtained result is in agreement with the practical consideration raised in Chapter 2.5.1, stating that real vane designs adopted in the market are usually characterized by values of $\hat{d}$ less than 0.15.

2.5.3 *Pre-compression scheme influence*

The former Subsections have detailed the numerical procedure required to explicit the analytical dissertation and consequently determine the admissible domain for the geometry of twin lip vanes starting from a reference cam ring profile. Once the correlation between the cam ring profile and the vane geometrical parameters has been clarified, it may be interesting to analyse how

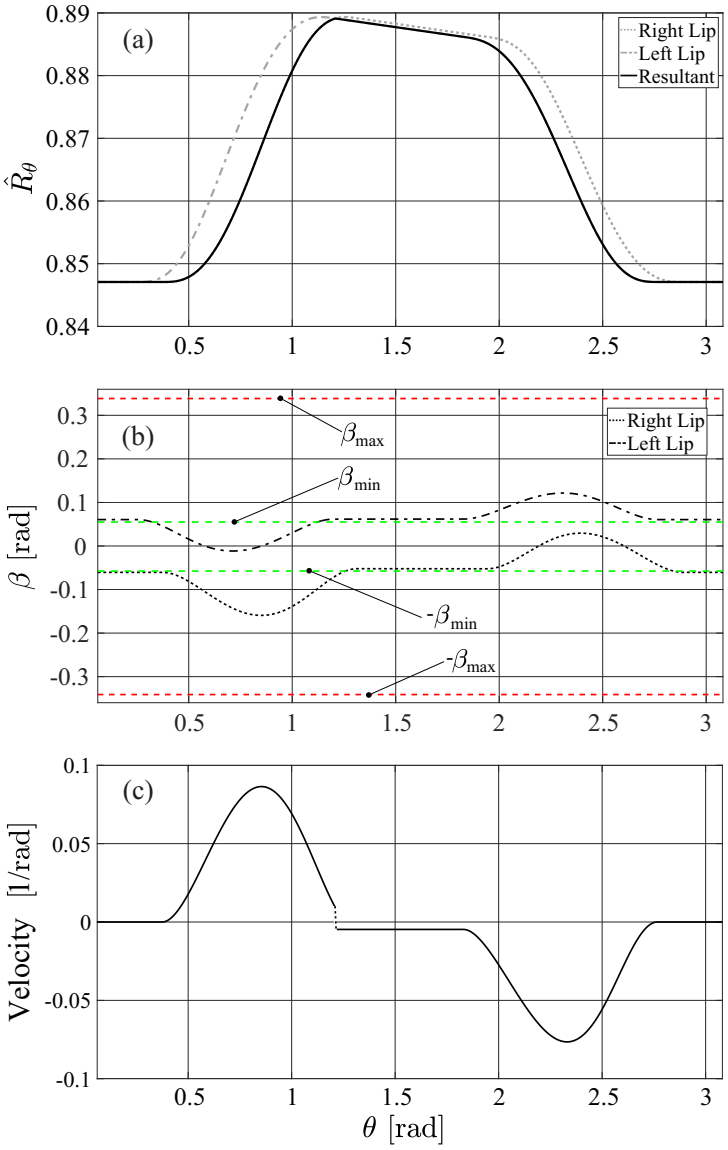

Figure 16: Right lip, left lip and resultant vane lift laws described by a TLV characterized by $\hat{h}_v = 0.050$, $\hat{r}_v = 0.140$ and $\hat{d} = 0.120$ coupled with a pre-compression cam ring (a), description of the pressure angle trends for the contact points with maximum and minimum achievable values of β (b) and vane radial velocity (c)

different cam ring design solutions affect the availability of the twin lip vane configurations.

In this scenario, a relevant role is played by the pre-compression profile [27], which is often adopted to improve the pumping capability of the machine. In order to evaluate its influence, the numerical procedure previously described is hereinafter repeated for a cam ring profile that shares the same timing and the same mathematical equations as the one depicted in Fig. 11, but with $\hat{r}_s(\gamma_P) = 1.042$ and $\hat{r}_s(\gamma_F) = \sqrt{1 + 1/(4\pi)}$. It is worth highlighting that this design solution offers no upper-dwell phases, since the linear pre-compression phase starts immediately after the rise phase. As an example, Figure 16(a) details the resultant vane displacement for a twin lip vane geometry characterized by $\hat{h}_v = 0.05$, $\hat{r}_v = 0.14$ and $\hat{a} = 0.12$, coupled to the mentioned cam ring. Within this context, Fig. 16(b) shows the pressure angle trend during the entire rotor revolution, calculated through the parametric analysis.

Despite the adopted vane design fulfils the kinematic mandatory requirements defined by Equations 27 and 31, the computation of the first derivative of the vane displacement, which is reported in Fig. 16(c), clearly demonstrates the unacceptable motion of the linkage. As it may be appreciated, a jump discontinuity takes place in the vane radial velocity when the vane moves from the rise phase to the pre-compression one. This phenomenon is obtained even though the cam ring profile has been designed with a smooth transition that is guaranteed till its second derivative. This results appears to be a permanent outcome for the entire calculus domain defined by Eq. 47: as a matter of fact, the substitution of the flat upper dwell phase with the linear pre-compression profile with no dwell results into the impossibility to achieve vane designs with satisfactory motion. From this observation it descends that, despite the kinematic analysis may provide a consistent domain of geometrically admissible twin lip vane configurations, the subsequent vane motion regularity investigation voids the entire domain.

On the basis of the achieved results, it may be deduced that the absence of dwell between the rise phase and the pre-compression phase, a design solution commonly adopted in circular tip vanes [28, 29], does not represent a feasible option in case of twin lip vanes. Starting from this observation, the last part of the parametric study is devoted to the evaluation of pre-compression schemes involving a brief dwell phase placed between rise and linear pre-compression phases. This choice seems to be also adopted in [27], where the authors noticed

its beneficial effects in case of flat tip vanes. In order to evaluate the potentials

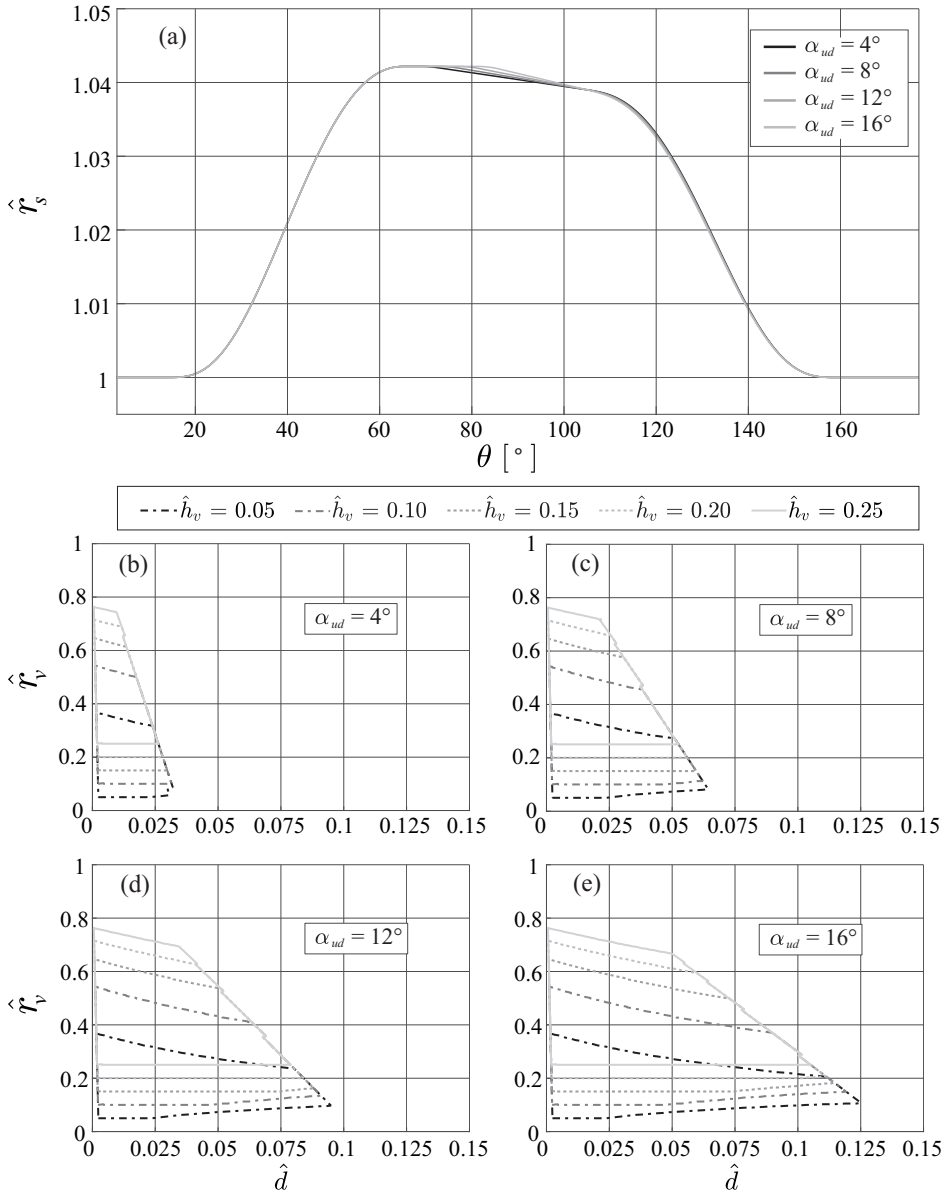

Figure 17: Influence of the brief dwell phase angular extension on the cam ring law (a), isolines at discrete values of $\hat{h}_v$, representing the admissible TLV domain projected on the $\hat{d}$ $\hat{r}_v$ plane for different brief dwell phase angular extensions: α_{UD}=4° (b), α_{UD}=8° (c), α_{UD}=12° (d) and α_{UD}=16° (e)

of this design solution, the analysis of the twin lip vane admissible domain is repeated for four cam ring profiles. The entire set of analysed cam rings share the same timing, mathematical laws and values of $\hat{r}_s(\gamma_P)$ and $\hat{r}_s(\gamma_F)$ of the profile leading to the results in Fig. 16.

The difference stands in an upper-dwell phase inserted between γ_P and the beginning of the linear pre-compression. The angular extension of this brief upper-dwell phase, defined as parameter α_{UD} in Fig. 17(a), is progressively increased from 4° till 16° in order to provide a comprehensive overview of the effects generated by this design choice. It is worth underlining that these four profiles lead to the same specific displacement, since maximum and minimum values of the cam ring radius remain unaltered. Figures from Fig. 17(b) to Fig. 17(f) report the isolines of the twin lip vane admissible domains related to the four cam ring profiles analysed. The showed results are inclusive of the restrictions related to the fundamental law of cam design, demonstrating that suitable pre-compression schemes may be implemented also in case of twin lip vanes, pending the inclusion of a sufficiently long-lasting upper-dwell phase. Moreover, the analysis clarifies that the angular extension of the upper-dwell phase is directly connected to the maximum vane eccentricity permitted. This link is due to the role played by the upper-dwell phase, which has the exclusive task to allow a smooth transition from the vane rising to the vane falling: as the upper-dwell is extended, wider vanes have the chance to avoid sudden variations of their radial motion, since both their lips can effectively touch the dwell zone when the cam ring profile derivative switches from positive to negative sign.

In order to conclude the analysis of the cam ring profile influence, a further parametric study involving the severity of the pre-compression scheme has been carried out. As shown in Fig. 18(a), four different cam ring profiles have been considered, each one sharing the same timing and the same mathematical laws hereinbefore adopted and an upper-dwell angular extension equal to 8°. The profiles are characterized by a progressively increased pre-compression ratio ξ, in order to focus the attention on the magnitude of the pre-compression. According to [28], parameter ξ, defined as:

$$\xi = 100 \cdot \left| \frac{\hat{r}_s(\gamma_P) - \hat{r}_s(\gamma_F)}{\gamma_P - \gamma_F} \right| \tag{48}$$

may be considered as an index of severity of the pre-compression scheme, since it is linked to the slope of the linearly decreasing cam ring radius. Figures from

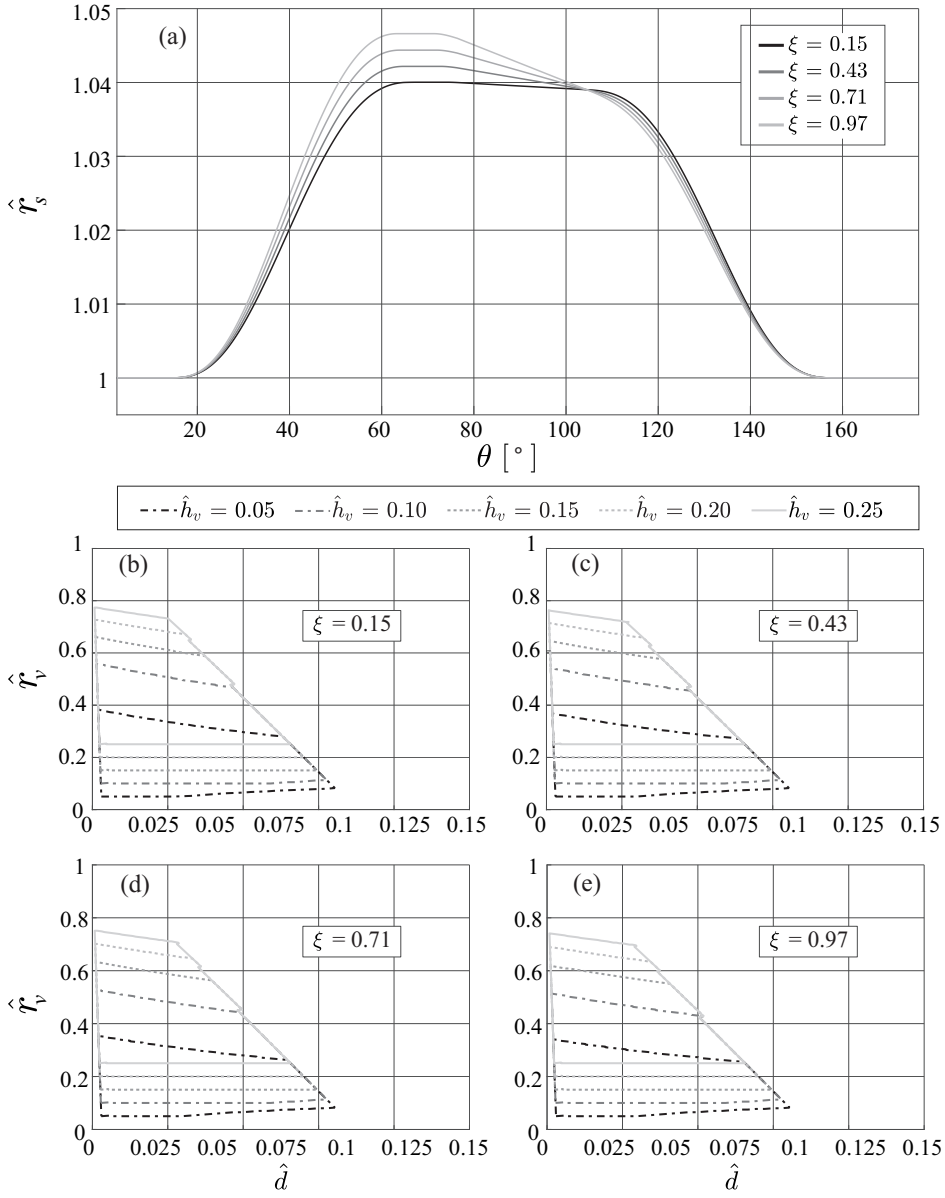

Figure 18: Influence of the precompression ratio on the cam ring law (a), isolines at discrete values of $\hat{h}_v$, representing the admissible TLV domain projected on the $\hat{d}$ $\hat{r}_v$ plane for different precompression ratios: ξ=0.15 (b), ξ=0.43 (c), ξ=0.71 (d) and ξ=0.97 (e)

Fig. 18(b) to 18(f) report the isolines of the twin lip vane admissible domains related to the four cam ring profiles analysed. As it may be appreciated, results present extremely slight differences between each other, indicating that the four cam rings may host the same twin lip vane designs. This outcome is produced because the boundaries of the set of admissible vane geometries are generated basically by the vane pressure angle, which cannot overcome a given maximum value, and by the restrictions imposed the by fundamental law of cam design. The former, in particular, is mostly influenced by the sharpness of rise and fall phases, therefore one would expect to observe some key changes in the results due to the increment of $\hat{r}_s(\gamma_P)$. However, the latter is not altered by the variation of ξ, since the extension of the upper-dwell phase remains unvaried. By considering that the limits imposed by the fundamental law of cam design have been shown to produce more restrictive boundaries, this behaviour explains the nonentity of the variations observed between the results. In conclusion, the analysis demonstrates the kinematic feasibility of the pre-compression scheme in balanced vane pumps adopting twin lip vanes, as long as a certain amount of upper-dwell phase is included. In particular, the study highlights the key role played by the extension of the upper-dwell profile, which has a relevant influence on the maximum admissible value for the vane eccentricity.

2.5.3.1 *Radial Load Characterization*

The application of the analytical procedure described within Chapter 2.4 gives the chance to include within the design procedure the restriction connected to unsuitable vane loads. In particular, through the calculation of the instantaneous vane loads through the entire pump rotation it is possible to identify maximum and minimum total loads acting on the vane. The results of such calculation are fundamental to evaluate the risk of detachment of the vane from the cam ring, the magnitude of the resultant contact load between vane and stator and the amplitude of the loads variation. The extension of the calculation to the entire admissibility domain allows to identify several influence maps which complete the description of vane behaviour. It is worth clarify that the study has dealt with cam ring without precompression modification. As well as for previously shown admissibility domains, even for the loads characterization only reasonable values of h_v have been considered. As mentioned before, the particular design of the TLV allows to include balancing bores along the

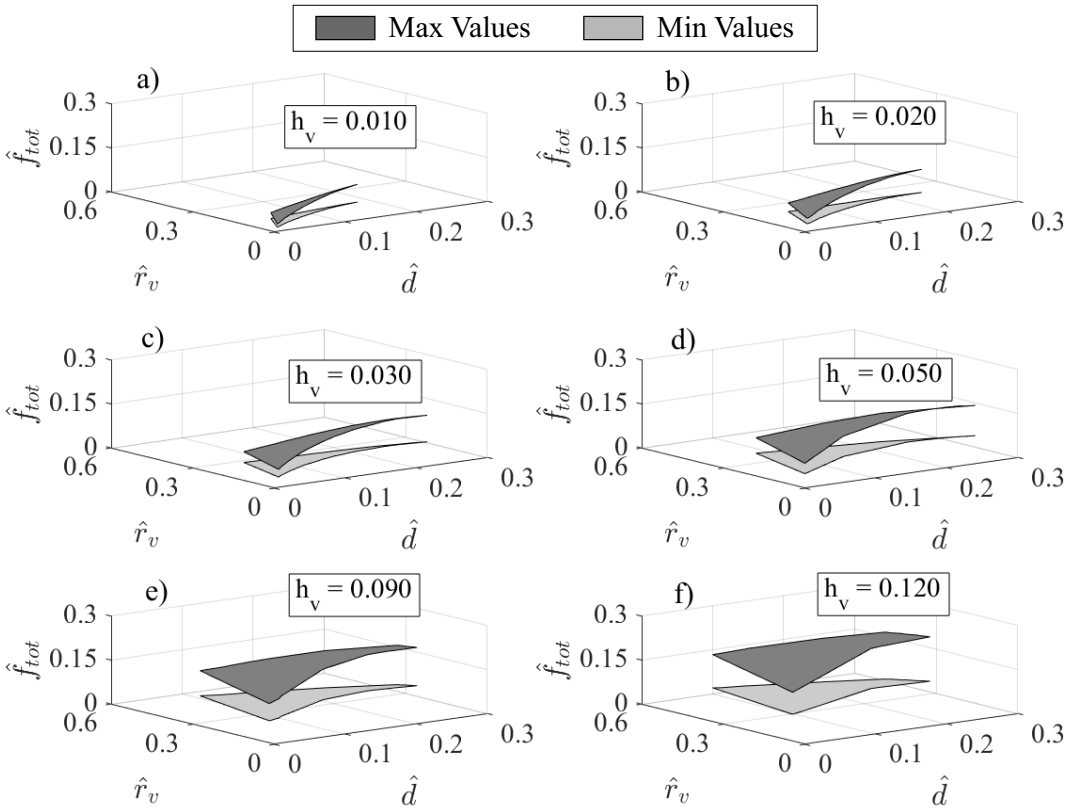

Figure 19: Maximum and minimum values of the total radial load acting on the vane, calculated for the entire admissibility domain at different h_v values

vane facewidth capable to neglect the pressure components from the total radial force.

Figure 20 shows the confrontation between the maximum and minimum values of the total radial force acting on the vane, raised through a pump revolution at constant angular velocity ω. The maps have been calculated for the entire admissibility vane domain for different values of the vane half width h_v. In addition, for the scope the total length of the vane l_v and the vane facewidth w_v have been considered as constant. Their values have been respectively set on 0.6 and 0.4. Analysing the picture is clear that incrementing the vane half width the difference between the maximum and the minimum registered total load increases. Analogue consideration descends from the analysis of the single subfigures of Fig. 20. As may be observed, the loads

difference tends to increase following the increment of tip radius r_v and, particularly, the vane eccentricity. It is worth underline that, with reference to Eq. 37, the increment of such parameters determines the increment of the vane mass. Where the admissibility domains allows large vane eccentricities, the values of maximum loads strongly increase. On the other hand, Fig. 20

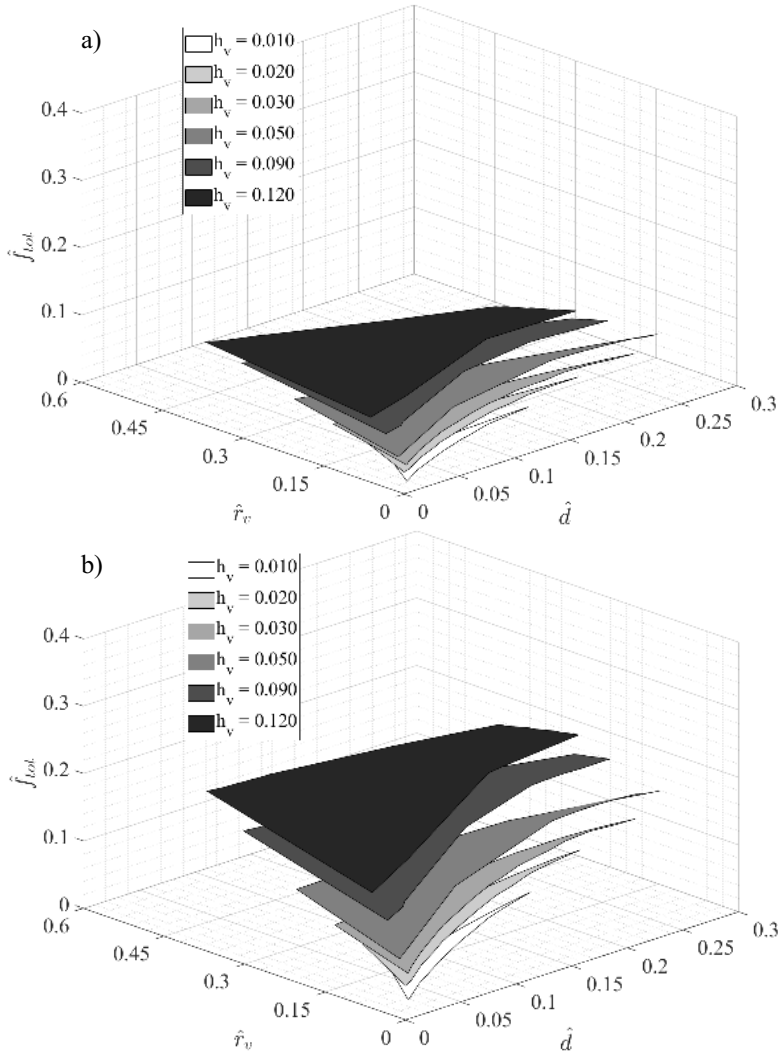

Figure 20: Maximum and minimum values of the total radial load acting on the vane, calculated for the entire admissibility domain at different h_v values

shows the confrontation between maximum and minimum values of total loads

for different vane half width. In particular, Fig. 20(a) depicts the minimum values of total loads. The overlapped layers, representative of different vane half width, do not show great differences increasing h_v. On the contrary, the distance between layers in Fig. 20(b) becomes more significant increasing h_v. Furthermore, the slope of maximum load layers is higher than the minimum. It descends that the vane mass mostly affects the maximum radial loads while the minimum values are almost constant trough the admissibility domain at constant h_v. With the purpose to deepen the investigation on how the TLV

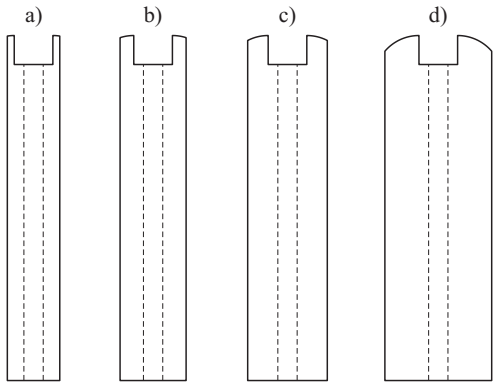

Figure 21: TLV with tip radius $\hat{r}_v = 0.065$, eccentricity $\hat{d} = 0.028$ and different values of vane half width: $\hat{h}_v = 0.01$ a), $\hat{h}_v = 0.02$ b), $\hat{h}_v = 0.03$ c) and $\hat{h}_v = 0.05$ d)

design modifications impact on the vane kinematics and the resultant pump behaviour, four vanes with equal tip radius and eccentricity but different lips width have been studied. Figure 21 allows to understand how the increment of $\hat{h}_v$ changes the vane geometry and the extension of the circular part of the lip. Within this context, Figure 22 shows the timing between the total load and the pressure angle through a pump revolution, for the set of vanes under investigation. In addition, it allows to identify how the increment of the lips width affects the magnitude of the total load and the amplitude of the pressure angle. Thinner vanes reach lower load amplitude and peaks, essentially thanks to a minor mass which reduces the centrifugal contribute. On the other hand, such vanes are affected by higher variation of the pressure angle that may be responsible of more severe wearing phenomena.

Since the results shown within [28] have highlighted the absolute predominance of the pressure load components on the total radial force for single lip vanes, the presented load maps for TLV have shown a substantial containment

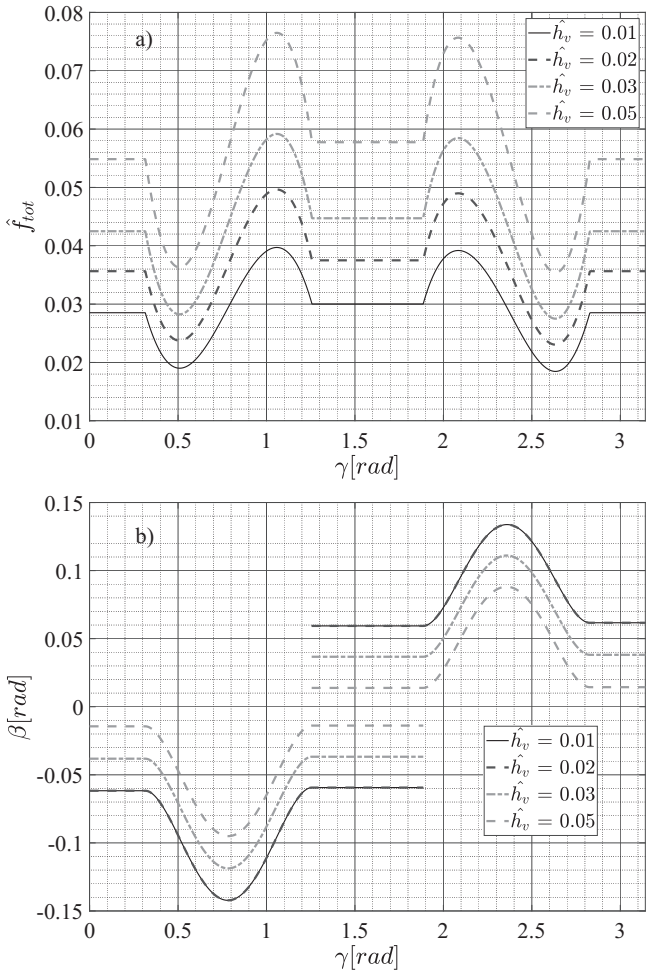

Figure 22: Plot of the total force for vanes with $r_v = 0.065$, $d = 0.028$ at different h_v values (a) and plot of the pressure angle trend for same vanes (b)

of the total radial force. Therefore, balanced vane pump equipped with TLV are capable to achieve higher delivery pressure than the single lip equipped avoiding the severity of contact loads which are major responsible of wearing phenomena of cam ring and vanes.

2.6 FINAL REMARKS

The Chapter has presented a kinematic based methodology for a coherent design of balanced vane pumps equipped with twin lip vane design, focusing the attention on the definition of vanes admissibility domains. The vane-cam ring mechanism has been outlined as an inverse cam-follower mechanism where the moving component is represented by the vane while the statoric component is the cam. The particular vane design introduces a critical kinematic issue: since the vanes have two circular lips which enter in contact with the cam ring in different instant, it is fundamental to clarify for every angular position on which lip the contact take place. The first part of the research has concerned the description of the vane motion law through the analytical implementation of the closure equations for each vane lip. A dedicated focus has been provided regarding the solution of the closure equations, which require to address the mentioned issue related to the duality of the point of contact. The analysis of the path of contact and of the kinematic rings components has allowed to formalize a discarding criterion for the identification of the representative ring. Then, the analytical expressions referring to the kinematic admissibility domain of the vane geometrical parameters have been formalized and deeply discussed. The correlation between kinematic constraints and vane geometrical parameters has been deployed through an explicit formulation which considers the vane radial motion and the pressure angle analysis. In parallel to the kinematic constraints, the verification of the compliance between the resultant vane motion law and the fundamental law of cam design has been included as additional limitation. Within this framework, the study has led to provide a comprehensive dissertation on the actual feasibility of the mechanism. Since the purpose of the study has been the identification of a design procedure which helps to design a vane pump that meets the performances requirements and additionally ensure a satisfactory NVH behaviour, the analysis of the loads acting on the vanes has been included.

In order to corroborate the analytical investigation, the work included a parametric study based on the Buckingham's Theorem that gave the chance to produce general results referring to families of similar pumps. Initially, the cam ring geometry has been assumed as indisputable input data and the study focused the attention on the numerical procedure required to distinguish the actual contact point and determine the vane radial motion. Later, the

attention moved to the computation of the entire set of twin lip vane designs that satisfy the mandatory kinematic requirements. The results demonstrated the existence of a bounded set, containing all the combinations of vane tip radius, eccentricity and width that respect the linkage closure equation. In this context, the computed domain showed that the large majority of feasible vanes are characterized by low specific eccentricity and lip half width values. With the purpose to identify the vanes ensuring a regular vane motion, which is a characteristics promoting a satisfactory pump dynamic, the analysis has been deepened by including the restrictions related to the fundamental law of cam design. Due to this additional limitation, the initial admissibility domain resulted as further curtailed, exclusively preserving the twin lip vane geometries with specific eccentricity values lower than 0.3. As a matter of fact, the computed domain includes TLV that even if satisfy the kinematic constraints are not eligible to properly work in a vane pump. Since the procedure seeks to constitute a robust and reliable design tool, it is worth to clarify that vanes with total width greater than the 40% of the cam ring minimum radius are not suitable to assure the pumping action of the machine.

Within the definition of admissibility domains context, subsequently to the study of the interactions between TLV and simple RFD cam rings, the study has been focused on the implementation of different family of cam ring profiles involving several pre-compression schemes. By following the same steps carried out for the previous analysis, the study has demonstrated that twin lip vanes cannot be adopted in these peculiar profiles as long as no upper-dwell intervals are interposed between rise and pre-compression phases. This result is specifically produced by the limits imposed by the fundamental law of cam design: the absence of an upper-dwell phase produces a discontinuity in the first derivative of the vane radial motion due to a harsh transition of the contact point from one vane lip to the other. Based on this observations, additionally considering the crucial role acted by pre-compression profiles for the achievement of higher delivery pressure, further numerical studies addressing the influence of the upper-dwell phase on the twin lip vane design admissibility have been reported. In this context, two different approaches have been implemented: the extension of the upper-dwell phase with the purpose to ensure a smoother contact lip transition and the increment of the pre-compression ratio. The analysis highlighted the key role played by the angular extension of the upper-dwell phase, which basically determines the

maximum allowable vane eccentricity, while the pre-compression ratio appears to have a negligible impact.

In the last part of the Chapter, the numerical analysis of the loads acting on the vane has been presented. The analysis has been performed considering the cam ring designed without the pre compression profile. As first consideration, it is worth mention that thanks to the balancing bores, twin lip vanes are subjected to the pressure force compensation. Since the predominant loading component would be neglected, twin lip vanes generates loads against the cam ring lower by two order of magnitude if compared with single lip vanes. The centrifugal force has been evaluated as the most relevant component, its definition suggests that the vane mass is extremely influent on the total load calculation. As a matter of fact, the maximum load map calculated for the entire vane domain has shown that where the admissibility domain includes higher value of vane eccentricity the load fluctuation increase as well as the peak value of the radial force. On the other hand, the analysis of the pressure angle for vane with crescent lip width has shown that thinner vanes have higher pressure angle fluctuation. It descends that, even if the differences are minimal, for such vanes may exists a considerable risk of vane wearing, results of the sliding between vane lip and cam ring.

The originality of the presented work stands in the development of an organic and robust design procedure which deals with the kinematic constraints and with the dynamic implications that affect the design of twin lip vanes balanced vane pumps. The results of the study remark that design a TLV capable of a proper kinematic and contemporaneously a contained loads development is an articulated process which requires robust basis and guidelines.

3

HIGH ACCURACY PREDICTION OF GEAR PUMP PERFORMANCE BY USING LUMPED PARAMETER APPROACHES

The Chapter deals with the description of a lumped parameter model implemented to numerically analyse the gear pumps performances. The proposed model represents the update of a previous version which was developed for a specific gear pump. The novelty aspects introduced are firstly represented by a new method for the calculation of both the axial exchange areas between gear vain and side plate grooves and the vain control volumes. The updates give to the model improved flexibility and reliability. Then, a novel approach for the calculation of the flowrates between adjacent control volumes has been implemented. In this framework, the adoption of specific tailored flow parameters for different families of orifices gives the chance to avoid the definition of the laminar or turbulent flow a priori. The flow regime is free to vary, following the pressure and flow ripples that the model instantaneously calculates. It descends that the description of the pump internal flows acquires greater consistency increasing the reliability of the results. The model has been assessed through dedicated test campaign checking the coherence between numerical and experimental flow ripples. With the model it is possible to additionally describe the gears micromotions and the pressure loads distribution. Within the current Chapter, with the purpose to demonstrate the model potentiality, a gear pump design improvement case study has been included. Moreover, it is also included a gear pump design procedure which represents a key tool for the design of novel gear pumps. The procedure allows to estimate pump internal clearances and volumetric efficiency, in parallel to the calculation of the journal bearings and the gear pair representation.

3.1 CHAPTER NOMENCLATURE

Latin symbols

A	generic exchange area
ad	addendum
B	oil Bulk's modulus
b	backlash
cr	contact ratio
Cq	flow coefficient
Cc	pump displacement
D	circle diameter
f	pressure force
g	bridge extension
h	tooth height
hd	hydraulic diameter
I	gearpair center distance
$\overline{K_1K_2}$	active meshing segment
l	bearing length
m	mass
m_n	normal module
Mb	bending moment
n	pump speed
P	oil pressure
Q	volumetric flowrate
s	tooth thickness
S	Sommerfeld's number
T	torque
V	volume of a generic tooth pocket
W	gear facewidth
w	gearpair total width

x	profile shift
$\mathbf{X}$	power loss
z	gear teeth number

Greek symbols

α	pressure angle
β	helix angle
γ	gear stock allowance
δ	radial clearance
ε	shaft eccentricity
λ	flow number
ζ	bridge contact covering ratio
η_V	pump volumetric efficiency
χ	shaft relative eccentricity
μ	oil dynamic viscosity
ν	oil kinematic viscosity
ψ	meatus height
ω	angular speed
ρ	oil density
ξ	da definire
σ_{am}	material admissible tension

Subscripts & superscripts

$drvg, drvn$	denote driving and driven gear, respectively
in, out	denote incoming or outgoing from the control volume, respectively
tl	denotes the tip and lateral orifices
pp	denotes the pre and post vain flank and orifices
sd	denotes the suction and delivery orifices
sen	denotes the piping orifices

$_{cmp}$	denotes the compensation grooves orifices
$_{op}$	denotes the operative condition
$_{base}$	denotes dimension referred to the gear vase circle
$_{pitch}$	denotes dimension referred to the gear pitch circle
$_{tip}$	denotes dimension referred to the gear tip circle
$_{root}$	denotes dimensions referred to the gear root circle
$_{b}$	denotes dimension referred to the bearings
$_{T}$	denotes dimensions referred to the cutting tool
$_{des}$	denotes design condition
$'$	denotes the pre-grinding condition

3.2 INTRODUCTION

Reliability and robustness are the most recognized features of external gear pumps that have promoted the wide diffusion of these machines in a great variety of fields of the mechanical industry. With the purpose to answer to the requests of constant improvement of the pump performance, the development of new studies, in terms of mechanical or fluidynamic efficiency as well as in terms of vibroacoustic characterization, is increasingly encouraged. Within this framework, the need of reliable and direct methods for the simulation of the pump behavior is constantly spreading among the pump constructors. Clearly, the adoption of a validated tool which allows to briefly estimate the influence of design improvements or new pump design, allows to dramatically reduce the number of physical samples and operative tests. Over the years, several studies have been carried out for the scope. The analysis of the dedicated literature gives the chance to see how the methodologies have improved and how the nowadays models are sophisticated and reliable.

One of the first mathematical models found in literature has been presented in [33]. The model was capable to predict the pressure evolution within the gear vain, considering the trapped oil as incompressible and focusing on the connection with pressure loads. Then, a different approach has been formalized by Mancò and Nervegna in [34] and lately in [35]. Here, authors have introduced the study of the oil pressure variation through the resolution of a continuity equation, considering the compressibility of the oil. In addition, the

definition of the initial conditions through the numerical solution of a system of stiff differential equations has been included. A fundamental contribute to the research was provided by same authors in [36]. An experimental methodology for the detection of the pressure within gear tooth spaces was proposed for the numerical model validation. With a similar mathematical approach, Bonacini *et al.* in [37] proposed a model where, in addition to the pressure loads, the effects of oil viscosity and gear speed have been investigated. Lately, Borghi *et al.* in [38], [39] and [40] upgraded the model including both the calculation of gear position with the purpose to evaluate the running-in process in spur gear pumps and a study of axial balance of gears.

Since the validation process of numerical models by means of experimental tests have been adopted, further development of the modelling strategies have permitted constant improving of the simulation models. The works presented by Mucchi et al. in [41] and [42] provide a non-linear mathematical model devoted to the calculation of the gear eccentricity, resulting into the definition of the instantaneous static equilibrium positions of gear axes (SEP). The salient aspects considered within the study are pressure loads, meshing forces and bearing reactions. The comparison between simulation and experimental trials, has led to the assessment of the model. Later, as presented in [43], the lumped parameters model has been developed to focus on the features of the flow during the meshing process. Phenomena such as local pressure peaks and cavitation phenomena have been detected and characterized. In addition, the model provides a methodology for the prediction of the gear axes micro-motion and for the casing wear due to the break-in process. The topic has been investigated in [44] where a former work of the authors [45] has been integrated in a lumped parameters model. The implemented model has been addressed by CFD analyses carried out in parallel and, finally, validated by dedicated experimental campaigns. The absolute consistency of the lumped parameter models is often highlighted among the dedicated literature through studies that includes a confrontation with CFD analyses [46], [47], [48]. Within this context, find a relevant role the work presented in [49] where the CFD analysis is employed to design pump grooves and internal gaps. Lately, Mucchi *et al.* in [50] have performed CFD analyses with the purpose to calibrate a set of parameters necessary for the lumped parameters model.

The relevance of the hydraulic efficiency of gear pumps has been considered as a core argument in [51] and [52]. In Ref. [51], the authors present

a mathematical model based on a previous work presented in [53], focused on the evaluation of the hydro-mechanical efficiency on external gear machines. Flowrate losses arising from internal clearances of the pump (tooth tip clearance, journal bearings clearance, lateral gap) and the mechanical losses resulting from the meshing process and from friction phenomena, have been investigated. Furthermore, in Ref. [52] a technique for the investigation of the influence of gear conicity manufacturing errors on the volumetric efficiency is proposed. Within the same framework, in Ref. [54] the authors analysed the influence of manufacturing tolerances on tooth tip clearances and bearing clearances on the pump efficiency for a wide sample pump population. The effects of gear manufacturing and assembly errors on meshing loads have been deeply investigated by authors in Ref. [55]. In addition, in Ref. [56] the connection between the stiffness of floating supports and the meshing forces has been extensively surveyed.

As it can be appreciated from this literature survey, thanks to the constant upgrade of the modelling techniques over the last thirty years, the adoption of LP model for pump prediction represents a reliable choice. Since LP models do not necessarily requires dedicated software and extremely powerful calculators, the diffusion of such numerical approach is nowadays still spreading. Within this context, the aim of the present Chapter is to describe the mathematical formulation and the implementation of a novel LP model. The current model represents an evolution of a former calculation tool developed for a specific gear pump [54]. As first improvement, with the purpose to give to the model the flexibility required to become an accurate and reliable design tool adoptable for the design of pump improvements or new pump projects, a novel method for the calculation of the passage areas from gear vain to lateral grooves has been introduced. In second hence, the flows between adjacent control volumes have been described by means of a continuity equations which instantaneously identify the laminar or turbulent regime. Finally, a study of the bending of the gears has been included with the purpose to coherently represents the internal gap between gears that might vary during the operations. The assessment of the new calculation method has been performed by means of dedicated test campaigns where the flow parameters, involved into the continuity equations, have been properly calibrated. In addition to the delivery pressure and flowrate estimation, the model is capable to represents the pressure loads evolution and the running-in profiles described by gear tip

In order to develop a complete design tool, a design procedure for the calculation of the gears equipped on the simulated gear pump, has been integrated. Such design tool may be employed in the early stages of a new pump development or for the reproduction of an existent one. The methodology has been structured with the purpose to drive the design procedure with the choice and calibration of a limited number of input parameters. The main outcomes concern the detailed gearpair geometry, which includes also information regarding the rack cutter profile, the maximum allowable width of the relief grooves, as well as the gearpair center position and the estimation of the gear stock allowance. It is worth pointing out that the geometrical design of the gears concerns traditional enveloped tooth profiles. It is based on the analytical equations presented in [57] and integrated with the pump displacement calculation presented in [58] for spur gears and [59] for helical gears. Moreover, the calculation is carried out as an iterative procedure within which the gearpair could be tailored to meet the established space requirement and functioning constraints, through the manual calibration of the input parameters. In addition, the proposed procedure provides not only the geometrical characterization of the gear pump, but it also deals with its structural design. Furthermore, the main pump clearances, addressed by [60], and the design of the journal bearings have been implemented by correlating them to the tooth geometry, the estimated loads and the working condition parameters.

The result of the current Chapter is the definition of a comprehensive design tools which allows to generate a gearpair that meets initial performance constraints, evaluate the internal gaps and simulate the pump dynamic behaviour giving information on internal loads and pressure ripples. The first Section of the Chapter is devoted to the description of the mathematical theory at the base of the LP model, from the continuity equation formalization to the pressure loads calculation. Then, the model workflow is presented within Section3.4. Furthermore, Section3.5 is devoted to describe the experimental campaign carried out for the model validation. Within Section 3.6 the application of the model in a performance improvement case study is presented and discussed. In the concluding part of the Chapter, while Section 3.7 deals with the description of the gear pump design procedure, the last Section is devoted to the concluding remarks.

3.3 MATHEMATICAL ASPECTS OF THE LUMPED PARAMETERS MODEL

The developement of a LP model for the study of the gear pump fluid-dynamic behaviour expects, in first hence, to discretize the internal fluid domain into significant limited control volumes (CV). Then, for such oil pockets it is necessary to describe the oil flows exchanged through the passage sections between adjacent control volumes. As a matter of fact, for this work the subdivision of the internal volumes follows the method adopted in [54] which relies on the meshing zone discretization presented by Vacca *et al.* in [43].

For the proposed model, the connection between control volume pressure variation and flow rates Q_i are described by means of the following continuity equation:

$$\frac{dP}{dt} = \frac{B}{V_i}\left[\sum Q_i^{in} - \sum Q_i^{out} - \left(\frac{dV_i}{dt} - \frac{dV_i^{var}}{dt}\right)\right] \tag{49}$$

Assuming constant transmission ratio and angular velocity ω, it is possible to express a single continuity equation as function of the angular coordinate θ, valid for both gears involved:

$$\frac{dP}{d\vartheta_1} = \frac{B}{V_j}\left[\frac{1}{\omega_1}\left(\sum Q_j^{in} - \sum Q_j^{out}\right) - \left(\frac{dV_j}{d\vartheta_1} - \frac{dV_j^{var}}{d\vartheta_1}\right)\right] \tag{50}$$

The structure of the equation, gives the chance to identify the two contributions that affects the pressure variation within the control volumes: one is given by the total flowrate balance, the second is given by the control volume variation caused by the gear motion. It is worth noticing that the angular discretization become very useful in the description of the model and, in particular, for the inspection of the timing of the pump internal phenomena.

The flowrate calculation implemented within this work, represents one of the novelty aspects with respect to the base model of Ref.[54]. In the base model, the flows have been calculated with the Couette-Poiseuille equation in case of low Reynolds number, with the Bernoulli's equation for high Reynolds number. With such approach, the nature of the flow needs to be attributed *a priori* on the basis of experience, considering the clearance size and how the oil might flows. The model upgrade has been developed giving the opportunity to autonomously switch from laminar to turbulent regime thanks to

the Bernoulli's equation implementation with a specific control over the flow coefficients Cq. The equation is formulated as:

$$Q = CqA\sqrt{\frac{2|\Delta P|}{\rho}}\,sign(\Delta P) \tag{51}$$

where ΔP is the pressure difference between adjacent control volumes and A is the passage area. As mentioned above, Cq is the flow coefficient which is a non dimensional parameter responsible of the transition from laminar to turbulent regime. It is calculated as:

$$Cq = Cq_{max}\tanh\left(\frac{2\lambda}{\lambda_{crit}}\right) \tag{52}$$

The value of Cq_{max} is established on the basis of the orifice geometry and its value stands between 0 and 1. On the other hand, λ_{crit} represents the critical flow number which is a non dimensional coefficient, responsible of the orifice geometry complexity characterization. The expression of the flow number λ highlights the nature of the parameter:

$$\lambda = \frac{hd}{\nu}\sqrt{\frac{2|\Delta P|}{\rho}} \tag{53}$$

where appears hd which is the hydraulic diameter of the orifice and the oil kinematic viscosity ν, evaluated at the mean pressure between the adjacent control volumes.

As a matter of fact, since λ_{crit} is a parameter properly set for the orifice, the pressure variation rules the transition of the flow regime affecting the local λ value. In fact, due to the nature of the function tanh, with slight increments of the argument the function swiftly tend to its maximum represented by 1. It descends that, when the calculated λ equalizes or overcomes its critical value, the Cq value adopted within Eq. 51 tends to reach its maximum value, giving to Eq. 51 the classical formulation of the Bernoulli's equations in case of turbulent regime. On the contrary, if for the passage area subjected to the calculation λ is lower than the critical threshold, the flow coefficient for Eq. 51 is lower than the expected maximum value. By means of such reduction, the Bernoulli's equation would be adopted for the calculation of the flowrate either in laminar regime.

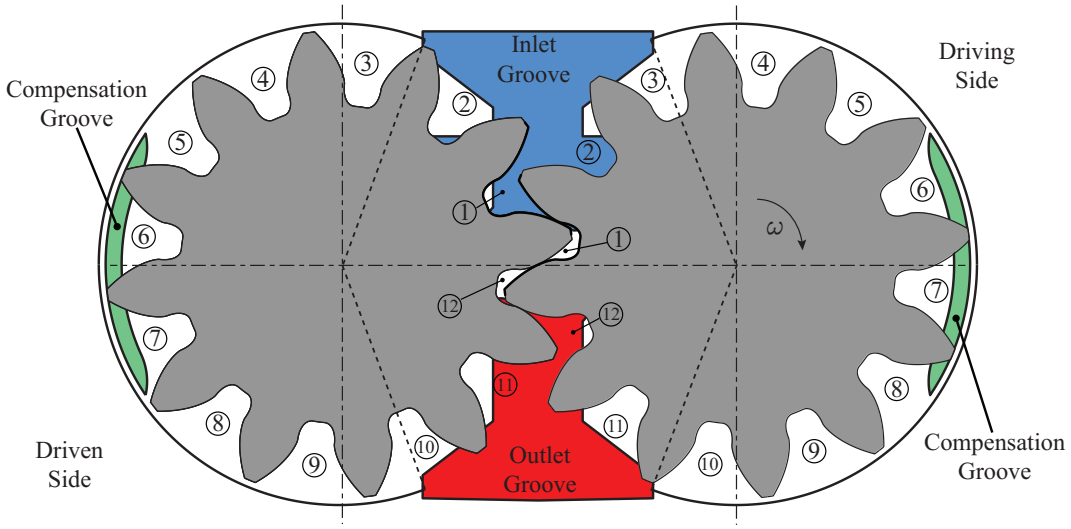

Figure 23: Schematic view of the pump implemented within the model with reference to the gear vain control volumes enumeration

An additional novelty aspect is represented by the introduction of the Bulk's modulus dependency on the pressure variation. Besides giving a more coherent flow description, such improvement allows to take into consideration the influence of the oil air fraction and how it affects the flowrates, considering the study carried out in [61], [62] and [63]. Furthermore, oil aeraction constitutes the main potential cavitation risk ([64], [65], [66]). Since completely avoid the presence of air bubbles within the circulating oil is almost impossible in gear pump and the air may costs a dramatic shrinkage of pump performance, the evaluation of its effects during the simulation process represent a crucial aspects to properly estimate pump performances. The Bulk's module pressure dependency has been evaluated through the implementation of the equation:

$$B = \frac{(1-\alpha_0)\left(1+m\frac{(P-P_0)}{B_0}\right)^{-\frac{1}{m}} + \alpha_0\left(\frac{P_0}{P}\right)^{\frac{1}{\xi}}}{\left(\frac{1-\alpha_0}{B0}\right)\left(1+m\frac{(P-P_0)}{B_0}\right)^{-\frac{m+1}{m}} + \frac{\alpha_0}{\xi P_0}\left(\frac{P0}{P}\right)^{\frac{\xi+1}{\xi}}} \tag{54}$$

3.4 LUMPED PARAMETERS MODEL STRUCTURE AND WORKFLOW

The model is essentially structured into three main modules: preprocessing, where the gearpair is generated and exchange areas and control volumes are calculated through the entire pump revolution; resolver module, where the mathematical model presented in Section 3.3 is implemented with the purpose to calculate pump performances; post-processing for the extraction of the simulation outcomes and the confrontation with experimental data. With the purpose to have a flexible and programmable tool for the data post processing and for eventual upgrades, the model has been implemented within Matlab environment.

With reference to the gear pump internal volumes, within Fig. 23 is included the enumeration scheme of the vain control volumes. The enumeration follows the rotation verse of the gears and represent a crucial aspect of the model. Since, in order to properly calculate the exchanged flowrates, it is fundamental to coherently put in communication the correct CVs, within the preprocessing section the volumes properties are collected following such framework. The control volumes map of the model is given within Fig.24 where for each volume are additionally reported the exchange sections. For sake of clarity, the scheme describes the instantaneous position reported in Fig. 23. It is worth noticing that within the pump, part of the control volumes have a constant value *e.g.* volumes associated to inlet, outlet and compensation grooves. On the contrary, the gear control volumes are subjected to a variation essentially caused by the mating tooth that invades the vain volumes in the meshing zone. Each control volume is characterized by the oil instantaneous pressure value and exchanges flowrate with adjacent volumes through the boundary sections. The pump communicates with the rig circuit through the sections of the inlet and outlet chambers. In particular, on the delivery side has been modelled the volume of the rigid pipe where the pressure sensor has been located during the test campaign. Such control volume has been considered as reference volume for the calculation of the mean delivery pressure and the pressure ripple. Thus, the piping control volume has been included simulating the flexible piping equipped during the experimental activity. At the end of the piping, a variable hydraulic orifice for the delivery pressure tuning, has been located. Then, the oil flows toward an hypothetical tank. The circuit is finally closed connecting the tank with the pump suction chamber. The external circuit components have

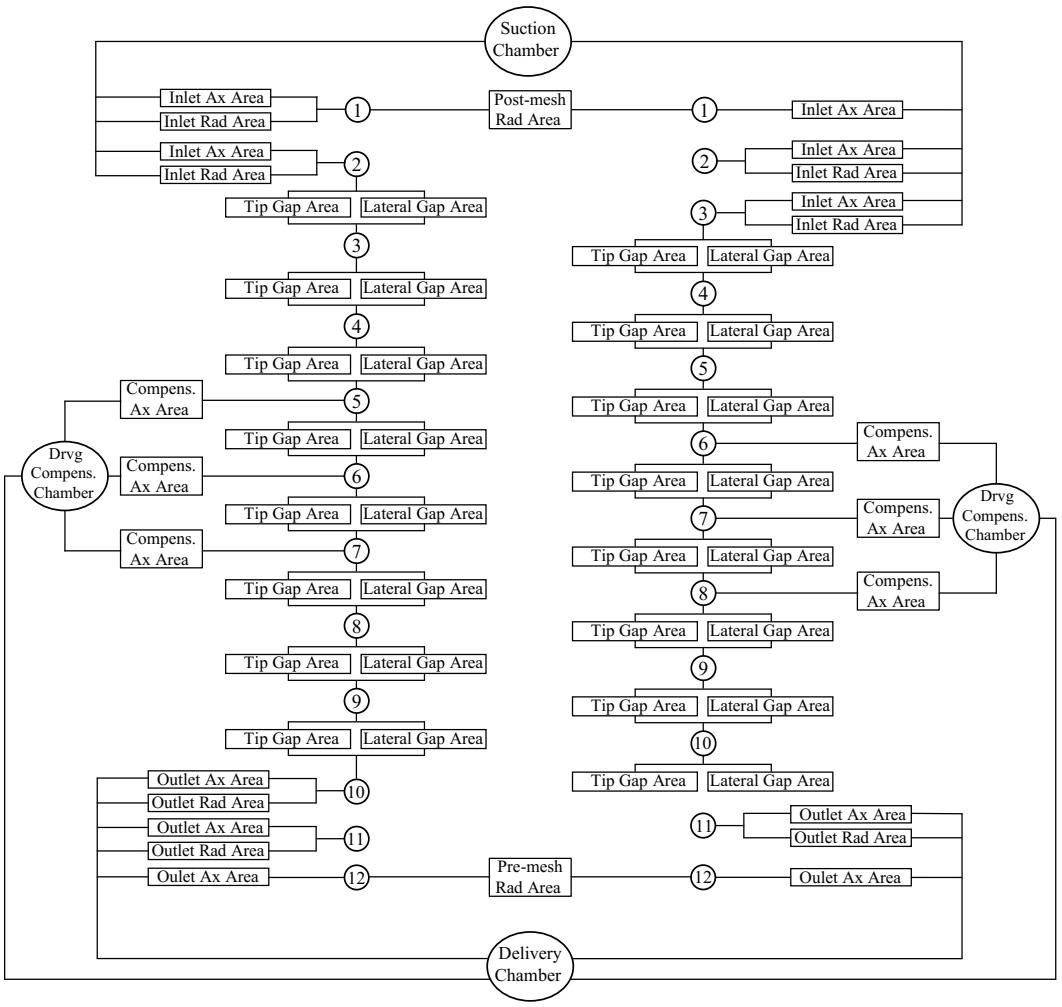

Figure 24: Map of the control volumes implemented within the gear pump LP model and volumes communication scheme

been included assuming a constant volume estimated from the cad models of the piping. Such components communicates among themselves and with the inlet and outlet volumes through constant areas either calculated *a priori* by the analysis of the cad model. Otherwise, the gear vain communicate with the surrounding control volumes through time varying sections calculated step by step within the preprocessing phase. Considering Fig.24, driving and driven gear facing vain mutually exchange lubricant through the variable *pre* and

post respective radial areas. Similarly, the last driving and driven gear vain communicates through the *pre* and *post* orifices on the delivery side. A detailed description of the *pre* and *post* exchanged flowrates has been included within 3.5. Alongside with these radial exchanges, gear vain axially relief pressurized oil toward the inlet chamber through the instantaneous *Inlet Area* exposed to the vain.

Figure 23 also shows that on the balancing plate of the pump studied for the validation, two symmetrical grooves named *Compensation Groove* are included. Such grooves are responsible to axially collect oil from the pressurized vain with the purpose to deliver it to the back-plate grooves. The pressurized oil is here required in order to ensure the balancing plate hydrostatic radial and axial sustainment. Thanks to the gaskets included in the rear face of the plate, the oil leakage toward the suction side is avoided, on the contrary, it is put in communication with the delivery chamber. When the pump works in stationary conditions, the limited pressure difference between the involved volumes do not causes intense oil exchanges ensuring a constant floating actions. It is worth underline that the tip and lateral flowrates between adjacent vanes are calculated only within the pressure arc zone. Furthermore, while lateral areas are considered constant during the simulation and calculated by the preprocessing tool, the tip areas between gear and housing depends on the instantaneous position of the gear and are calculated within the resolver.

The resolver tool works on the basis of the data collected within the pre-processing phase, iteratively resolving the continuity equation for the entire set of volumes. The fundamental outcome is the definition of the equilibrium position of the gears and the instantaneous active pressure field combined to the control volumes flowrates. The resolution of the system for constant angular step lead to obtain the pressure and flowrate oscillations of the control volumes through complete pump revolutions.

3.4.1 *Pre-processing Module*

The preprocessing module has been structured with the main purpose to determine the geometrical features needed to characterize the control volumes. In particular, the main preprocessing outcomes are the calculations of the exchanging areas between adjacent control volumes and the control volumes dimensions themselves.

The module essentially relies on the accurate reproduction of the gearpair equipped within the pump. In this context, the initial part of the tool is devoted to the collection of the basic gearpair geometrical data and of the rack cutter tool adopted for the gear production. Then, the data are processed generating the gears through the reproduction of the cutting process. Aside from a detailed tooth table, the tool creates the Matlab structures where the points constituting the gear profile are properly ordered and stored. Furthermore, with the purpose to straightforwardly generates the balancing plate grooves, the Matlab tool has been put in communication with a 3D cad software by means of a dedicated function. Since one of the final scopes of the LP model is the design of pump improving solution, the tool assumes further relevance when is required the design of several different grooves layout for a same pump. Being the shape of such profiles extremely difficult to describe as parametric function in Matlab, a flexible tool that generates usable data directly from the cad assumes an absolute relevance. The tool basically operates discretizing the grooves profile on the cad environment in a proper number of ordered points and import them as Matlab usable data. Inlet, outlet and compensation grooves are imported from the cad model and reproduced within the preprocessing scripts. Then, the groove profiles are combined with the gearpair profile previously generated.

The nature of the collected data gives the chance to calculate the dimensions of the control volumes and of the exchanging areas for a complete rotation. A dedicated script simulates the gearpair motion discretizing the gears revolution around its axis, in a consistent number of equal angular steps. In particular, the rotation of a singular vain per gear is considered focusing the attention on the relationship with the mating tooth on the other gear and on the vain exposure to the plate grooves. For each angular step, the script is able to calculate the oil volume isolated within the vain and the instantaneous flowrate exchanging areas. Within this context, for the presented LP model a novel method for the axial relief areas and volumes calculation, based on the 2D Matlab meshing feature has been developed.

For sake of clarity, Figure 78(a) shows the instantaneous axial exchanging area exposed to the driving gear reference vain. The black area is the portion of inlet groove that communicates with the oil trapped by the vain and the mating tooth of the driven gear. Zoomed views reported within Figures 78(b) and (c) show the structure of the 2D triangular mesh [67] generated within

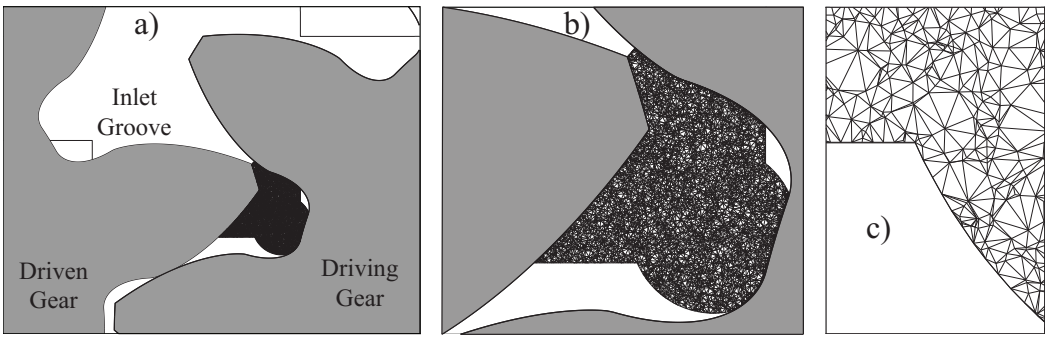

Figure 25: Path of contact and relief groove

the Matlab environment. Despite the resultant exchanging areas result into articulate and irregular profiles, a proper implementation of the triangulation combined to a coherent script programming, gives the opportunity to calculate the exposed area very precisely. Furthermore, the script allows to identify the section perimeter which is a crucial parameter for the section hydraulic diameter calculation. An accurate calculation of the areas for each angular step is particularly important since it allows to reproduce the smooth variation of the area. A poor calculation often results into the generation of discontinuous area profile that may produce numerical errors on the final pressure and flowrates estimation. Nevertheless, the proposed methodology excellently overcome the problem giving absolute accuracy and flexibility. In addition to the axial passage areas, through the same approach it is possible to calculate the gear vain control volumes evolution. As a matter of fact, the calculation of the vain frontal area represents the fundamental aspect for the volume estimation. In fact, for spur gears the trapped oil vain should be calculated by the multiplication of its frontal area for the gear facewidth, while for helical gears the vain volumes might be obtained integrating the frontal area along the helical profile. Then, the preprocessing tool calculates the vain volume derivative through a complete gear revolution.

Once described the calculation method for axial areas and control volumes, it is worth to focus on the calculation of the radial exchange orifices. Figure 26(a) shows an example of the communicating orifice between two facing vain control volumes. The exchange area between the vain is mutually shared between the control volumes. The definition of the *Pre* and *Post* adjectives will be successively provided within Section 3.5. The orifices are rectangular

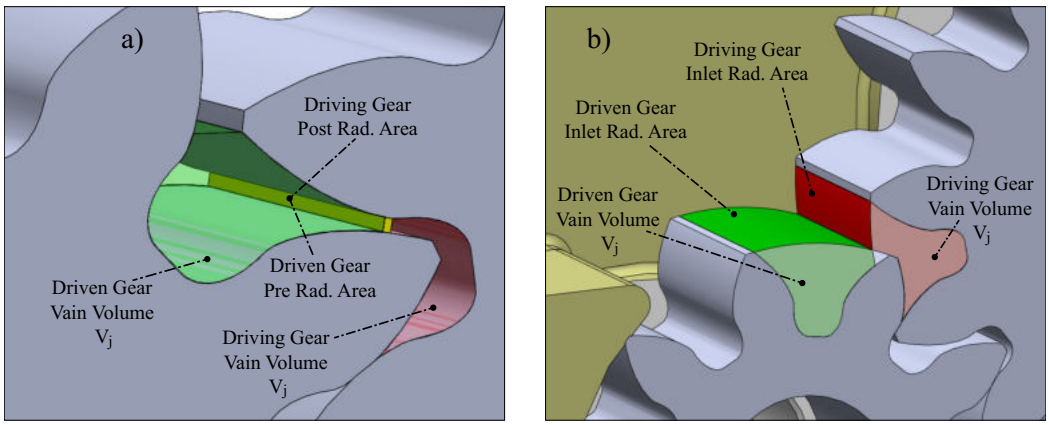

Figure 26: Vain to vain flowrate exchange (a) and two instant of radial flowrate exchange (b) (c)

shaped with long edge equal to the gear facewidth and height calculated considering the minimum distance between the inactive profiles of the meshing vanes. Otherwise, the inlet radial orifices for both driven and driving gear are presented in Figure 26(b). Similarly to the vain to vain orifice, one edge of the passage area is represented by the gear facewidth while the other one is represented by the arc length, or a portion of it, as shown within the picture. For sake of clarity, the same principle may be adopted for the description of the outlet radial areas. Within the control volumes map of Fig. 24, these areas are indicated as *Outlet Rad Area* or *Inlet Rad Area*.

The last passage area calculation performed in the preprocessing phase, concerns the calculation of the lateral orifices. Such sections are calculated by multiplying the lateral gap between gear and balancing plates for the tooth height. It is worth underline that these ports put in communication consecutive vain of the same gear on the pressure arc zone generating lateral leakages.

A great potentiality of the developed model is associated to the possibility to launch the preprocessing module separated from the rest of the code. It descends that, once collected the volumes and passage area values, the model would be executed launching the resolver module changing only the operating parameters. In this way it is possible to contain the computational demands and study several operative conditions.

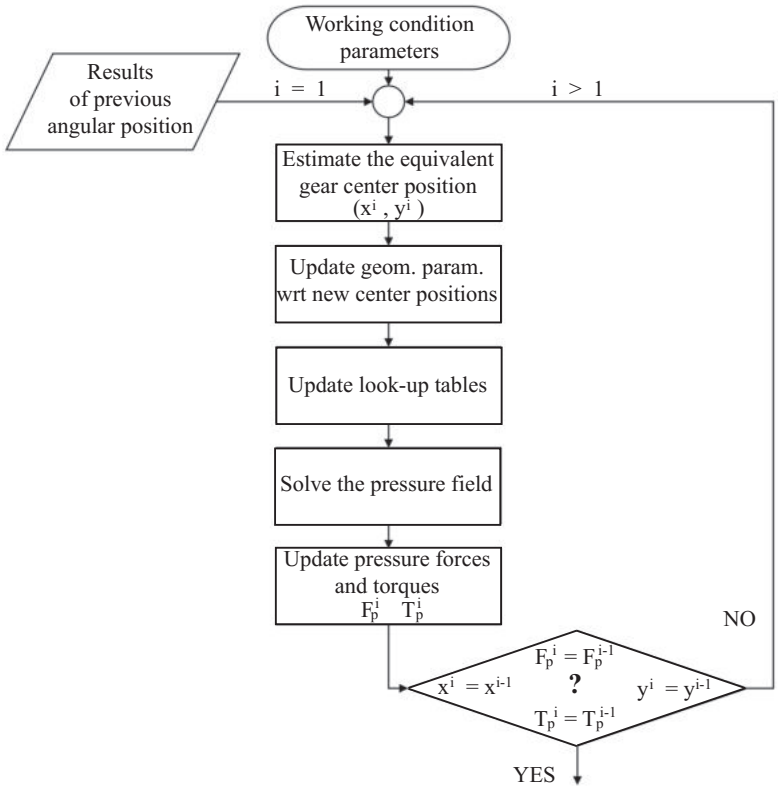

Figure 27: Iterative solution scheme for a given gearpair angular position

3.4.2 *Resolver Module*

The resolver module is devoted to the calculation of the interactions between the control volumes. It allows to characterize the pump fluidynamic behaviour and the loads arising during the pumping operation. It requires, as input data, the geometrical parameters of gearpair, bearing and clearances and the volumes and areas data collected performing the pre-processing module. In addition, it is necessary to provide the pump rotational speed, the inlet pressure and the target delivery pressure. To initialize the resolver, it is necessary to attribute an initial pressure value to the control volumes and the initial position inside the bearings to the gears.

The resolution scheme relays on the iterative procedure described within Fig.27. For a generic angular position of the gear it is possible to inseparably calculate the pressure field inside the pump and the gears instantaneous

position. Since these two aspects directly affects each other, it is mandatory for a simulation tool to perform a bonded calculation of their values. Describing the correlation starting from the gear position, it is clear that the clearance between gear shaft and journal bearings allows the gear to orbit within the bearings, converging to the position that ensure a pressurized meatus and the required fluidynamic sustainment. As a matter of fact, the position of the gear provides a variation of the gap between tooth tips and the pump internal casing which directly causes a leakage flowrate variation. Then, according to the continuity equation 50, the flowrate variation results into a fluctuation of the control volume pressure. Consequently, the pressure loads, arising on the pressurized oil volume, are subjected to a unavoidable variation. Extending the discussion to all the vain of driving and driven gear, it is clear that the entire pressure field and related pressure loads vary generating a different total pressure force that loads the journal bearings. The reaction of the bearing consists in a variation of the oil meatus height capable to sustain the new resultant force. It descends that the gears are assuming a novel equilibrium position, different from the first implemented, that results into a further tip clearance modification.

The straightforward description of the cause-effect process represents a step of the iterative procedure implemented for each angular step. With the purpose to describe the instantaneous equilibrium condition of the pump in terms of pressure field, flowrates, gear position and loading scheme, the continuity equation is solved for the entire set of control volumes in each iteration. From a mathematical point of view, the existence of a set of several control volumes generates a non-linear system of continuity equations which has been treated by means of the *fsolve* Matlab function. As mentioned within previous Sections, the model has been developed with the purpose to deal with the oil Bulk's module variation during the pump operation. For this reason, the Bulk's module equation 54 is solved in each iteration. Furthermore, the flowrate estimation is also subjected to the calculation of the flow number and flow coefficient in every instantaneously active passage area. The flow regime characterization given by the solution of Equations 52 and 53 ensure the coherency of the estimation in every calculation step. The introduction of these updates has shown higher robustness and reliability to the continuity equation solutions.

Figure 28: Frontal view of the test bench where the gear pump has been tested

3.5 EXPERIMENTAL VALIDATION OF THE LUMPED PARAMETER MODEL

The computational model has been developed with the purpose to reproduce the performances of an existing spur gear pump. The coherence of the model results has been evaluated on the basis of the reproduction of the delivery pressure, delivery flowrate and pressure ripple on the outlet pipe. The characterization of such terms of comparison has been performed through a dedicated test campaign where the performances of a benchmark gear pump have been mapped on a test rig. The tests have been performed driving the pump at the required speed with a smooth and contained acceleration in order to do not introduce shocks and overheating of the lubricant. In parallel, through the bench controller, the delivery pressure needs to be lead to the

Figure 29: Pump studied for the LP model validation

target value. Then, when the test condition are achieved, pressure and speed signals are acquired for 30 seconds.

From Figure 28 it is possible to see the frontal view of the test bench and the setup for the measure. The gear pump is mounted on the test bench coupling the pump cover to the bench flange, here the pump driving shaft is connected to the bench driver which is controlled in order to ensure the required pump speed.

With reference to Fig. 28, the suction port of the pump is placed on its right side while the delivery port is on the left. A rigid T-pipe connect the outlet port to the flowmeter and house the pressure sensor on the central joint. After the flowmeter, the outlet pipe end up into the bench tank where the oil is filtered and stored. Apart from the pressure and flowrate sensors, the bench is equipped with an encoder for the pump speed control and a thermal sensor for the oil temperature monitoring. Within the picture are also visible a microphone and four accelerometers mounted with the purpose to monitor the pump NVH behaviour. The data collected by means of such sensors have been employed in a parallel activity on the same pump.

The pump adopted for the activity is shown within Figure 29. With the purpose to show the main components of the gear pump, the picture presents the machine disassembled. Body, balancing plates and covers are made of aluminium alloy, while the shafts are made of tempered 20MnCr5 steel. In order to ensure a steady set of clearances for the entire operation, gear housings

Table 1: Test conditions adopted for the experimental campaign.

Pump Speed (rpm)	Outlet Pressure (bar)	Outlet Flowrate (L/min)
2000	10	29.10
	50	28.55
	100	28.21
	150	28.10
	200	28.26
3000	10	43.09
	50	42.90
	100	42.65
	150	42.50
	200	42.52

have been subjected to a running-in procedure before the test campaign. The gear pump is essentially constituted by two spur gears with equal number of teeth $z = 12$, module $m_n = 2.5mm$ and facewidth $w = 26mm$ that ensure a theoretical pump displacement Cc equal to $14.59cm^3/rev$. The condition tested for the pump performance mapping have been included within Tab. 1. The lubricant adopted on the test rig is an ISO-VG46 oil and it is worth mentioned that during the entire test, the fluid has been maintained at constant temperature of 40°C. The pressure sensor located on the outlet port of the pump has allowed to acquire the operative pressure ripple which stands as one of the most representative indicators of the numerical-experimental correlation. Within Tab. 1 the mean delivery pressure values, measured by the sensor, are reported. Figure 30(a) shows the pressure ripples measured at pump speed of 2000 rpm while displays in 30(b) the data collected at 3000 rpm. In each subfigure, the curves are representative of the delivery pressure ripples measured at different target outlet pressures. With the purpose to give robustness to the ripple comparison, the experimental signals have been cleared out of the mean pressure value. Since the pump was working in single contact, the waves present a number of positive and negative peaks equal to the gear number of teeth.

The model validation procedure has in its initial step the reproduction of the gearpair through the gear tooth tables of the tested pump. In second instance,

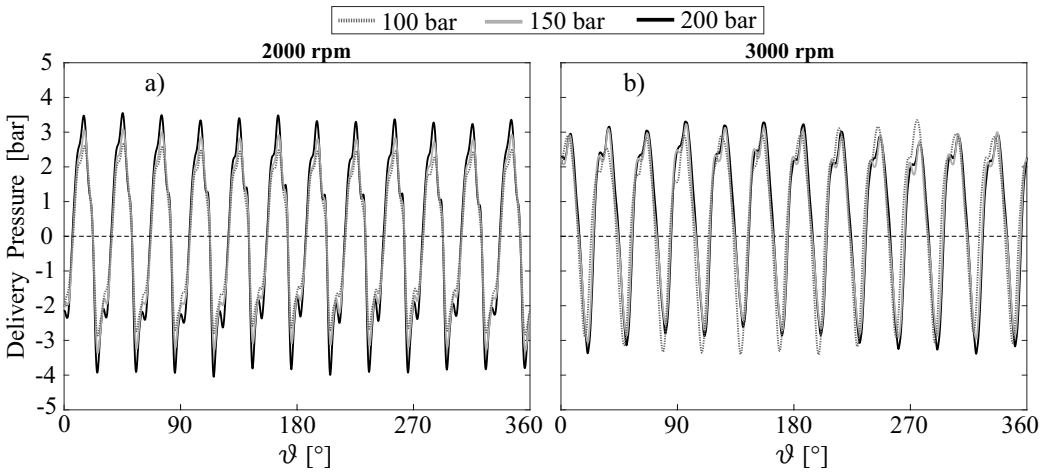

Figure 30: Delivery pressure ripples measured at three different delivery pressure at 2000 rpm (a) and 3000 rpm(b)

balancing plate grooves have been imported from the pump cad model with the purpose to activate the preprocessing calculation phase. As mentioned before, the preprocessing tool has lead to generate the structures and matrix containing volumes and exchanging areas necessary for the resolver module. Aside from the orifices calculation, preprocessing phase requires the introduction of the complete set of geometrical input parameters that characterize the tested pump. In particular, in this phase it is mandatory to insert the stationary internal clearances between rotating and stationary bodies. Such set of parameters has been obtained through the measurement of the tested pump components by means of a measuring machines on the metrological laboratory of the pump manufacturer. Finally, the operative conditions have been setted through the generation of the structure including oil characteristics such as viscosity and reference Bulk's modulus at test temperature, pump speed, target delivery pressure, shaft material data.

Aside from a certain number of input parameters derived from measurement and operative data, there is a set of parameters devoted to the calibration of the model. In particular, the validation of the model has been performed through the tuning of the critical flow numbers λ and flow coefficients Cq. To ensure a fine calibration of the model, such parameters have been specified for different families of passage area. The map of the exchange orifices shown within Fig. 24, gives the chance to identify the mentioned families of areas. With reference

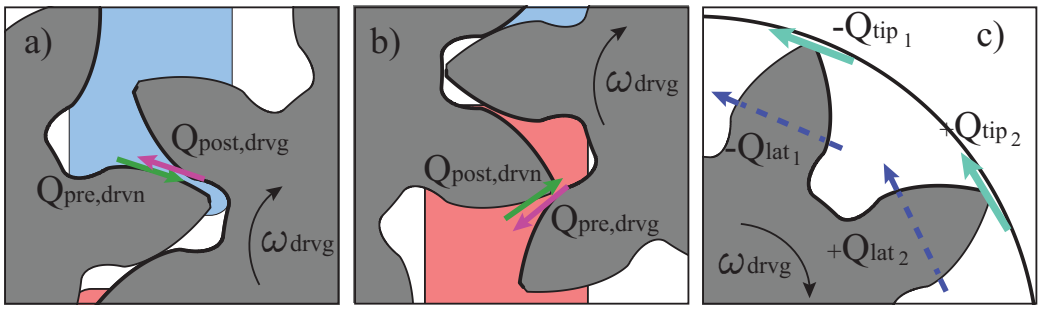

Figure 31: Vain-to-vain oil exchanges: *pre* and *post* flowrates in two different meshing instant (a), (b) and schematic representation of tip and lateral flowrates (c)

to Fig. 24, it is worth to describe the zone of application of the parameters. The subscript *sd* are referred to the axial and radial exchange areas between vain and suction or delivery chambers. An example of the radial suction side orifice has been depicted in Fig. 26(b). The indication *sen* describes all the exchanging areas between delivery and suction chambers with the piping while *cmp* is related to the compensation grooves axial exchange. A special focus is given to the tip and lateral orifices named *tl* and to the vain-to-vain exchange areas described by the subscript *pp*. Figure 31(a) and (b) gives the chance to understand the reference framework for the calculation of the *pre* and *post* radial flowrates within the meshing zone. The schematic view of the radial orifices reported in Fig. 26(a) also helps in the description. Considering driving and driven mating vain and the enumeration framework, the subscript *pre* is given to the flowrates exchanged through the first portion of the vain. On the contrary, the subscript *post* is assigned to the second portion. It descends that for the adopted reference scheme, the *pre* flowrates of the driving gear are exchanged with the *post* orifices of the driven and viceversa. Since the reference vain for the two gears are shifted of one angular step, the flowrates are shifted of such angular period with opposite sign. Otherwise, tip and lateral flowrates are exchanged by adjacent vain along the pressure arc. The flowrate scheme reported within Figure 31(c) helps for the explanation of the leakages calculation. Since the reference vain is completely entered in the pressure arc zone, it may exchange oil with the adjacent vain through the tip and lateral gap. The flowrates that enter within the control volume are considered with positive sign while the exit flows are considered negative. For

these vain control volumes, the model calculates a flowrate balance in each angular step. The lateral orifices are rectangular shaped and are characterized by one edge equal to the tooth height and the other one equal to the axial gap between gear flank and balancing plate.

Model validation has been carried out considering as reference test condition the 2000 rpm and 100 bar of target delivery pressure. For sake of clarity, the target pressure implemented within the model has been set to 91 bar, since the value measured by the pressure sensor has shown a consistent discrepancy with respect to the target value of the test rig. To initialize the model tuning, the value of Cq has been set to 0.4 for the entire set of orifices. With same strategy, λ_{crit} has been set to the standard value 1000. In first instance, the results of the initial run already show the consistency of the model in terms of pressure and flowrate mean value estimation. As a matter of fact in its initial run, the model has shown 8% and 10% underestimation errors on delivery flowrate and pressure respectively. On the contrary, the pressure ripple shows a strong mismatch on the waveform and on the amplitude. It descends that the flow parameters tailoring is mandatory to diminish the mean value errors and consistently reproduce the internal phenomena of the pump.

To properly introduce the flow parameters values, is here presented a sensitivity analysis to the modification of such parameters. In particular, Fig. 32 shows the influence of the modification of the flow parameters of the tip and lateral orifices. For sake of clarity, Fig. 32(a) presents the comparison between the experimental and the numerical pressure ripple for two angular periods while Fig. 32(b) shows the delivery flowrate ripples for a singular period. Among numerical results are also presented the outcomes of the first run. Figures 32(c) and (d) represent the vain pressurization through a complete rotation of the driving and driven gear respectively. The analysis of the results is completed by Fig. 33 which shows the comparison between the tip and lateral flowrates calculated with the different flow parameters. The strong increment of Cq_{tl} acts as a reduction of the orifices constriction. It results into a diminished pump pressurization, observable from delivery pressure drop, which enlarge the error until 10%. Figures 33(a),(b) highlight the increment of the tip leakages that are responsible of the reduction of the mean delivery flowrate shown in Fig. 32(b). The reduction of the pressurization is also notable within Fig. 32(c) and (d) where the pressure peak shown in the meshing zone is heavily reduced as well as the mean vain pressure. It is worth underlining

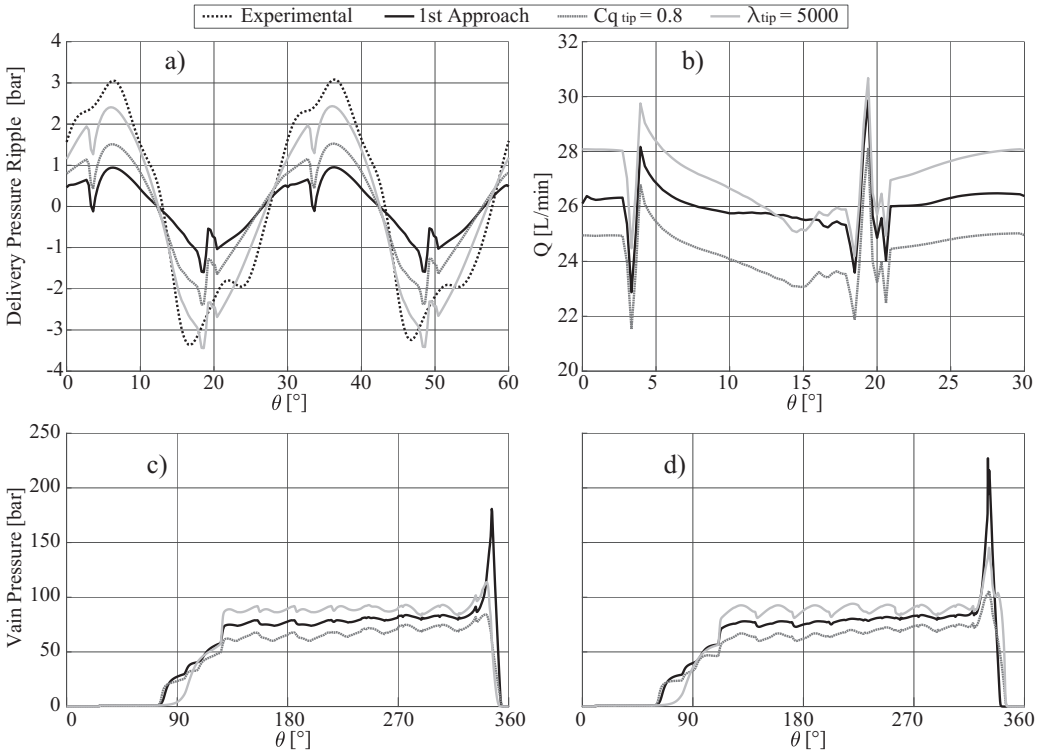

Figure 32: Numerical results calculated varying the tip and lateral orifices flow coefficients. Comparison between experimental and numerical pressure ripples in two angular period (a) and comparison between numerical delivery flowrates in one angular period (b)

that the peak shown from the first approach simulation appears as an unreal phenomena caused by the numerical assumptions. On the contrary, the increment of λ_{tl} from 1000 to 5000 ensures the improvement of the mean values of delivery pressure and flowrate. The numerical errors calculated from the comparison with the experimental values are reduced to 2.6% and 3.9% on the pressure and on the flowrate respectively. The λ_{tl} increment acts as an increment of the threshold that trace the transition from laminar to turbulent regime. Maintaining the flow in laminar regime, the magnitude of the leakages decrease, as shown within Fig. 33, acting as a sealing effect on the pump. The graphical comparison shows that the wave form of pressure ripple is similar to the first approach results with an increased amplitude. However, despite the peak to peak amplitude slightly differs from the experimental, the ripple

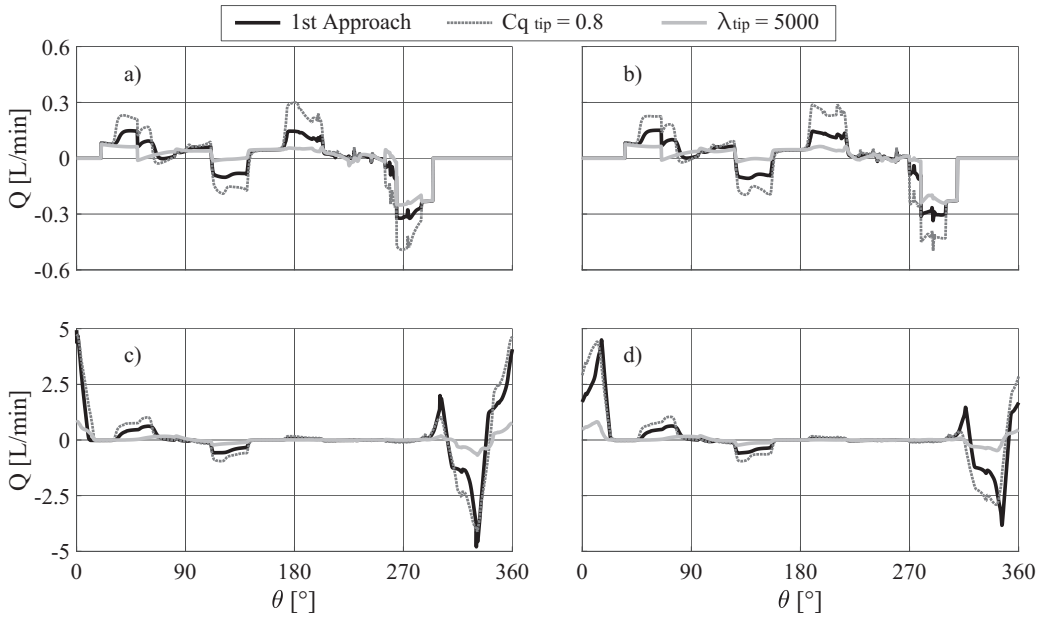

Figure 33: Comparison between tip and lateral exchanged flowrates calculated varying the tip and lateral orifices flow coefficients. Results for the driving gear (a), (c) and for the driven gear (b), (d)

presents some unexpected spikes. The focus on the vain pressurization shows the mean pressure increment paired with a pressure peak reduction.

In second hence, the focus has been put on the influence of the flow parameters on the delivery and suction orifices. For the scope one simulation has been performed increasing Cq_{sd} from 0.4 to 0.8 keeping unaltered the other parameters while the second one has been carried out reducing λ_{sd} from 1000 to 50. As a matter of fact, the Cq_{sd} increment reduces the obstruction on the sections involved while the reduction of λ_{sd} causes the transition to turbulent regime for the entire flowrate exchange. The results of the Cq_{sd} increment is a 1.4 bar reduction of delivery pressure and 0.3 $L/minmin$ of delivery flowrate with respect to the initial simulation. The comparison of the pressure ripples included within Fig. 34(a) shows that the modification improve the pressure ripple amplitude. However, it is also possible to observe that the improvement ensured by the λ_{sd} modification is greater and reduces considerably the discrepancy on the pressure ripples. Within this context, the mean values of outlet pressure and flowrate increase getting closer to the target

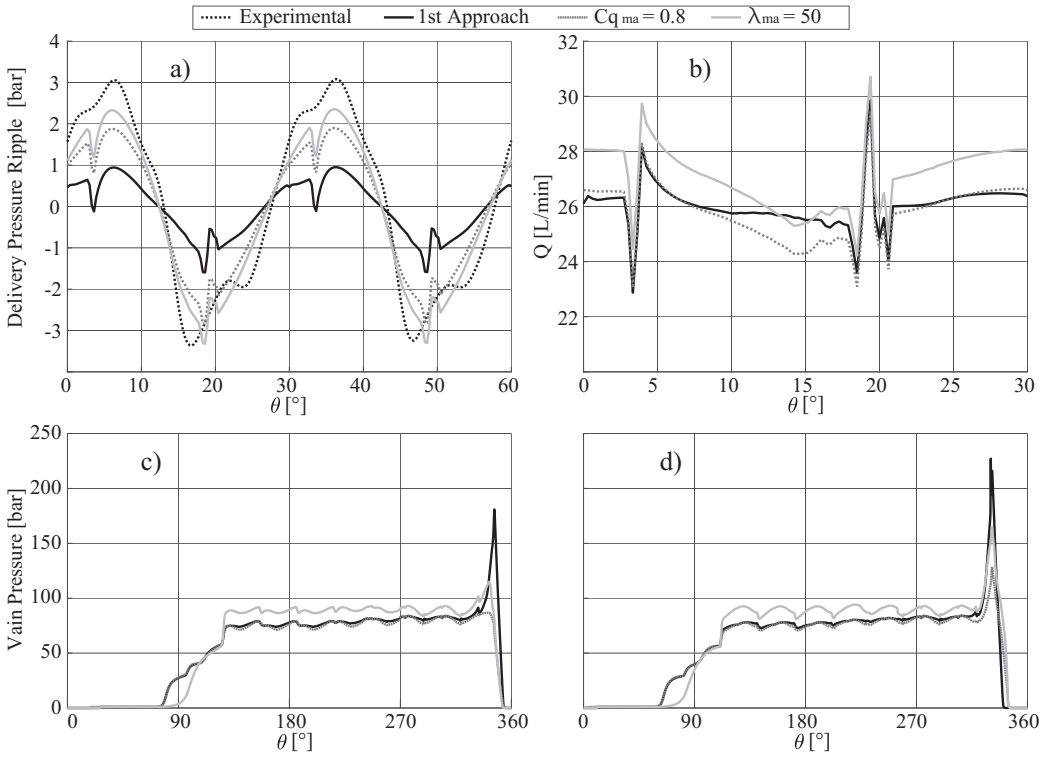

Figure 34: Numerical results calculated varying the delivery and suction orifices flow coefficients. Comparison between experimental and numerical pressure ripples in two angular period (a) and comparison between numerical delivery flowrates in one angular period (b)

values. The errors on pressure and flowrate achieve 2.5% and 3.8% respectively. In terms of pressure peak, Fig. 34(c) and (d) highlight that the Cq_{sd} increment shut down the pressure peak of the meshing zone on the driving gear and reduce the peak on the driven. Then, λ_{sd} reduction shows peak reduction with vain pressurization increment followed by higher fluctuation. Despite results shows the improvement on the correlation, Figures 35(a) and (b), reveal strong and unreasonable flowrates fluctuations in the lubricant exchange from vain to the deliver chamber control volume. The impact of the turbulent regime is particularly notable on the radial exchange 35(b). It descends that a small reduction of λ_{sd} may have positive effect on the increment of the control parameters and of the pressure ripple amplitude while Cq_{sd} should be slightly reduced to avoid contrary effect.

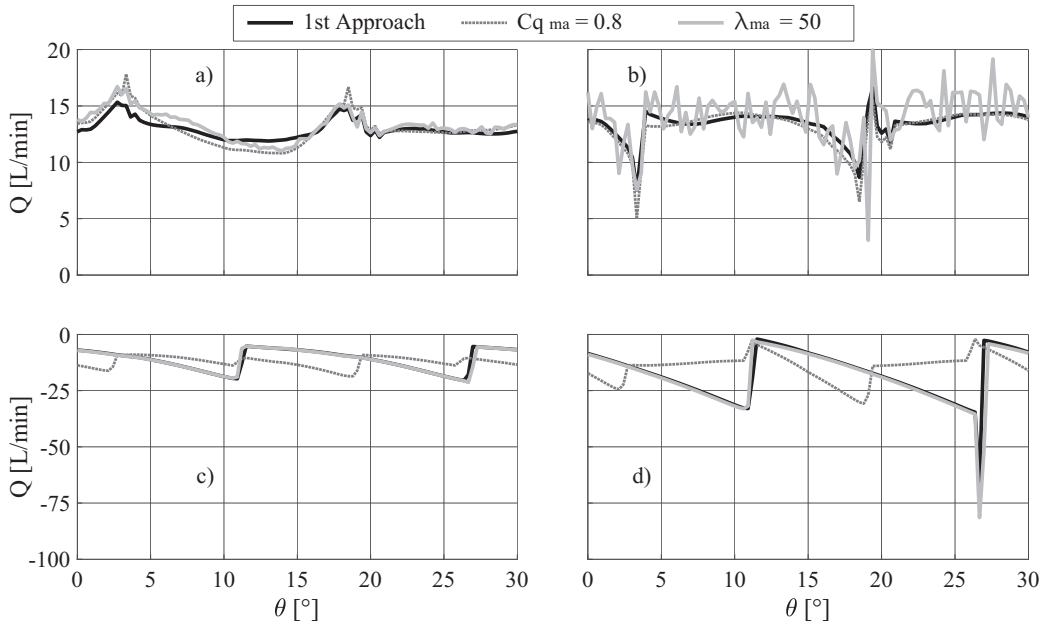

Figure 35: Comparison between exchanged flowrates calculated varying the delivery and suction orifices flow coefficients. Axial flowrates with the delivery chamber CV (a), radial flowrates with the delivery chamber CV (b), axial flowrates with the suction chamber CV (c) and radial flowrates with the suction chamber CV (d)

Following a strategy similar to the previously mentioned, for the *pre* and *post* orifices the related Cq_{pp} has been set to 0.8 while λ_{pp} reduced to 50. The effect of the Cq_{pp} increment follows the results observed for the previous simulations reducing the flowrates, the delivery pressure mean values and the vain pressure peaks. On the contrary, the augmented flow coefficient produces an higher pressure fluctuation, also visible on the vain pressurization, combined with a good reduction of the pressure peaks. The comparison is observable within Fig. 36. The phenomena might be correlated to the increment of the *pre* and *post* flowrates magnitude shown in Fig. 37. The impulsive nature of such radial flowrates is caused both by the high pressure differences between vain control volumes and by the narrow orifices. The constraints reduction given by Cq_{pp} permits higher magnitudes. The reduction of λ_{pp} increments the outlet reference parameters reducing the error to 2.6% on the outlet pressure and 3.9% on the flowrate. The reduction shows an increment

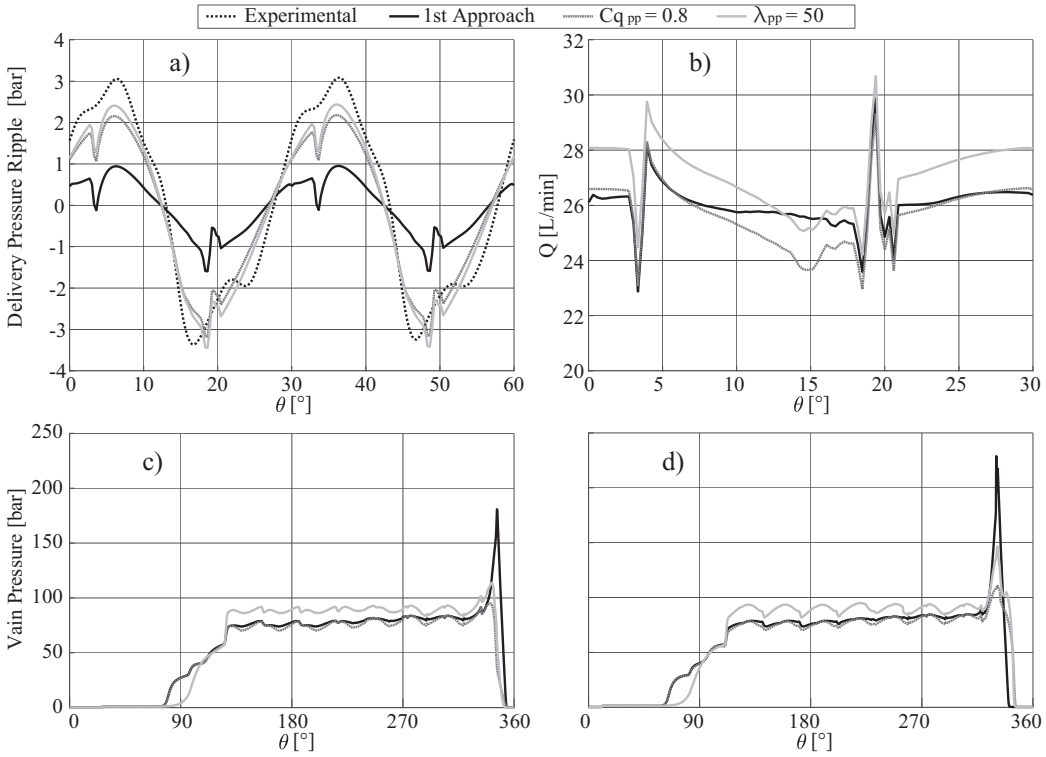

Figure 36: Numerical results calculated varying the pre and post orifices flow coefficients. Comparison between experimental and numerical pressure ripples in two angular period (a) and comparison between numerical delivery flowrates in one angular period (b)

on the pressure ripple amplitude that reduce the error to the 11%. The effect on the *pre* and *post* flowrates is admissible without showing non-physical phenomena. Furthermore it results into a reliable containment of the pressure peaks. It descends that a slight increment of Cq_{pp} from the 0.4 initial value may be profitable for the scope. In parallel the reduction of λ_{pp} will help the transition to the turbulent regime.

Since the pressure differences between compensation chambers, gear vain and delivery chamber control volumes are extremely low, the flowrates calculated in each simulation have not shown sensible differences. A dedicated tailoring procedure of the flow parameters Cq_{cmp} and λ_{cmp} has been performed but it has not shown influence on the reference parameters. On the contrary, the analysis of the piping orifices has given relevant results. In partic-

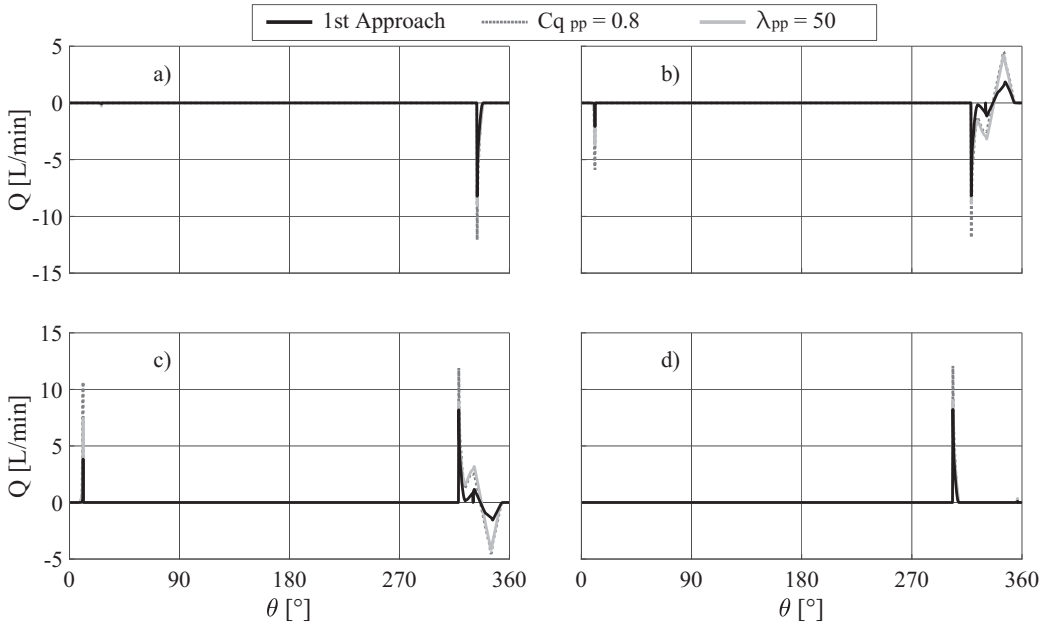

Figure 37: Comparison between exchanged flowrates calculated varying the *pre* and *post* orifices flow coefficients. Flowrates exchanged from the driving gear on the *pre* side of the reference vain (a), on the *post* side of the reference vain (b), flowrates exchanged from the driven gear on the *pre* side of the reference vain (c) and on the *post* side of the reference vain (d)

ular, since the circular shape of the orifices and the diameters implemented seem to barely constraint the flow, the dedicated Cq_{sen} has been set to the 0.8 value. In parallel, to ensure the laminar flow for the entire simulation toward such orifices the λ_{sen} value has been set to 10000. The first important result is visible on Fig. 38(a). Aside from the pressure ripple amplification, the numerical pressure spikes, seen among previous results, have been considerably attenuated. Moreover, the mean delivery pressure has been increased from the initial numerical value, achieving 88.9 bar with a 2.3% of error. Then, the delivery flowrate has been increased to 27.1 L/min with a 3.9% discrepancy respect the reference value. However, in terms of vain pressurization, despite the waves assume a more regular form, the pressure peak on the driven gear almost achieve the original value.

The sensitivity analysis here described has allowed to confirm the strong improvement introduced with the novel flowrate calculation method. In particular,

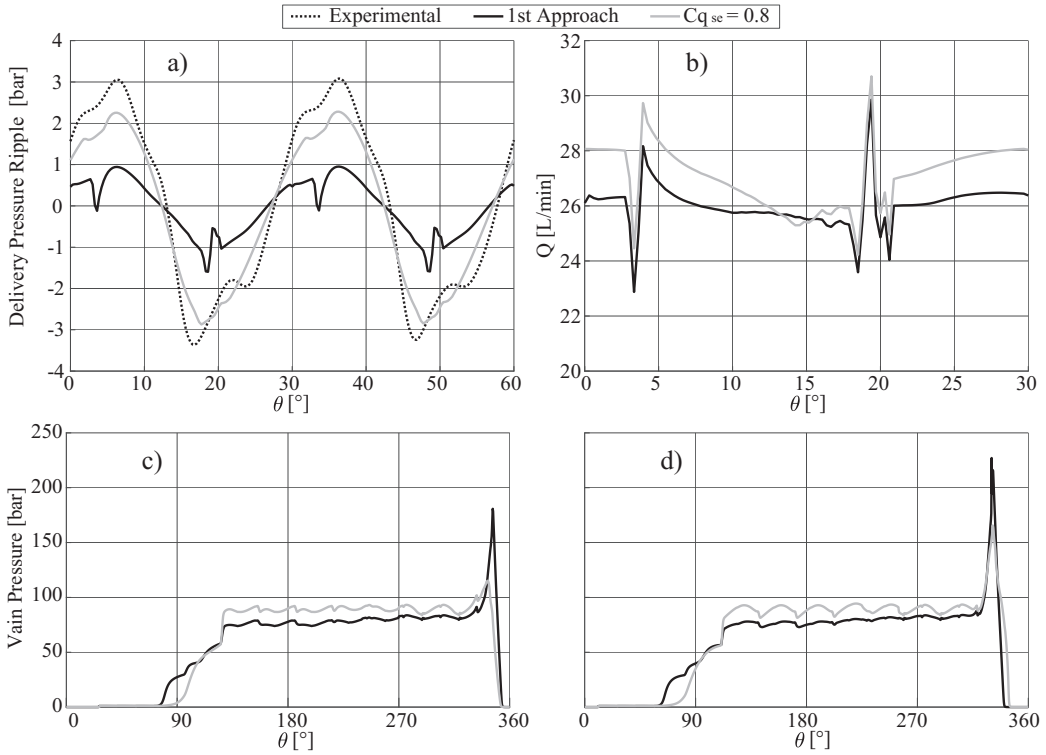

Figure 38: Numerical results calculated varying the sensor and piping orifices flow coefficients. Comparison between experimental and numerical pressure ripples in two angular period (a) and comparison between numerical delivery flowrates in one angular period (b)

Table 2: Set of flow parameters implemented within the validated model

	Reference Orifice				
	tl	sd	pp	sen	cmp
Cq	0.35	0.55	0.65	0.80	0.80
λ	4000	5000	50	1000	10000

it descends that in order to ensure a proper description of the phenomena, the calibration of the flow parameters requires a coherent balancing of the mutual effect of their variations. The LP model tuning has required a great number of

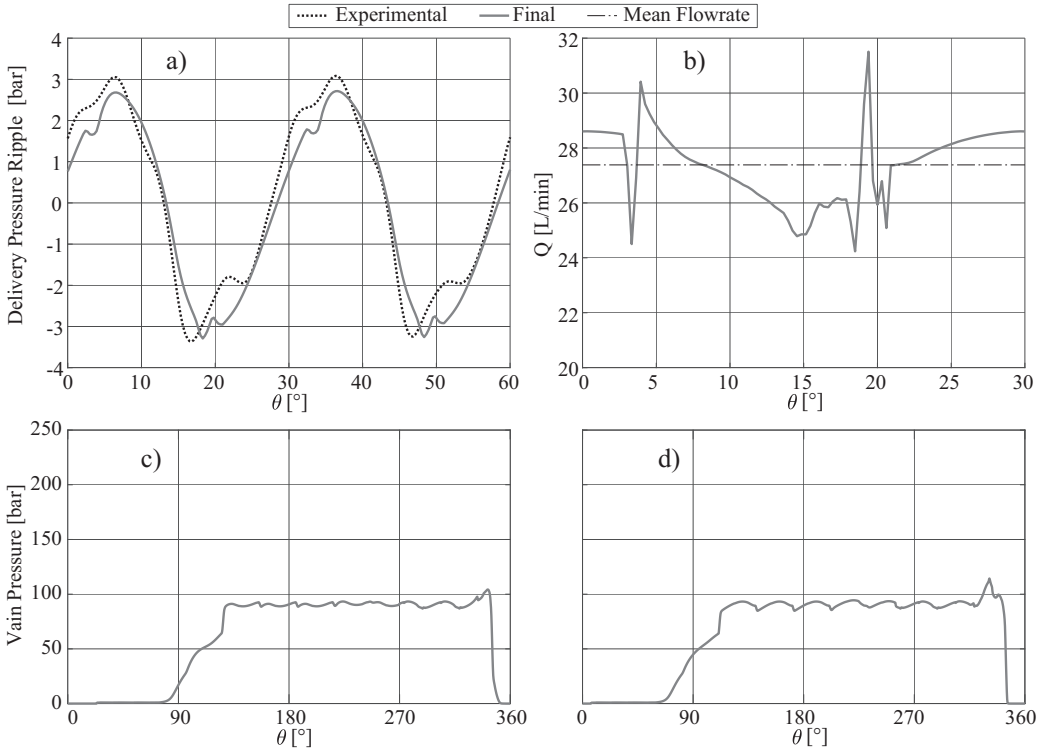

Figure 39: Results of the validated model. Comparison between experimental and numerical pressure ripples in two angular period (a), numerical delivery flowrates in one angular period (b), vain pressurization in a complete pump rotation for the driving gear (c) and driven gear (d)

simulations that, for sake of brevity, have been omitted from the dissertation. It is worth noticing that the computational demand of each simulation has been consistently reduced thanks to the model structure. The definitive set of flow parameters has been included within Table 2. As general rule, the entire set of flow coefficients has been incremented from the first approach 0.4 value except for Cq_{tl}. Such strategy has been implemented pursuing the containment of vain pressure peak incrementing the mean pressure value. In parallel the flow numbers have been incremented in almost all the orifices with the purpose to ensure a turbulent regime transition as smoother as possible. On the contrary, λ_{pp} has been set on the minimum admissible value in order to certainly generate a turbulent flow throughout the vain-to-vain radial orifices.

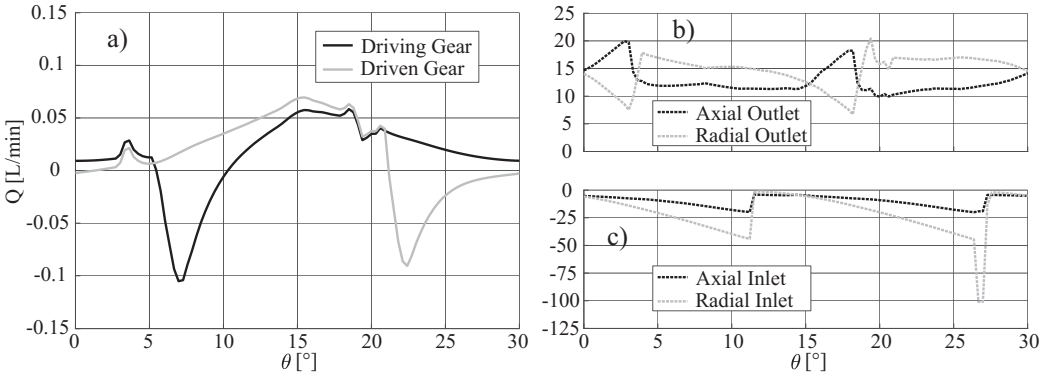

Figure 40: Comparison between calculated compensation flowrates (a), axial and radial flowrates excganged by gear vain with the outlet chamber (b) and inlet chamber (c)

For the reference condition considered during the validation procedure, the ultimate flow coefficient set has led to obtain a 2.2% underestimation discrepancy on the measured delivery flowrate and a 2.3% overestimation on the mean delivery pressure. Within Fig. 39(a) is reported the comparison between numerical and experimental pressure ripple. As can be noticed, the model reproduce the measured waveform with slight differences while the peak-to-peak amplitude discrepancy has been contained on a residual 4%. The delivery flowrate ripple calculated in an angular step reported in Fig. 39(b) shows the waveform generated by the model and the position of the mean value. The calibration of the parameters has allowed to obtain the vain pressurization curves included within Fig. 39(c) and (d). The pressure peak has been contained on both driving and driven gear, reproducing a coherent waveform.

In order to ensure a complete overview of the monitored results, within Fig. 40(a) the flowrate exchanged by compensation chambers control volumes have been reported for driving and driven gear. As previously mentioned, the stability of the adjacent CV pressure generates low flowrates. Within Fig. 40 are also included the flowrates exchanged toward outlet chamber (b) and intlet chamber (c). The calculated waveforms have coherent shape without strong perturbation as shown in Fig. 35. Within the angular period are visible two main discontinuities on both axial and radial flowrates which are linked with the suction or delivery of lubricant by driving and, subsequently, by driven gear. Tip flowrates are reported in Fig. 41(a) while lateral flowrates are reported

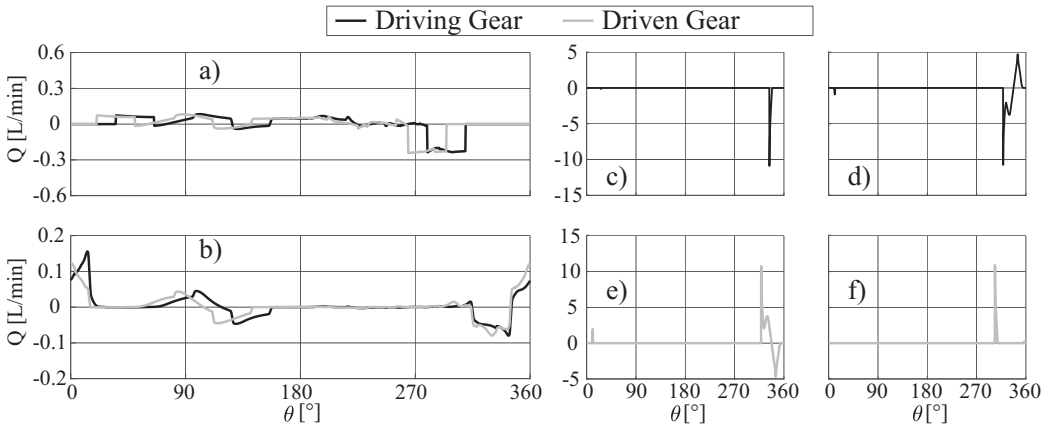

Figure 41: Vain to vain exchanged flowrates. Tip leakages (a), lateral leakages (b), *pre* and *post* flowrates respectively calculated for the driving gear (c), (d) and for the driven gear (e), (f)

in Fig. 41(b). The concurrent reduction of Cq_{tl} and increment of λ_{tl} shows a slight fluctuation of the leakages. Particularly evident are the vain leakages from the pressurized vain to the outlet chamber located on the last quarter of the graphs. The negative sign is due to the assumed sign reference system which attributes negative sign to the CV outgoing flows. The subfigures from (c) to (f) show the magnitude of the *pre* and *post* flowrates that conserve their impulsive behaviour.

To conclude the validation procedure, the model has been deployed for the pump performance mapping. With reference to the experimental results, the pump has been simulated at two nominal speeds varying the target delivery pressure from 50 to 200 bar. The experimental and numerical volumetric efficiencies have been evaluated considering as target flowrate the experimental value measured imposing 10 bar of target delivery pressure. Figure 42 shows the efficiency map at 2000 and 3000 rpm. As previously mentioned, the model is capable to reproduce the target flowrate with a slight underestimation error. Even if the difference are notable for the entire set of performed simulations, the model is capable to reproduce the efficiency increment observed from 2000 to 3000 rpm condition. Furthermore, it reproduces the slight efficiency improvement observed increasing the pressurization. The discrepancies noticed during the validation procedure might be imputable to the lack of information on the lubricant employed by the pump manufacturer.

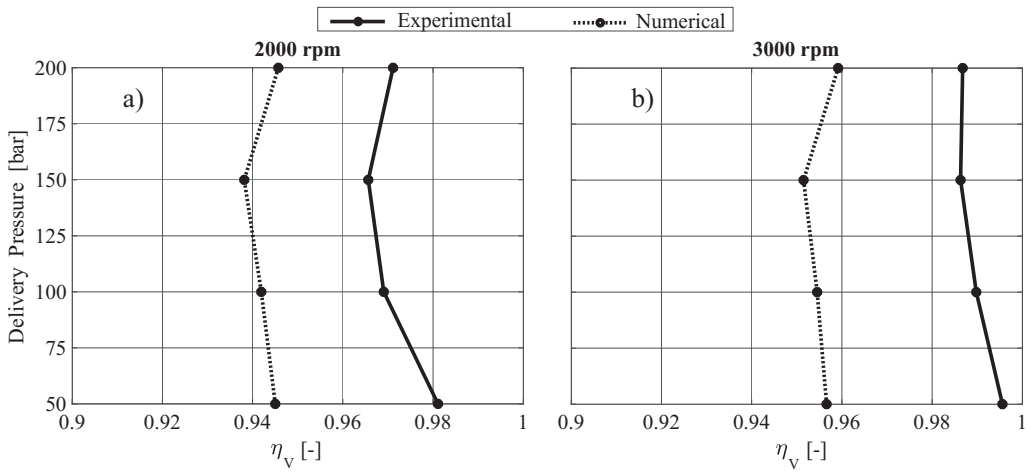

Figure 42: bla

3.6 PERFORMANCE IMPROVEMENT OF EXTERNAL GEAR PUMPS: APPLICATION OF THE LP MODEL

The validation procedure detailed within Chapter 3.5 has highlighted the consistency of the model for the representation of the gear pump performances, obtained thanks to the implementation of the flow coefficient approach to the flowrates calculation. Aside of representing a robust tool for the numerical reproduction of existing pump characteristics, it is also employable for the prediction of the performances of novel pump layouts. Within this context, the model might deploy its fundamental contribute on the containment of sampling and operative tests and, consequently, to the energy and material waste reduction. Within the current chapter, one application of the model for the performance improvement of a gear pump is presented and discussed. Since the gear pump object of the activity was equipped with helical gears, within the model the analysis of such gears besides spur type has been implemented. The salient data of gears and pump have been included within Tab. 3. It is worth noticing that the pump involved in the study was already subjected to the running in procedure and, consequently, the internal gap between gears and casing were substantially different from the values obtained from the stack-up analysis of the executive drawings. With the purpose to ensure an higher level of coherency to the model, the internal profiles of the housing have

Table 3: Test conditions adopted for the experimental campaign.

Parameter	Value	Unit
z	10	-
m_n	4.23	mm
β	13.30	deg
W	26.0	mm
Cc	84.53	cm^3

been measured by means of a measuring machine and implemented within the model.

3.6.1 *Characterization of the Pump Performances*

In order to define the benchmark performances of the pump, a preliminary test campaign has been performed. The pump has been tested at three rotational speed and eight crescent values of delivery pressure. Furthermore, each test condition has been repeated three times with the purpose to achieve representative mean results. Within Fig. 43 the performance map with 3 different pump speed is reported. The efficiency has been calculated considering as reference value the delivery flowrate obtained with the lowest tested pressure. It is worth noticing that the pump seems to increase the efficiency increasing the delivery pressure and the behaviour is repeated for all the velocities. Such phenomena tends to be in contrast with the expected results where the increment of the delivery pressure may causes the increment of the leakage flow and the internal frictions. A reasonable hypothesis elaborated for the explanation of the efficiency recover, relies on the ability of the gearpair to minimize gears backlash and gaps between gears and housing in the pump suction side, thanks to a certain amount of shaft bending that occurs at high pressure. In the attempt to coherently represents the pump behaviour, the model has been updated in this case study including the bending calculation within the resolver module. Shafts have been considered as isostatic supported beams and the resolution of the structure has lead to define the shaft displacement. Then, the value has been included within the gap calculation of the resolver module. The correct

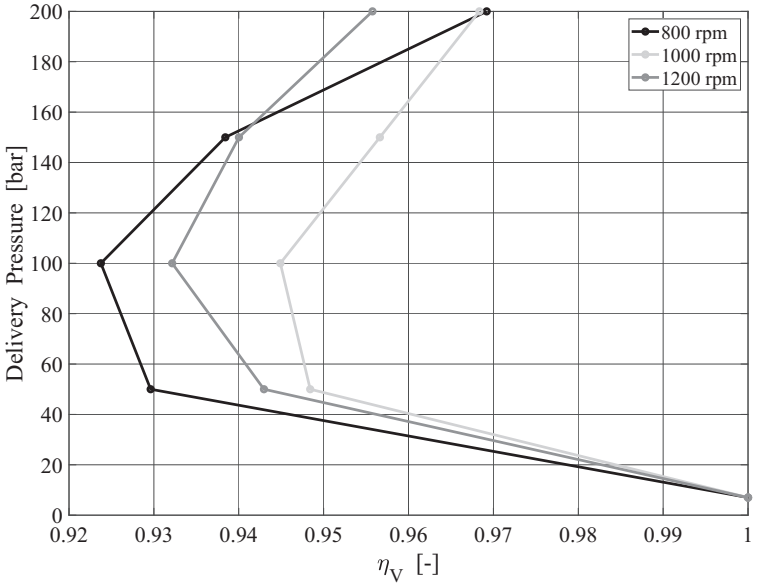

Figure 43: Performance map of the tested pump

definition of the internal gap is fundamental to properly describe the flowrates between gears vain and finally obtain the pump behaviour.

As formerly described, the LP model application starts with the balancing plate axial grooves importation from the 3D cad model. Within Figure 44 it is possible to see how the gear faces are exposed to the balancing plate grooves at the same instant. The figures represent the frontal and the rear face of the gear which are shifted by the helix angle β. The frontal face present an isolated vain while the second has the possibility to exchange oil with the outlet groove. Contemporaneously, on the other side the first vain is already opening to the suction chamber while the second is completely enclosed. The isolation phasing is the most relevant aspect in the groove design since its correct calculation lead to avoid excessive pressure peaks in the meshing zone and incomplete pressurization at the same time.

As mentioned within the validation description, by means of the pre-processing tools the gear geometry has been reproduced on the basis of the tooth table and then passage areas and control volumes dimensions have been calculated for the entire pump revolution. Then, the validated flow parameters set has been included. With the purpose to evaluate the model coherency with a pump different from the one implemented for the validation, the model

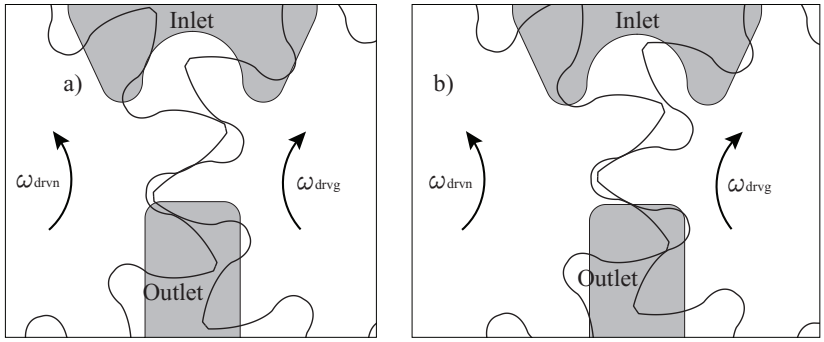

Figure 44: Helix gear exposed to the balancing plate grooves frontal view (a) and rear view (b)

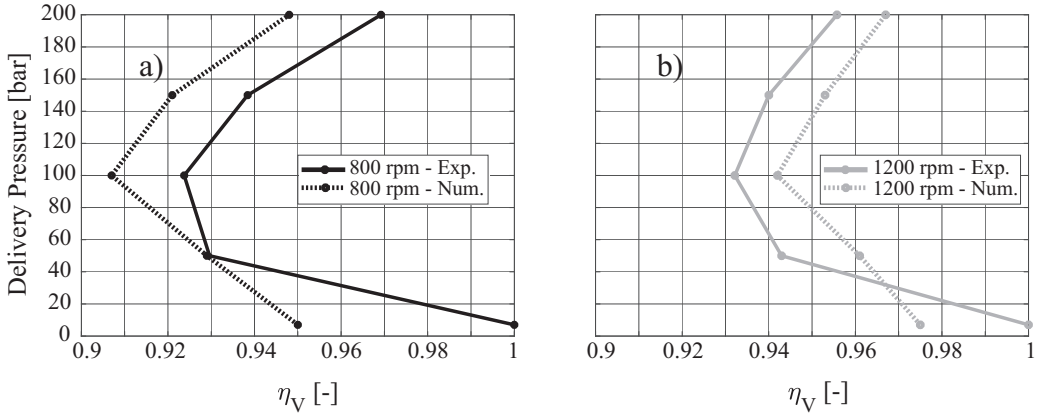

Figure 45: Comparison between numerical and experimental results at 800rpm (a) and 1200rpm (b)

has been initially launched reproducing the operative conditions. The results are reported within Fig. 45. As well as for the operative efficiency, the numerical efficiency has been evaluated considering the result of the operative measurement at the lowest delivery pressure as reference. The maps reported within the figures show that the model is capable to coherently predict the pump behaviour with minor errors, proving that the assumption on the gap tightening consequent to the shaft bending was valid and accurate.

Since the preliminary simulations have further confirmed the reliability of the proposed model, the results have been taken into account constituting the benchmark performances for the design improvement.

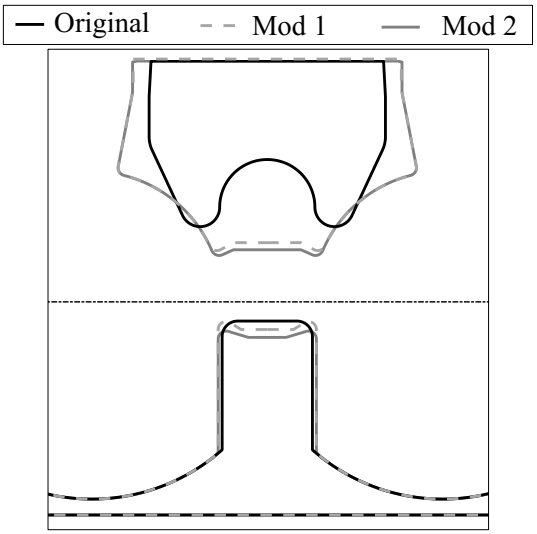

Figure 46: Implemented designs of the balancing plate relief grooves

3.6.2 *Design of Improvement Solutions*

The first step of the design improvement has been represented by the study of a different set of relief grooves with the purpose to enhance the oil pressurization within the meshing zone. In particular, the original grooves layout presents a wide bridge zone on the balancing plates, combined with tight grooves on the outlet side. This particular geometry ensure a strong sealing of the vain CVs within the meshing zone and simultaneously extends the pressure arc. It descends that the pump achieve a great volumetric efficiency. On the other hand, increasing the speed or the pressurization may cause higher internal loads. Through a groove improvement it is possible to reduce the sealing and the consequent loads peak, allowing the pump to work at higher speed elaborating equal delivery flowrate with lower displacement. To pursue this strategy, it is worth start from the analysis of the theoretical bridge width. Such parameter might be calculated considering the the height of the active contact segment. It is worth mentioning that for the current activity, the bridge width for a full meshing coverage has been calculated equal to 11.10 mm.

The relevance of such parameter relies on its influence on the vain CV pressurization. In fact, the lubricant carried out from the outlet chambers through the meshing zone, increases its pressurization resulting entrapped within

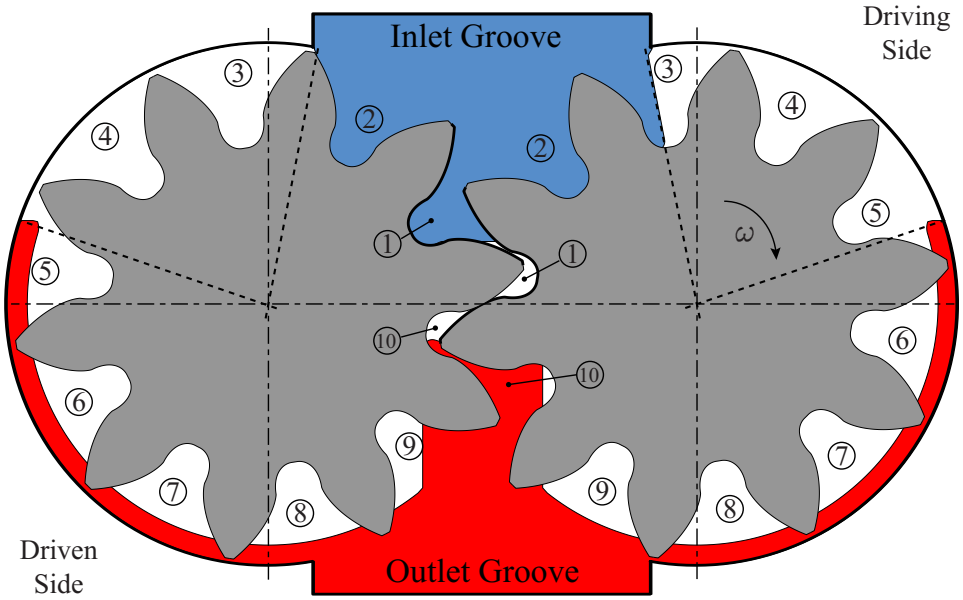

Figure 47: Schematic view of the the *Mod2* configuration with reference to the gear vain control volumes enumeration

mating teeth and the bridge surface of the balancing plates. The extension of the bridge and the position of its initial and terminal edges directly influence the pressure peaks. Furthermore, since highly pressurized oil is squeezed within the suction volume, strong perturbations and air bubbles may affect the pump suctioning phase. The oil entrapping and releasing timing assumes a crucial role to prevent hazardous cavitation phenomena. Displacing the axial release of the pressurized oil as far as possible from the outlet chamber, it is possible to mitigate the effects on the inlet chamber. The main reason of the potential beneficial effects relies on the fact that the backlash opening generates contained radial flows that contribute to reduce the pocket pressure. Within this framework, the proposed grooves present a bridge shifted to the suction side of the 70% and 60% of the standard bridge width, respectively. In addition, to ensure the oil axial relief avoiding full enclosure, four groove extensions have been added on the bridge corners. For sake of clarity, hereinafter the groove shifted of the 70% will be named as *Mod 1* while the 60% shifted will be named as *Mod 2*. Moreover, with the purpose to better respond to the injection of pressurized oil, the suction chamber volume has been increased extending

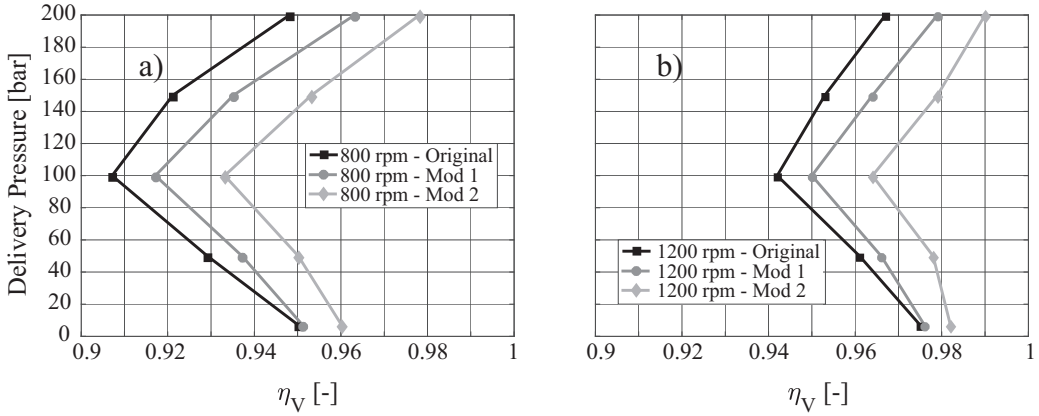

Figure 48: Comparison between volumetric efficiency of different groove design calculated at 800rpm (a) and 1200rpm (b)

the inlet groove. The described designs are presented within Figure 46 while Figure 47 depicts the gear vain enumeration for the case study pump.

The model has been launched reproducing the operative conditions implemented for the original balancing plate. As can be seen from Figure 48 is clear that the novel balancing plates are responsible of a consistent pump performance increment. Considering the volumetric efficiency with respect to delivery flowrate measured at 7 bar, the *Mod 1* configuration shows a mean increment of the 1% through the entire set of simulations. In particular, it shows a crescent improvement incrementing the target delivery pressure. On the other hand, the *Mod 2* configuration shows a similar increment trend with a 2.5% of efficiency increment with respect to the original configuration. As shown, the gap recover at high delivery pressure still ensure the efficiency increment.

Despite the volumetric efficiency confrontation do not leaves doubt on the effective improvement introduced, it is worth to deepen the investigation of the pump behaviour comparing as more results as possible. The graphs presented in Figure 49 play a key role for the choice of the most effective solution. As well as for the volumetric efficiencies of Fig. 48(a) and (b), the figures on the left are referred to the 800 rpm test condition while on the right side there are the 1200 rpm results. Figures 49(a) and (b) represent the delivery pressure achieved by the pump with reference to the target delivery pressure reported in the graphs abscissa. Compared to the original balancing plate, the new

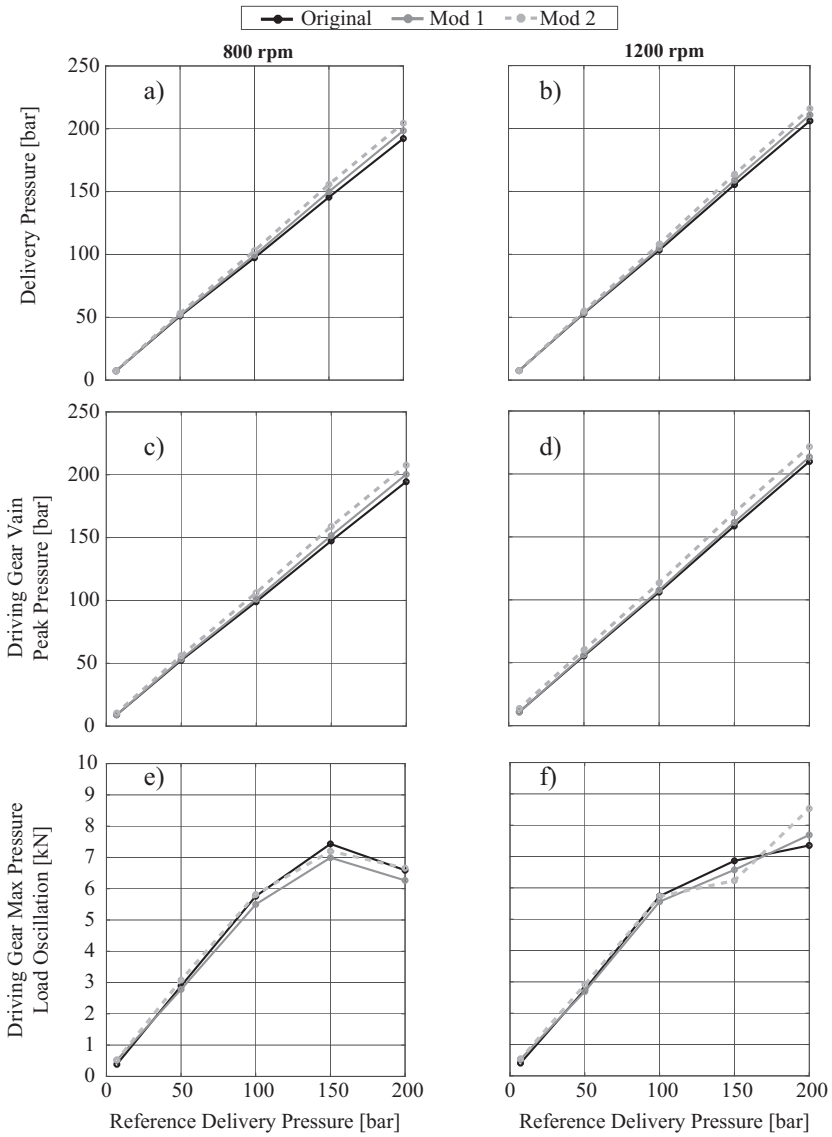

Figure 49: Comparison between the results of simulation of different groove design, calculted for the driving gear: delivery pressure at 800rpm (a) and 1200rpm (b), pressure peak at 800rpm (c) and 1200rpm (d), maximum pressure load oscillation at 800rpm (e) and 1200rpm (f)

grooves ensure a higher pressurization, even if the pressure gain seems to be relatively contained. With same principle, the pressure peak calculated among

the gear vain suffers a slight increment for the *Mod 2* plate remaining on similar magnitude of the original configuration. The subfigures (c) and (d) are referred to the driving gear vain, same trends have been observed on the driven gear vain and have been omitted for sake of brevity. Since the gear pressure loading indisputably follows the peak pressure trend, the graphs with the comparison of the mean pressure load value trend have been omitted, On the contrary, within subfigures (e) and (f) the maximum amplitude of the observed numerical pressure load oscillation have been reported. The importance of such parameter stands in the facts that load oscillation would represents an indicator of potential dynamic effects on the pump. The behaviour of the three implemented layouts is similar at 800 and 1200 rpm showing a slight reduction of the load amplitude. As an exception, the 200 bar-1200 rpm condition presents for *Mod 1* and, more consistently, for *Mod 2* configuration a sensible amplitude increment. Despite it represents a potential negative effect on the pump, the consistency of the efficiency improvement suggests to take in consideration the *Mod 2* as definitive improvement solution.

Considering the pump performance maps reported within Figures 43 and 48, is clear that the pump suffer a considerable efficiency loss when the delivery pressure is set to achieve 80-120 bar. Within this context, the analysis of the simulation results, carried out by means of the post-processing module, has given the chance to further improve the pump behaviour. In particular, since the efficiency loss is clearly connected to flowrate losses and the phenomena is delivery pressure dependent, the investigation has been performed setting a reference pump speed at 1200 rpm, varying the target outlet pressure. Furthermore, the attention has been focused on the comparison of the entire set of flowrates contributes between the control volumes. Figure 50 includes the comparison between the flowrates exchanged by the driving gear vain control volume through the backlash gap. Subfigures from (a) to (f) are representative of the *pre* and *post* flowrates. From the pictures, descends that increasing the pump pressurization, the *pre* flowrates conserve the magnitude while the *post* values linearly increase in the negative part. Following the model vain enumeration described in Fig. 47 and considering the flowrates sign framework, is clear that outgoing flowrates are exchanged from the pressurized vain to the driven gear mating vain after the bridge zone. Figures (g), (h) and (i) represent the lateral leakages exchanged by adjacent gear vain along the axial gaps. Even for such flowrates the pressurization of the pump do not shows sensible

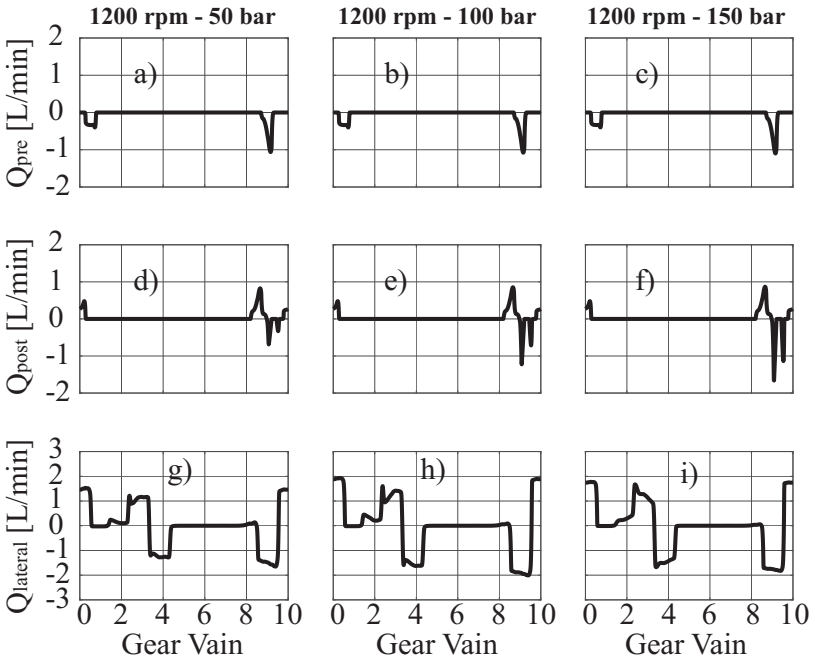

Figure 50: Flowrate exchanged by driving gear vain during a pump rotation at different target delivery pressure. Flowrate exchanged through the backlash gap before the meshing zone (a), (b), (c) and after the meshing zone (d), (e), (f). Vain to vain flowrates exchanged through the frontal gap (g), (h) and (i)

effects. On the other hand, the analysis of tip flowrates shows a non-linear trend. The expected behaviour of such leakages should present the reduction of the outgoing flowrates within the initial zone of the pressure arc, thanks to the progressive tip clearance closure. However, as depicted within Figure 51, the magnitude of the flows exchanged in the early pressurization zone suffer a sensible increment when the target delivery pressure is set to 100 bar for both driving (b) and driven gear (e). The result given by the graphical analysis suggests that such phenomena, particularly visible for the driving gear control volumes, needs to be further analysed. Within this context, the analysis of the radial gap between gear tip and pump body internal housing assumes a relevant importance. Since the gear vain control volumes may exchange flowrates through the tip gaps, it is fundamental to understand the magnitude and the trend of such clearances. Within Fig.52 the trends of the tip gap which put in communication with the previous vain are reported.

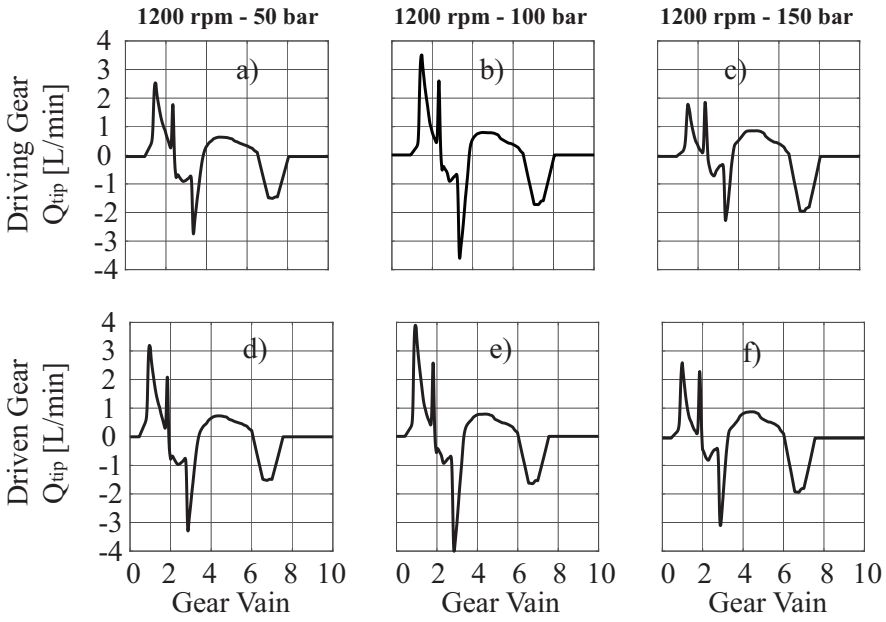

Figure 51: Flowrates exchanged through the tip gap by the driving gear vain at crescent delivery pressures (a), (b), (c) and flowrates exchanged through the tip gap by the driven gear vain (d), (e), (f)

The reason stands into the necessity to focus the attention on the exchange orifice between pressurized gear vain and the suction chamber. According to the pump scheme of Fig. 47, when CV 3 of the driving gear approaches the pressure arc zone, it starts the pressurization. As a matter of fact, in this condition the oil starts to squeeze through the radial exchange surface toward the less pressurized inlet chamber. The leakage then continues even when both the vain flanks are completely entered within the pressure arc zone. In this context, the right tip orifice is usually crossed by a positive flowrate, coming from the more pressurized following vain. On the other hand, the left tip is crossed by a negative flowrate toward inlet chamber. The balance of the tip flowrates produces the drop shown within Fig. 51. The graphs in Fig.52 allow to understand that the oil pressurization among the vain take place when the gap tends to, or equalize, the zero value along the pressure arc, within the suction side of the pump. However, the zoomed view presented in Fig.52(c) highlight the lack of contact between gear and housing for the driving gear at 100 bar, while for the driven gear (d) the gear is capable to neglect the

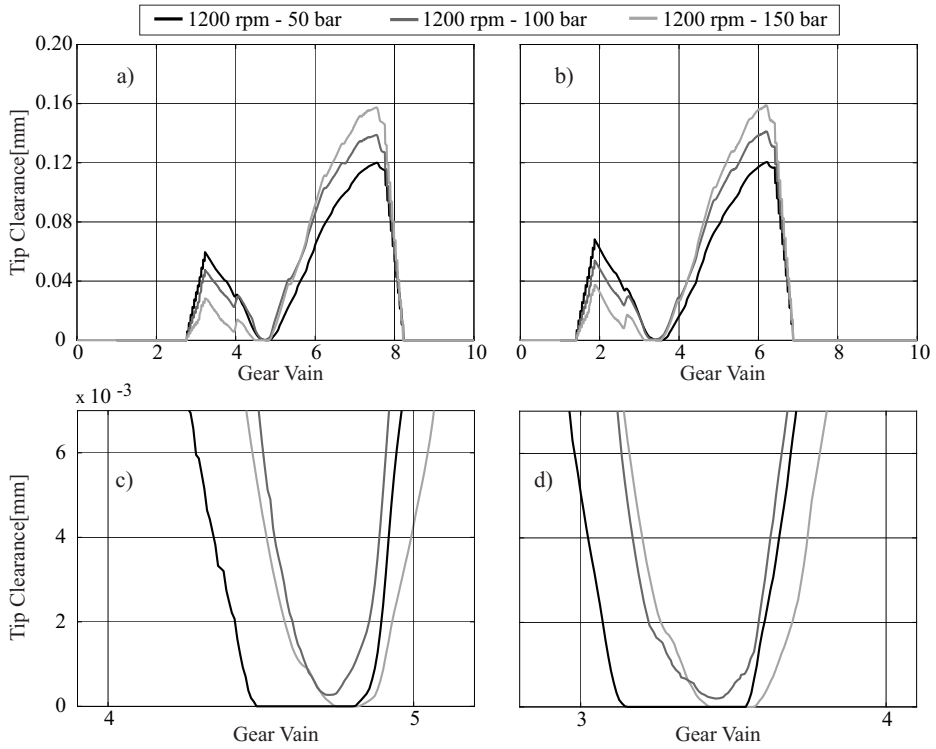

Figure 52: Comparison between the tip clearance profile traced during a pump revolution at different delivery pressure condition for the driving gear (a), driven gear (b) and the respectively zoomed views (c) and (d)

radial gap avoiding undesired leakages. The remaining gap on the driving gear provokes an high outgoing flowrate from vain 4 to vain 3, as shown in 51(b). It also might be recognized as the responsible of the efficiency drop in such simulated condition.

Despite the novel balancing plate proposal has shown a consistent potential improvement on the pump efficiency, the discover of such detachment phenomena suggests that with slight additional improvements the machine may achieve further enhancements. Within this context, the strategy adopted relies on the anticipation of the pressure arc on the pump suction side giving the chance to ensure the gap closure even at 100 bar. The design upgrade basically consists into the modification of the pump housing through the extension of the circular housing profile, keeping unaltered the housing diameters and center distance. In parallel, it is worth underline that even the balancing plate

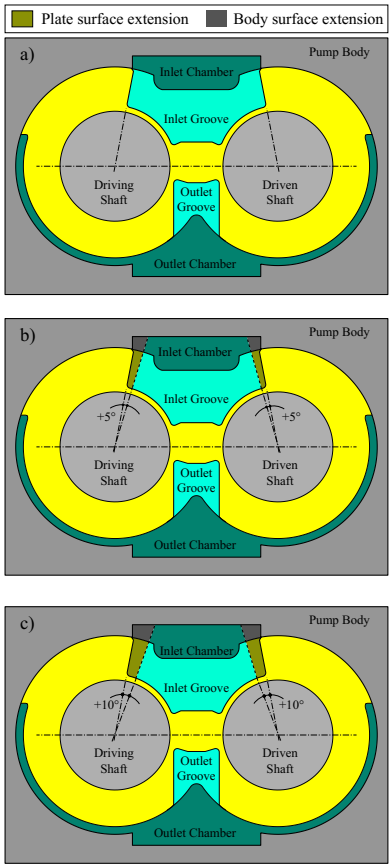

Figure 53: Schematic view of the novel balancing plate equipped within the pump body in original layout (a), 5° inlet chamber modification (b) and 10° inlet chamber modification (c)

grooves needs to be updated reducing the suction groove. Since the simulation results have not shown particular criticality on the delivery side, pump body and balancing plate have not been updated. Here, original and updated pump bodies are presented in Fig. 53. Figure 53(a) shows the original pump layout and the proposed novel balancing plate in yellow. Then, as shown within Fig. 53(b) and (c), the anticipation of the pressure arc produces the concurrent reduction of inlet groove and inlet chamber on both driving and driven side. With the purpose to evaluate the impact of the modification, the update has been carried out implementing two steps of arc anticipation shifting the groove boundaries of 5° and 10°. The limit was set by the pump manufacturer since

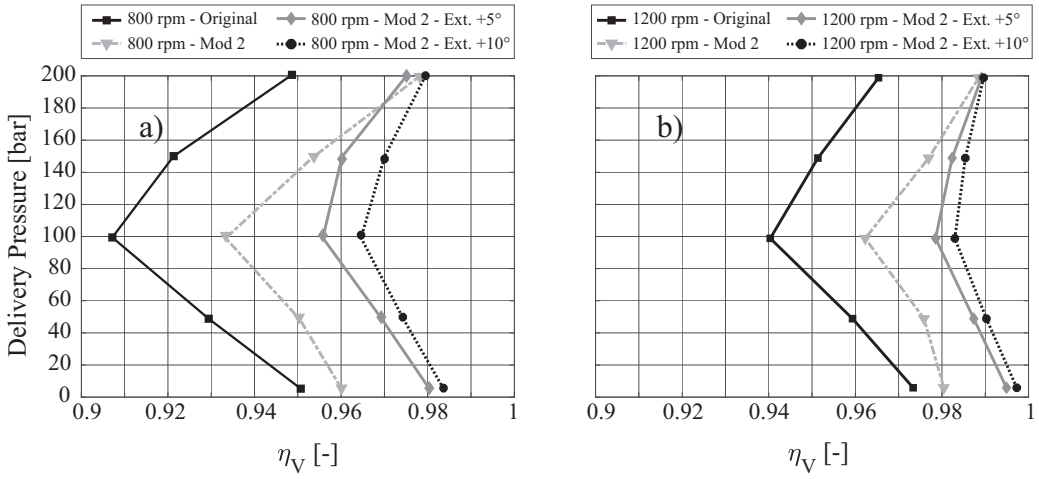

Figure 54: Comparison between volumetric efficiency of the pump with original layout, with novel balancing plate and original housing and with pressure arc extension calculated at 800rpm (a) and 1200rpm (b)

further inlet chamber closures would have not met the body constraints given by the inlet piping.

The designed updates have been implemented within the model and simulated with the purpose to obtain the new configuration performance mapping. The maps are included in Fig. 54. As well as for the first update step, the 800 and 1200 rpm conditions have been considered for the comparison. It is worth underline that only the *Mod 2* balancing plate layout has been considered for the pressure arc extension update. The results suggest that the proposed update may introduce a strong efficiency gain in all the configurations but seems to intensify the effect on the 100 bar zone as expected. The comparison between 5° and 10° extension shows a major impact at lower speed (54(a)) where a mean 1% of efficiency increment has been calculated for the entire set of simulations. On the other hand, at 1200 rpm (54(b)) the improvement ensures a mean 0.4% efficiency increment. It is worth underlining that at the higher tested speed the calculated efficiency already achieve values near to the 99% in all the tested conditions. Furthermore, the pressure arc extension do not introduce appreciable improvement for the 200 bar target delivery pressure condition where the three layouts present almost coincident efficiency values.

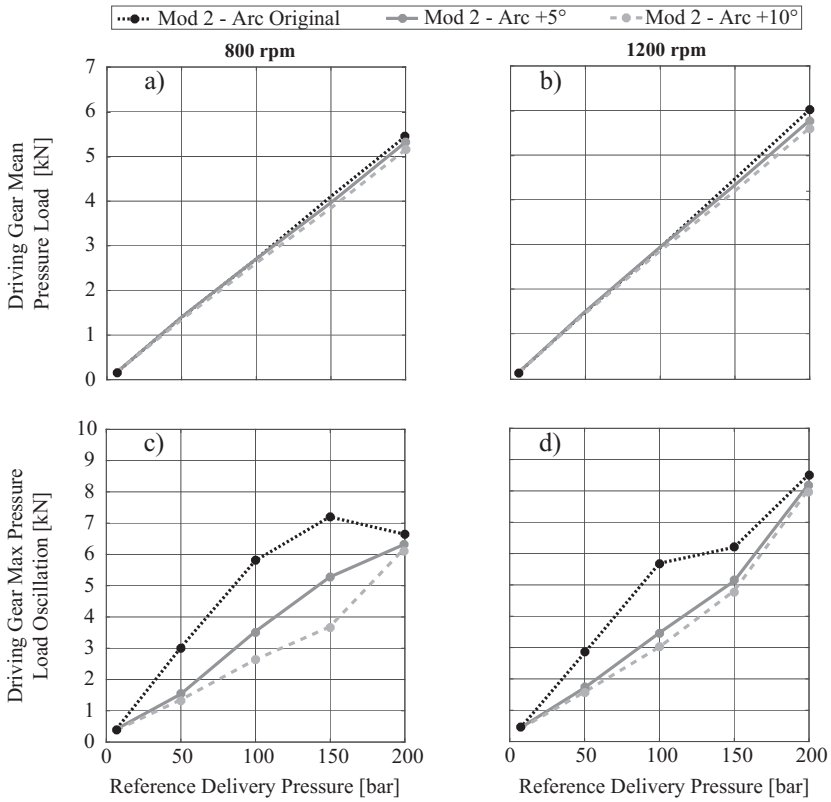

Figure 55: Comparison between the results of simulations with updated balancing plate and different pressure arc layouts, calculted for the driving gear: , mean value of the pressure load at 800rpm (a) and 1200rpm (b) and maximum pressure load oscillation at 800rpm (c) and 1200rpm (d)

Following the formerly proposed comparison framework, Fig. 56 has been included to give a straightforward but general overview of the pump behaviour variations. From figures 55(a) and (b) it is possible to see that the mean value of pressure load calculated for the driving gear at crescent target delivery pressure, do not shows sensible variation between the three tested configurations. A slight reduction is shown for the *+10°* layout at both pump speed but it not represents a remarkable improvement. On the contrary, figures 55(c) and (d) gives the chance to appreciate the beneficial effect of the pressure arc extensions even on the loading context. In fact, with the updated housing the amplitude of the pressure force ripple, calculated on the driving gear, undergoes an extremely important containment within the three middle delivery pressure

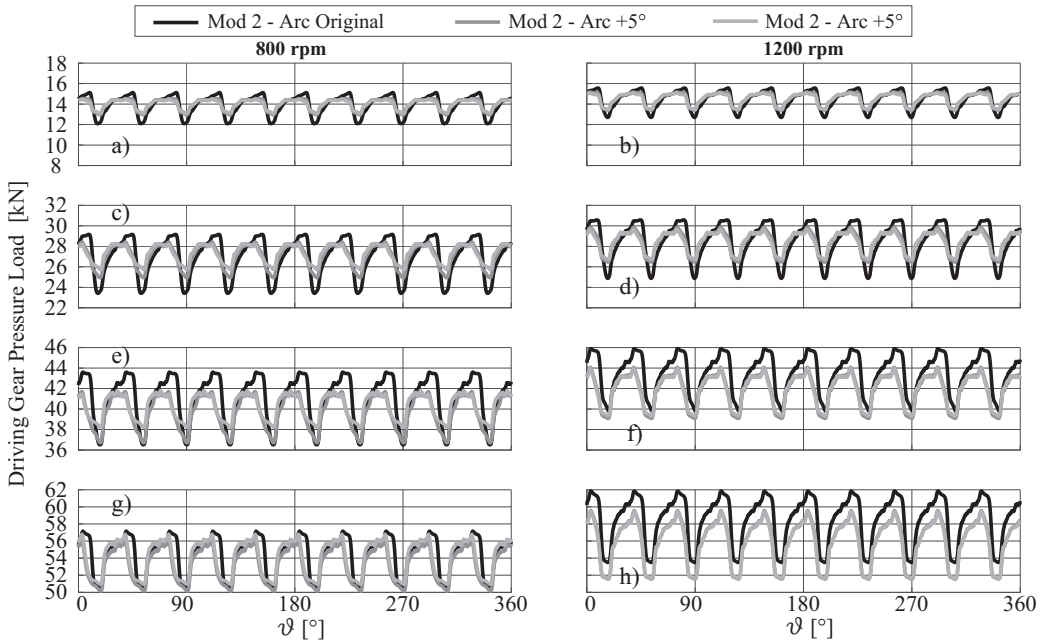

Figure 56: Comparison between the pressure load ripples calculated for the pump with updated balancing plate and different pressure arc layouts. Simulations carried out at 800 and 1200rpm respectively, at different target delivery pressure: 50 bar (a) and (b), 100 bar (c) and (d), 150 bar (e) and (f), 200 bar (g) and (h)

conditions. At 800 rpm the effect of the 10° extension assume a major relevance suggesting a 50% reduction of the load ripple at 50, 100 and 150 bar of reference delivery pressure. Then, increasing pump speed the +5° layout ensures the same effects of the *+10°* keeping the 50% curtailment at 50 and 100 bar, reducing it of the 15% at 150 bar. Moreover, the 200 bar condition has not been improved comparing novel housing layout to the original one. Within this context, the graphs presented within Fig. 56 give the chance to understand both the waveform of the pressure load ripples and the effects of the design improvement on them. It is immediately appreciable the amplitude reduction from the original ripple for the entire set of simulations. In parallel, it is possible to identify the mean load value reduction for the higher delivery pressures Fig. 56(e), (f), (g) and (h). Aside from the amplitude containment of the ripple, it is fundamental to attenuate the drastic increment and reduction of

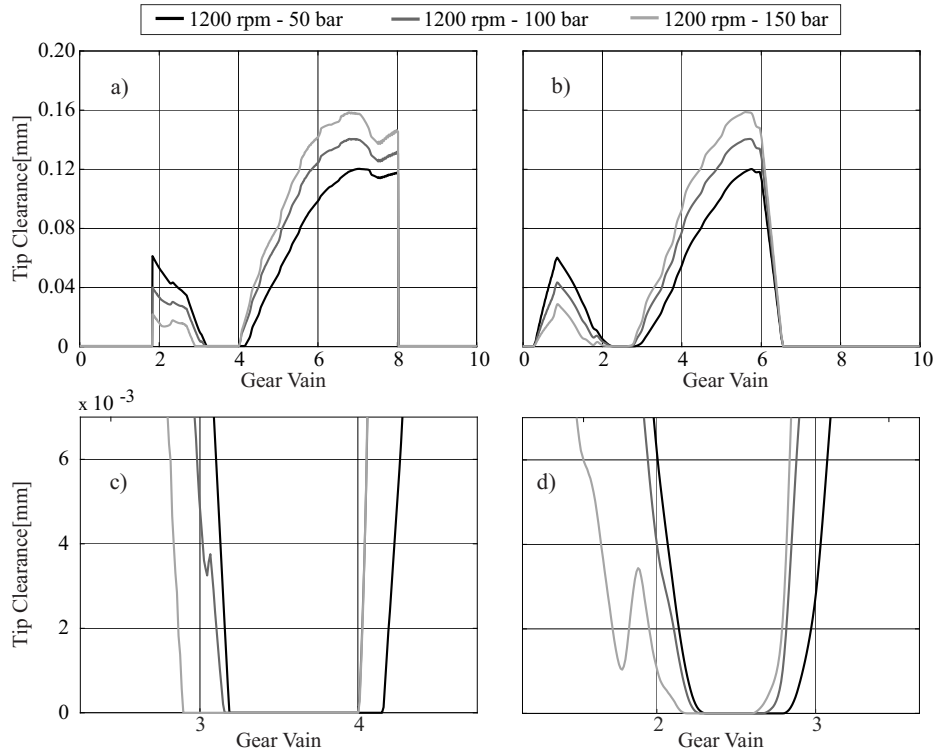

Figure 57: Comparison between the tip clearance profile traced during a pump revolution for a pump equipped with the updated balancing plate and pressure arc extension of 10°, at different delivery pressure condition for the driving gear (a), driven gear (b) and the respectively zoomed views (c) and (d)

the wave. The *+10°* modification seems to achieve the goal more effectively than the +5° layout. In particular, since the improvement with respect to the original layout is eloquent, between the two configuration the major discrepancies are recognisable at 800 rpm as shown within Figures 56(c), (e) and (g). It is worth underlining that the presented estimations are just indicators of the pump dynamic behaviour since at the current state of the research it is not possible experimentally acquire pressure force ripple and compare with the numerical values. Furthermore, such strong and evident result obtained from the numerical study, suggests that the design updates would be capable, *in primis*, to improve the pump efficiency and also to strongly contain the dynamic effects related to the pressure ripples.

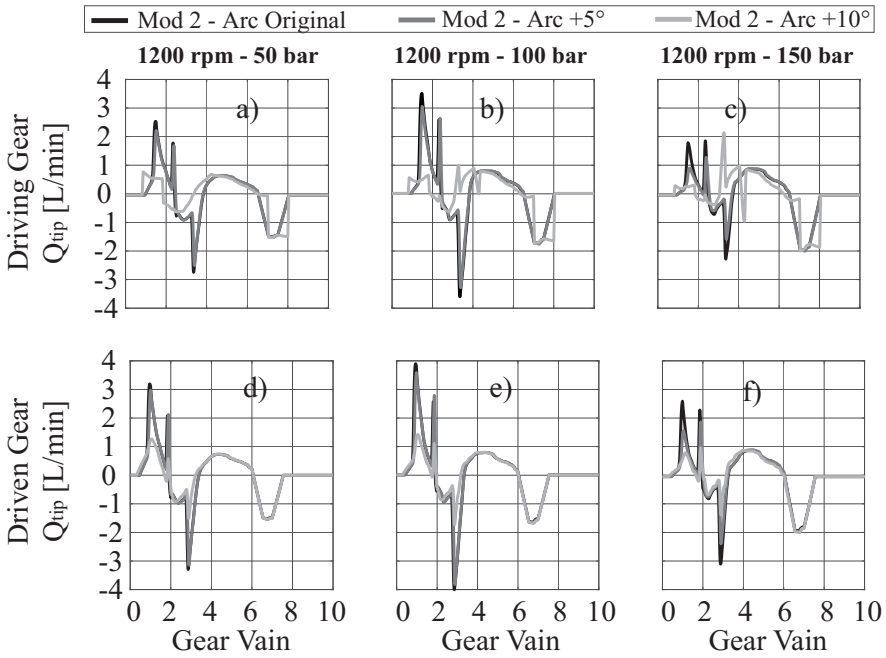

Figure 58: Comparison between different pump layout of the flowrates exchanged by the gear vain through the tip clearances at 1200 rpm. Driving gear results at 50 bar (a), 100 bar (b), 150 bar (c) and driven gear results at 50 bar (d), 100 bar (e) and 150 bar (f)

Finally, the analysis of the simulation results has been focused on the tip clearances calculated through the entire pump revolution presented within Fig. 57. The zoomed views of Fig. 57(c) and (d) show that the proposed arc extension ensures the clearance sealing for the entire set of simulated condition, resolving the detachment observed at 100 bar in the original layout of the housing. Furthermore, the sealing take place for a wider portion of the pressure arc giving the chance to the pump to quickly and highly pressurize the trapped oil, increasing the efficiency. Within Fig. 58 is shown the comparison between the tip flowrates exchanged by the gear vain at 1200 rpm at different target delivery pressure. The 5° inlet chamber restriction shows a leakage trend close to the original version even if contributes into the leakages reduction. On the other hand, the leakage containment is strongly notable for the *+10°* configuration in all the simulated conditions.

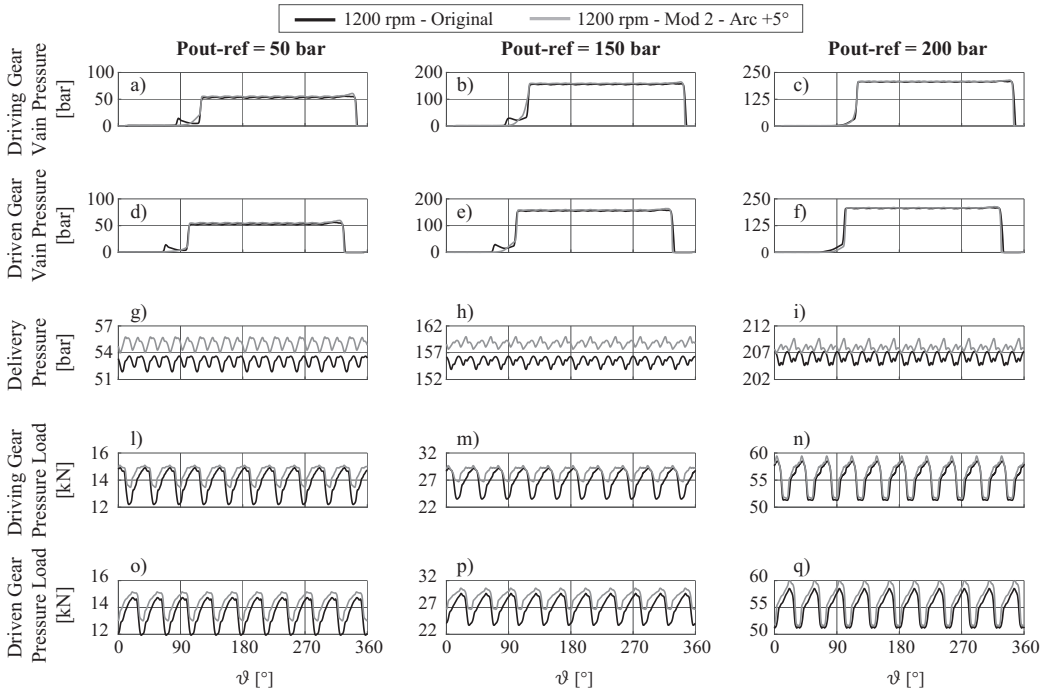

Figure 59: Comparison between the simulation results of the original pump layout and the updated version. Pressure values calculated on the vain control volumes for the driving gear at 50 bar (a), 150 bar (b), 200 bar (c) and driven gear results at 50 bar (d), 100 bar (e) and 150 bar (f). Delivery pressure ripple at 50 bar (g), 100 bar (h) and 150 bar (i). Pressure load ripples calculated on the driving gear at 50 bar (l), 150 bar (m), 200 bar (n) and on the driven gear at 50 bar (o), 100 bar (p) and 150 bar (q).

The analysis of the numerical results gives the chance to assume, with reasonable confidence, that the equipment of the *Mod 2* balancing plates and the parallel inlet chamber and plate groove restriction of 10°, are capable to lead the pump to reach a higher volumetric efficiency and a more satisfactory NVH behaviour. A final and comprehensive overview of the improvement achieved by the proposed novel layout are presented in Fig.59. In particular, the sub-figures from (a) to (f) present the pressurization scheme of the driving and driven gear vain. The numerical results highlight a smoother pressurization of the vain control volume on both gears, avoiding the pre-compressive spike shown until 150 bar of target pressure, which may introduce undesired dynamic effects. Despite the new groove layout ensures a higher mean delivery

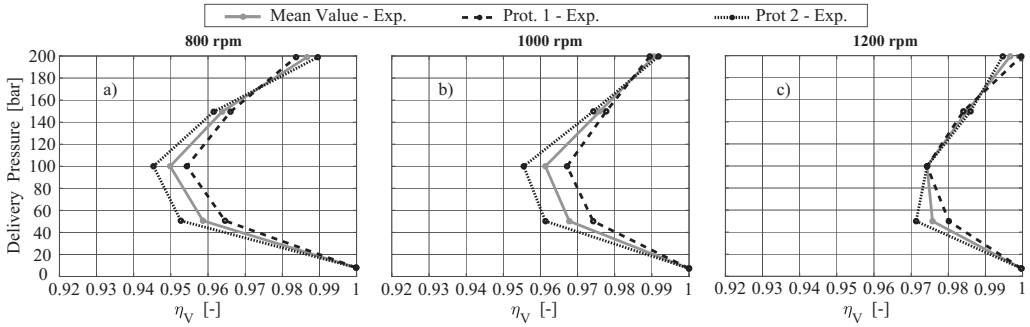

Figure 60: Volumetric efficiency maps of the two novel layout prototypes obtained at 800 rpm (a), 1000 rpm (b) and 1200 rpm (c)

pressure value in all the tested conditions, as shown within Figures 59(g), (h) and (i), vain pressure peaks within the meshing zone among 315 and 340° are not recognisable. Then, for what concerns the loads characterization, the sub-figures from (l) to (q) further highlight the beneficial effect of the design improvement on the load ripple amplitude containment until 150 bar of reference delivery pressure. On the contrary, the 200 bar condition depicted in 59(n) and (q) is subjected to a slight increment of the ripple which represents a minor effect if compared to the whole set of simulated conditions.

3.6.3 *Experimental Evaluation of the Proposed Design Improvement Solutions*

Since the numerical results have shown strong potential benefits from the suggested design improvement solutions, two sample pumps have been produced following the proposed design guideline and tested in a dedicated experimental campaign. Such pumps have been subjected to a running in procedure with the purpose to obtain the operative internal clearances. Then, in order to evaluate the coherency of the numerical data, the pumps have been tested at three stationary pump speed and five different target delivery pressure. The comparison with the numerical study has been carried out through the analysis of the pump efficiency. In particular, Figure 60 shows the efficiency maps obtained at three different pump speeds for the new pumps. As well as for the first mapping, the outlet flowrate measured at the lower target pressure have been assumed as the reference data for the volumetric efficiency calculation.

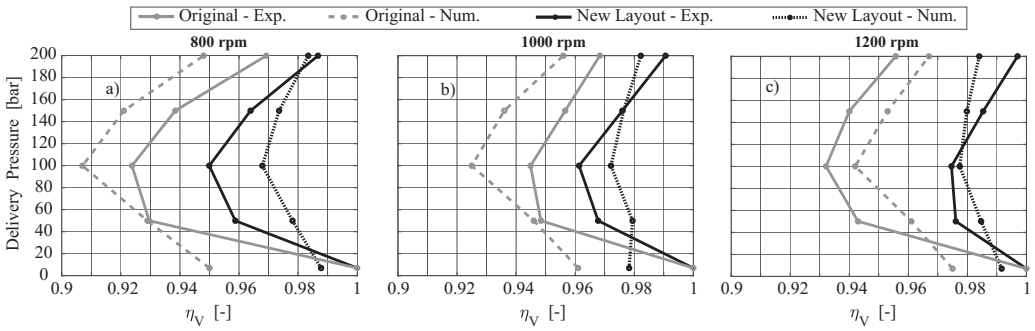

Figure 61: Experimental and numerical volumetric efficiency comparison between original and updated pump layout obtained at 800 rpm (a), 1000 rpm (b) and 1200 rpm (c)

The two tested prototypes have shown an overall good reproducibility of the results.

With the purpose to evaluate the efficacy of the design improvement, a mean efficiency value has been considered as representative for the novel layout. The comparison with the original pump layout is shown in Fig. 61 where the experimental results have been plotted with a continuous line while the numerical results are depicted with dashed lines. In first hence, it is worth to highlight the coherence of the numerical results if compared to the novel pump experimental results. The slight discrepancy between the curves allows to assume that the model is capable to reproduce and predict experimental results with good accuracy and reliability. Then, focusing the attention on the continuous lines, it is possible to appreciate the strong volumetric efficiency improvement, expected from the numerical results. The experimental maps highlight the reliability of the design improvement strategy and the robustness of the LP model proposed within this work. While the 1000 rpm tests shown in Fig. 61(b) a mean 1.5% of volumetric efficiency improvement for the entire set of tested conditions, the 1200 rpm maps in Fig. 61(c) shows a heavy improvement of the efficiency. If at 50 bar of target delivery pressure the pump shows a 3% of increment, at higher delivery pressures the improvement stands at 4At lower speed the efficiency increment stands at 2.5% almost equal for the entire set of tested conditions. As highlighted from the simulations, for the novel pump layout the increment of the delivery pressure generates the typical curve shown by the original pump. Focusing on the maps area around the 100 bar

condition, the housing modifications included to mitigate the efficiency loss phenomena, have shown relevant effect in such direction from the numerical data. Despite numerical results overestimate the benefits of the modifications in this context, the experimental data clearly confirm the beneficial effect of the improvement. Moreover, increasing the pump speed the novel pump curves progressively reduces the difference between the 100 bar efficiency and the values at higher outlet pressure, confirming the efficacy of the proposed design solutions.

3.7 ANALYTICAL DESIGN PROCEDURE FOR EXTERNAL GEAR PUMPS

As mentioned within previous sections, aside from a reliable implementation and resolution of the continuity equations, the results obtained through the LP model also relies on the accuracy of the preprocessing tool which calculates exchange areas and control volumes dimensions. However, without a robust calculation and reproduction of the gears equipped within the pumps, the entire preprocessing environment would not exists. Furthermore, when it is necessary to design *ex novo* a gear pump in addition to the reproduction of the gearing, it is fundamental to have a design tool that allows to evaluate clearances, estimates loads and guide the calcualtion of the bearings. The design of a gearpair responsible of a proper pumping action is an operation that requires a completely different approach with respect to the more common power transmission gearpair designs. With the purpose to generates the required pump displacement and clearances for proper working conditions, the introduction of non-standard module, tooth undercut, profile shift is a strategy often implemented in such field. Furthermore, the design of the clearances between the gears and the statoric components of the pump , *e.g.* casing, side plates, journal bearings, requires a dedicated study for balancing mechanical and volumetric losses. Since the design of a novel gear pump involves the calibration of a great variety of parameters which have combined effects, the presented methodology would give a reliable and comprehensive tool for the scope.

In the current Section the analytical formulae, which constitute the structure of the presented design methodology, are exposed and described. The design strategy implemented in this work has been structured in three iterative calculation phases, described in the following Subsections. Figure 62 illustrates

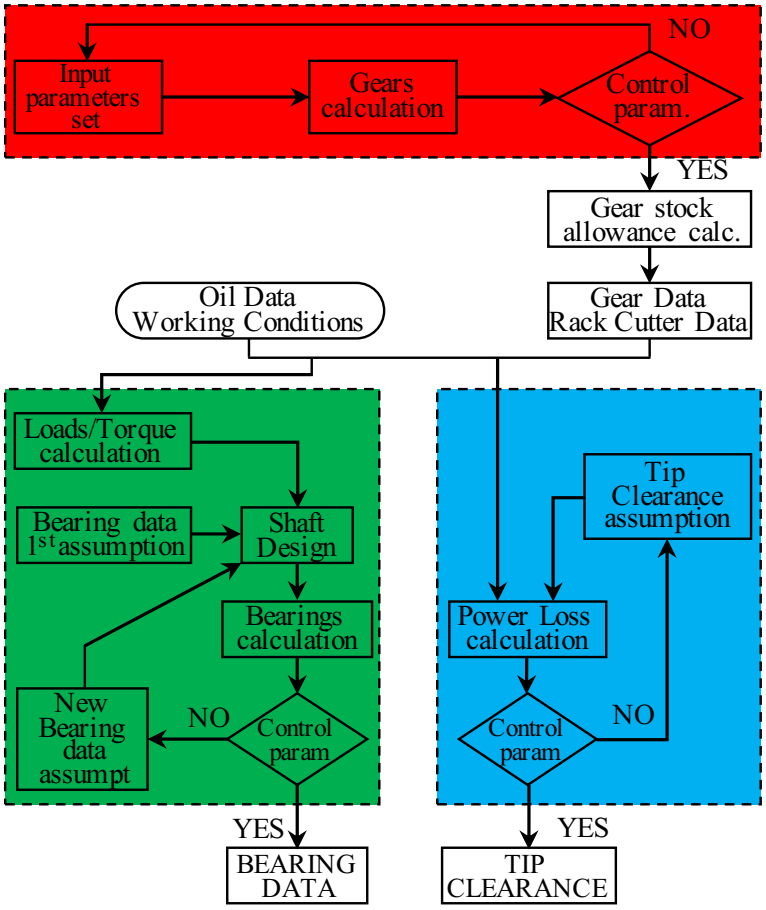

Figure 62: Design Procedure Workflow

the workflow of the procedure and the iteration scheme of each calculation phase. The first Subsection, focuses the attention on the calculation of a proper tooth profile that meets the space requirements limitation while ensuring the expected displacement. The gear design phase ends with the pre-grinding profile calculation which leads to calculate the real rack cutter data. Consequently, the second Subsection presents the calculation of torque and loads acting on the driving shaft, its structural design and the design methodology for the journal bearings. Finally, the third Subsection is dedicated to the description of the design methodology for the casing radial gap.

3.7.1 *Geometrical Design of Gears*

The first calculation step of the geometrical design phase, leads to obtain a draft gearpair. By means of geometrical input parameters m_n, z, α, x, ad_T, h_T, the geometry of the rack cutter tool is defined and, thereafter, the first output parameters set is generated. Equations from 55 to 59, form the first group of analytical equations of the first calculation step.

$$I = D_{pitch} = m_n \cdot z \tag{55}$$

$$D_{base} = D_{pitch} \cdot \cos \alpha \tag{56}$$

$$D_{root} = D_{pitch} - 2 \cdot (ad_T - x) \tag{57}$$

$$s_{pitch} = \frac{\pi m_n}{2} + 2 \cdot x \cdot \tan \alpha \tag{58}$$

$$D_{tip,lim} = D_{pitch} + (h_T - ad_T) + x \tag{59}$$

Limit tip diameter, calculated on Eqn. 59, represents the upper limit for the tip diameter of the gears. The choice of a proper value introduces the second calculation step, where the input parameters I_{op}, D_{tip}, W allow to complete the calculation of the draft gearpair. By defining the operative pressure angle α_{op}:

$$\alpha_{op} = \cos^{-1}\left(\frac{I \cos \alpha}{I_{op}}\right) \tag{60}$$

operative pitch diameter $D_{pitch,op}$ is achieved:

$$D_{pitch,op} = \left(\frac{\cos \alpha}{\cos \alpha_{op}}\right) D_{pitch} \tag{61}$$

thus, tooth thickness at operative pitch diameter $s_{pitch,op}$ is calculated:

$$s_{pitch,op} = \left(\frac{s_{pitch}}{D_{pitch}} + inv\,(\alpha) - inv\,(\alpha_{op}) \right) D_{pitch,op} \tag{62}$$

and tip pressure angle α_{tip} is calculated as:

$$\alpha_{tip} = \cos^{-1} \left(\frac{D_{tip} \cos \alpha}{D_{pitch}} \right) \tag{63}$$

moreover, clearance at root diameter δ_r is defined as:

$$\delta_r = I_{op} - \frac{1}{2} \left(D_r + D_{tip} \right) \tag{64}$$

In order to achieve the target performances, the values of some calculated output parameters have to stick to fixed limit values. These parameters act the role of control parameters and lead to orient the choice of the input parameters. Throughout the current phase, control parameters are calculated in addition to the output parameters already presented.

Pump displacement Cc_{lim} is a control parameter set out according to the target delivery flow rate. Its value is calculated as:

$$Cc_{lim} = \frac{Cc}{\eta_v} \tag{65}$$

where Cc is the target displacement provided as constraint data in the early phase of the design and η_v is the assumed volumetric efficiency of the pump.

The formulation exposed in the following equation relies on Ref. [58] and allows to calculate the design displacement for the input parameters set:

$$Cc_{des} = 2\pi W \left[\left(\frac{D_{tip}}{2} \right)^2 - \left(\frac{D_{pitch,op}}{2} \right)^2 \cdot \left(1 + \frac{1}{3} \cdot \left(\frac{\pi \cos \alpha_{op}}{z} \right)^2 \right) \right] \tag{66}$$

thus, the admissible error on the control parameter Cc_{lim}, have to be assumed for the assessment of calculated displacement Cc_{des}.

Total width limit w_{lim} is a control parameter imposed in order to limit the space requirement of the gearing. Equation 67 shows the analytical formula for total width calculation and the comparison related to the limit value as well:

$$w = I_{op} + D_{tip} \quad (< w_{lim}) \tag{67}$$

furthermore, thickness of the teeth (s_{tip}) is calculated as:

$$s_{tip} = \left(\frac{s_{pitch}}{D_{pitch}} + inv\,(\alpha) - inv\,(\alpha_{tip}) \right) D_{tip} \quad (> s_{tip,lim}) \tag{68}$$

where $s_{tip,lim}$ is assumed to guarantee the gear manufacturability.

Backlash b calculation is provided by:

$$b = \left(\frac{\pi D_{pitch,op}}{z} - 2s_{pitch,op} \right) \frac{D_{pitch}\ \cos\alpha}{D_{pitch,op}} \quad (> b_{lim}) \tag{69}$$

where backlash limit values b_{lim} is assumed from good practices.

It is worth noting that undercutting is often present in these designs and therefore the contact ratio needs to be estimated from the form diameter of the gear, since standard formulas may not be applied. Once the form diameter is defined, the length of active segment $\overline{K_1K_2}$ on the line of contact is obtained. In the end, the contact ratio is calculated by:

$$cr = \overline{K_1K_2} \cdot \frac{z}{\pi D_{base}} \quad (> cr_{lim}) \tag{70}$$

where contact ratio limit cr_{lim} is set out in order to ensure continuous meshing.

Finally, the relief groove width on the path of contact g_{op} is provided by:

$$g_{op} = \zeta \cdot \overline{K_1K_2} \cdot \cos\alpha_{op} \tag{71}$$

where ζ is a tuning parameter within 0 and 1 and represent the bridge contact covering ratio. Figure 63 illustrates the path of contact and the bridge width. The purpose of the ζ parameter is to provide an entry point for further relief groove enhancements. In particular, it allows the estimate the bridge width compared to the gear geometry and dimensions. As mentioned in [68], an accurate evaluation of the relief groove dimension plays a key role on the proper functioning of the pump. Values of ζ close to 1 means large bridge width, hence, high pressure peaks. On the contrary, thinner relief groove implies smoother pressure transitions even though a reduction in terms of volumetric efficiency may occur. The third calculation phase consists in the improvement of the draft gearpair which is achieved by calibrating the input parameters. From the first draft design, even with slight parameters variations, the gearpair characteristics may be enhanced. For gear pump application, the necessity to

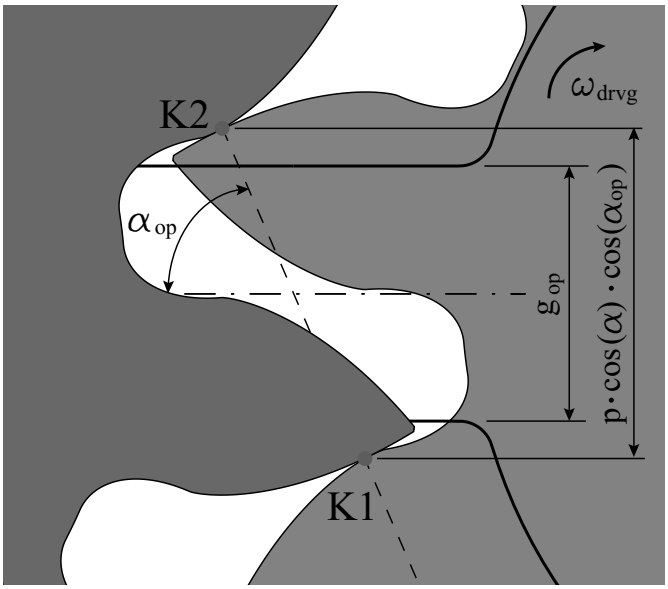

Figure 63: Path of contact and relief groove

design non-standard gears in order to achieve target performances, allows to assume values of the module substantially different from the standard ones. As well as the other input parameters described, the module may be calibrated in order to achieve the improvement of the gearing. Its variation affects most of the input parameters therefore it should be the first tuned parameter in the improvement design phase. Later, other geometrical parameters may be further modified, such as operative center distance I_{op} that directly reflects on the calibration of pump displacement. In alternative, regulation of the facewidth W provides equivalent results.

As a concluding step of the gearpair design procedure, it is worth underlining that gears employed in volumetric machines often undergo a tooth flank grinding process with the purpose to improve surface quality and smoothness of gearing. For this reason, gear stock allowance is usually provided to the teeth flanks. The rack cutter designed in the former calculation phases has been adopted in order to achieve the final shape of the gear, without taking into account eventual grinding operations. With the purpose to consider manufacturability aspects, the design of the pre-grinding rack cutter has been integrated into the procedure. From the choice of a certain gear stock allowance

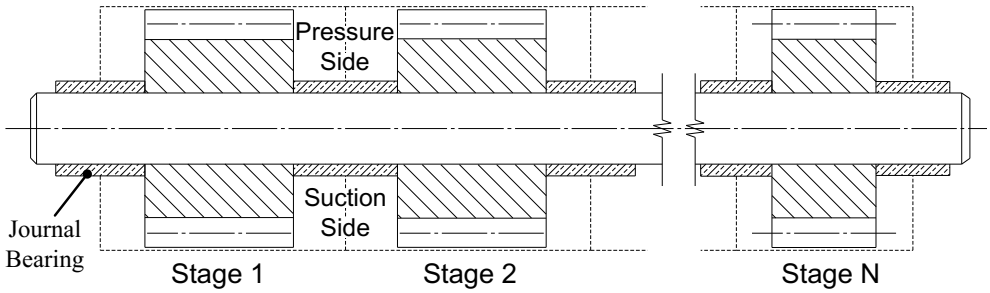

Figure 64: N stages gear pump schematic layout

γ, the pre-grinding tooth thickness at pitch circle s'_{pitch} is calculated by Eqn. 72:

$$s'_{pitch} = s_{pitch} + \gamma \tag{72}$$

By adapting Eqn. 58, the updated profile shift x' is calculated by Eqn. 73:

$$x' = \left(s'_{pitch} - \frac{\pi m_n}{2}\right) \cdot \frac{1}{2 \tan \alpha} \tag{73}$$

and the new rack cutter addendum $ad_T{}'$ is obtained:

$$ad'_T = \frac{D_{pitch} - D_{root}}{2} + x' \tag{74}$$

3.7.2 *Shaft and Bearings Design*

From the fulfilment of the gearpair design, it is now possible to give an analytical estimation of the pressure force and torque that loads the gears and the shaft. It constitutes the first step for the shaft calculation and for the journal bearings design. It is worth underline that, with the purpose to give a general dissertation, the design procedure has been formalized for a multistage gear pump with N stages. A scheme of an N stages pump is shown within Fig. 64. The estimation of the distributed pressure loads on a single stage has been integrated according to the simplified formula presented in [21]:

$$f_i = \frac{3}{4} \cdot \Delta P_i \cdot D_{tip,i} \tag{75}$$

thus, total pressure torque is calculated as the sum of the pressure torque of the N stages. Within the frameworks of the current methodology, friction effects have been neglected from the calculations and each i-th stage pressure torque is calculated with reference to the formulation proposed in [21]:

$$T = \sum_{i=1}^{N} \left(\Delta P_i \cdot (D_{tip,i}^2 - {D_{pitch,op,i}}^2) \frac{W_i}{4} \right) \tag{76}$$

Shaft design concerns the driving shaft of the pump, since its total width is assumed to be higher than the driven one and subjected to external loads, such as forces due to motion transmission to the pump. It is worth noting that the number of pump stages, gears facewidth, support dimensions, their number and layout are fundamental input data for the structural calculation. As part of the procedure, driving shaft has been outlined as a hyperstatic supported beam which can be structured with reference to the mentioned input data. The final outcome of this design phase is constituted by the minimum shaft diameter, which may be determined as follows:

$$d_{min} = \sqrt[3]{\frac{1}{\sigma_{am}} \sqrt{\left(\frac{32 \cdot Mb_{max}}{\pi} \right)^2 + 3 \cdot \left(\frac{16 \cdot T}{\pi} \right)^2}} \tag{77}$$

where σ_{am} is the admissible stress of shaft material and Mb_{max} is the maximum bending moment acting on the shaft.

The highest loaded support and working temperature combined to the lower speed of the driving shaft, describes the worst case scenario for the fluidynamic support. The design of the journal bearings, in particular of the radial clearance, is focused on the achievement of a satisfactory value of the minimum oil film, under these boundary conditions. In the actual calculation phase, an iterative procedure for the design of the bearings has been implemented. Input parameters set is formed by oil density and kinematic viscosity at maximum working temperature ρ, μ, minimum pump speed n_{min}, maximum support load P_{max}, shaft radius r, length of the bearing l_b, radial clearance δ_b.

Firstly, through the input parameters set, Sommerfeld number is calculated as:

$$S = \frac{\mu \cdot n}{P_{max}} \left(\frac{r}{\delta_b} \right)^2 \tag{78}$$

The methodology has been implemented by assuming the diagrams in Ref. [69] as reference for the calculation of relative eccentricity χ. The diagrams are specifically related to unitary bore diameter over length ratio bearings with singular axial groove. Thus, the eccentricity of the loaded floating shaft is obtained:

$$\varepsilon = \delta_b \cdot \chi \tag{79}$$

Finally, the calculation of the minimum height of the oil film ψ_{min} between shaft and bearing is expressed as:

$$\psi_{min} = \delta_b(1-\chi) \quad (> \psi_{lim}) \tag{80}$$

the control parameters ψ_{lim} is a lower limit established by good practices, with the purpose to ensures the fluidynamic support of the shaft.

3.7.3 *Tip and Flank Clearance Design*

The clearance between the gear tip circle and the pump housing has been determined by considering the dual effect produced by the tip clearance variation. Increasing clearance implies greater loss flows generated by the pressure difference between suction and pressure side, and consequently the massive reduction of the volumetric efficiency. This sort of problem is particularly relevant when the machine works at high temperature and high pressure drop. On the other hand, decreasing tip clearance may causes the spread of the pressure of the oil trapped between the tip of the gears and the internal surface of the housing, that reduces the mechanical efficiency of the pump. The phenomenon is more evident especially for low working temperatures. In both configurations power losses affect the pump efficiency and their behavior has been described in [60]. Assuming tip clearance δ_{tip} as input parameter, power loss due to tip leakages is defined as:

$$\mathbf{X} = \frac{\Delta P^2 W^4}{12\mu \cdot t_{tip}} \left(\frac{\delta_{tip}}{W}\right)^3 + \omega_{max}^2 \mu \cdot t_{tip} \left(\frac{D_{tip}}{2}\right)^2 \left(\frac{W}{\delta_{tip}}\right) \tag{81}$$

Since the procedure is oriented to pumps which work with low delivery pressure, balancing floating plates are not strictly required. Therefore, the flank clearance design procedure, implemented within this framework, reasonably

follows the tip clearance design philosophy. It is worth noting that the results strictly depend on the oil temperature. For this reason, the calculation needs to be carried out at maximum and minimum allowable temperature values, in order to guarantee that the chosen clearance represents the best compromise throughout the entire range of working conditions.

3.8 FINAL REMARKS

The current Chapter describes the development of a numerical tool for the reproduction of the performances of gear pumps which relies on a lumped parameters approach.

The model follows an iterative solution procedure where, for each discrete angular step of the gears, the micromotions and the internal pressure field are simultaneously solved. Since for the numerical model in general, and LP in particular, the discretization of the calculation domain represents a crucial step, the first novelty aspect implemented concerns an improved techniques for the calculation of both orifices and control volumes. Such approach is based on the 2D Delunay's triangulation mesh of the surfaces. The purpose is to avoid numerical errors that may alter the reliability of the results. At the basis of the meshing approach has been put the accurate reproduction of the gearpair and of the balancing plate grooves. While the grooves are imported from a cad model thanks to a dedicated tool, the gear reproduction is obtained through a calculation procedure that starts with the definition of a reduced number of input parameters. The gear calculation also represents a part of a multistage gear pump design procedure detailed within the dissertation.

In second instance, the continuity equations that govern the flowrate exchange between control volumes are solved through a improved version of the Bernoulli's equation. In particular, the model has the chance to autonomously shift from laminar to turbulent regime during the flowrate exchange, thanks to pressure dependent flow parameters. It descends that the model, after a validation procedure, is capable to pursue the internal phenomena with an improved flexibility and consistency. It is worth underlining that to emphasize the accuracy enhancing the coherent representation of the internal flowrates, the flow parameters have been separately specified for five families of orifices. Moreover, the description of the fluid-dynamic behaviour has been enhanced by the integration of the equations that describe the pressure influence on the

lubricant Bulk's modulus. A further relevant novelty aspect relies on the introduction of the shafts bending calculation for each angular step. The purpose is to better represent the tip clearance calculation since high pump pressurization introduces bending displacement comparable with clearances dimensions. Thanks to the pressure load calculation procedure integrated to study the gear equilibrium positions, it is also possible to estimate force ripples addressing the study of the potential NVH behaviour.

The model reliability has been assessed through an initial test campaign. The mean values of delivery pressure and flowrate measured from the operative tests have been considered as threshold values for the model validation. Furthermore, the acquisition of the pressure ripple waveform has given a further comparison object. The calibration of the flow parameters has been performed pursuing such three operative targets. Within the dissertation, a sensitivity analysis on the effects of the flow parameters tuning has been included. It is worth noticing that aside from the three major outcomes, the model allows to investigate the flowrate fluctuations between the entire set of control volumes. It descends that the tuning of the model does not concern only the pursue of the target performance but also the reproduction of coherent internal phenomena. The most relevant outcome of the validation is the flow parameters set that allows to better reproduce the pump behaviour. Then, a comparison between numerical and experimental pump mapping has been carried out highlighting the coherence of the results. The model has shown reliability on the pump replication even including a certain discrepancy on the flowrate estimation given by a lack of information regarding oil characteristics.

The potentiality of the LP tool for the study of improvement solution has been addressed through a dedicated case study. Furthermore, since the pumps adopted were equipped with helical gears, the model has been updated in order to deal with these gear layouts. The first part of the study has been oriented to the reproduction of the initial gear pump layout. Gearpair, lateral grooves, clearances dimensions, accurate lubricant parameters and the running-in profiles of the housing have been included within the pre-processing module. Then, in order to perform a comparative numerical mapping, the first set of simulations has been performed following the condition tested within a dedicated experimental characterization. The results of the initial activity confirm the robustness of the model showing great coherence on the reproduction of the pump performances. The greater accuracy of the lubricant data seems to

guarantee an improved consistency of the results. Moreover, thanks to the shafts bending calculation, the model replicates the strong volumetric efficiency recovery shown by the benchmark pump at high delivery pressure. Thanks to the post-processing tool, the results of the simulations have been deeply analysed to implement the improvement strategy. Since the pump has shown a strong pressurization followed by heavy pressure loads, the focus has been oriented on the improvement of the balancing plates. In this context, reducing the pump sealing it is possible to increase its speed avoiding pressure peaks and in parallel improve the efficiency.

Within the dissertation, the two most relevant solutions have been presented and discussed. The relief grooves proposed layouts are characterized by a diminished extension of the bridge combined with the displacement of the release edge toward the suction side. Furthermore, the pressurization arc extension has been reduced through the modification of the suction side. The new designs differ on the suction side displacement ratio. The numerical results show a general efficiency improvement for both layouts and for the entire set of simulations. In addition, the improved relief shows a slight improvement in terms of pressure load fluctuation. From the analysis of the efficiency map a strong diminish has arise at 100 bar of target pressure for the updated and original layouts. By means of the post-processing tool, the analysis of the internal leakages and clearances has revealed a lack of sealing within the pressure arc zone at this particular condition. The second improvement step has been performed with the purpose to overcome such phenomena trying to mitigate the efficiency drop. In this context, the pressure arc has been updated through the extension toward the inlet chamber of the internal housing circular profiles combined to the anticipation of the balancing plate groove edges. The scope of the solutions was to anticipate the vain pressurization giving to the gear tip a proper time to seal the clearance avoiding oil squeeze. Two step of increasing modification magnitude have been implemented and simulated. The results have shown a further general efficiency improvement with particular evidence on the 100 bar condition symptoms that the design assumption were reliable. Furthermore, the analysis of the results have highlighted how the novel set of development potentially improves the NVH behaviour reducing pressure and force ripples. On the basis of such numerical results, the updates have been implemented on two updated sample pumps. The dedicated test campaign confirms the beneficial

effect of the modifications in terms of efficiency improvement. The correlation observable from the efficiency maps comparison allows to finally confirm the reliability of the proposed LP model.

The residual discrepancies between the numerical model and the operative results reflect the absolute consistency of the implemented mathematical approach on the basis of the model. Furthermore, the accuracy and usability of the post-processing module provides a fundamental tool for the deep investigation of the pump internal phenomena. The improvement study carried out with the aim of the LP model has further highlighted the necessity of such tools to contain costs and waste.

4

DEVELOPMENT AND ASSESSMENT OF A FINITE ELEMENT MODEL FOR THE STUDY OF NVH IMPROVEMENT SOLUTIONS

The current Chapter is devoted to the description of a finite element approach to the investigation of the NVH behaviour of the hydraulic module of an agricultural hybrid continuous variable transmission (CVT). In particular, the model has been developed in order to evaluate improvement solutions to reduce the acoustical emissivity of the system. The hydraulic module has been subjected to a run-up speed test where vibrational response and acoustic emission have characterized by means of accelerometers and microphones. As preliminary step of the study, with the purpose to identify the critical excitations and structural responses, the operative noise and vibration experimental results have been processed and deeply analysed. Then, through a dedicated modelling strategy of the system components and connections, the model has been subjected to a validation procedure. The experimental results coupled with the mechanical system analysis has led to identify the responsible of the most hazardous excitations and responses. By means of the validated FE model, several enhancement solutions have been implemented and characterized.

4.1 INTRODUCTION

Within the industrial environment, the necessity to dispose of validated FE models for the characterization of a system behaviour has strongly increased over the last decades. It is imperative for the engineers to have the chance to transform, modify, substitute components within the system and directly evaluate the influence of the update without waste of material, energy and, in the end, money. Moreover, focusing on the automotive field, the crescent and

indisputable need improve the comfort of the final users, in terms of vibrations and noise, pushes the research to develop solutions for the numerical approach to the problem.

From the literature survey, one of the earliest study for the development of advanced methods for the numerical characterization of the NVH behaviour of mechanical systems was produced by Chikamori and Yoshikawa in [70]. Here, authors developed an analytical methodology for the estimation of the response frequencies and their influence on the noise emission, applied on vehicle drive trains. Furthermore, authors evaluated the influence of the introduction of dampers and other enhancements to reduce the transferability of the dynamic excitations to the axes. In this context, the works presented by Syed et al. in [71], and lately by Qu et al. in [72], has been oriented to the development of systems for the containment of driveline oscillations by means of an analytical dynamic model. Another relevant application was proposed by Kagawa et al. within [73] where a novel method for the estimation of the sound radiation power combined to the numerical modal analysis, analytically correlating the vibrational behaviour to the noise emission. As a matter of fact, the implementation computational modal analysis and frequency analysis represented a breakthrough on the enhancement of the NVH behaviour of mechanical systems. The work presented by of Lahey et al. in [74] proves the relevance of the methodology. In particular, with a study on a geartrain, it shows how the adoption of modelling systems in the early stages of the design may help to optimize the NVH behaviour of the product. In this context, the NVH optimization may be extended to more articulate systems such as car bodies as shown within [75]. The relevance of the approach may be proved by the diffusion of validated FE models for the representation of the natural frequencies of the mechanical systems in a great variety of industrial fields [76], [77]. A great contribute to the enhancement of the modelling strategy and correlation has been given by Mucchi et al. with the dissertation contained in [78]. The work is devoted to the integration of LP, FE and BE models. Authors have developed a LP model for the estimation of the excitations arising from the gear pump operating. Then, the excitation have been introduced within the FE model in order to evaluate the frequency response of the pump casing. Finally, the vibration level of the surfaces has been implemented into the BE model as input for the estimation of the radiated sound power level.

Within the automotive field, the work presented by Guj et al. in [79] shows the relevance of the FE analysis for the optimal design of cars damping layout. Then, Lu et al. proposed in [80] an algorithm based on a FE complex model for the optimization of the NVH behaviour of car body. For what concerns the development of FE methodologies, great relevance has been assumed by the work presented by Ramsey and Firmin in [81]. One of the earliest FE methods for the implementation of numerical modal analysis was here described and also the experimental comparison was reported. The experimental correlation with the numerical models represents an essential tool for the assessment of their reliability. The work of Allemang et al. [82] gives an overview of the basis of experimental modal analysis methods developed over the last fifty years. Within this context, Bucher and Ewins in [83] presented a dissertation on the modal analysis techniques for rotating structures. Furthermore, Peng et al. in [84] proposed the implementation of modal analysis to obtain the in-process response functions, while Karaağaçlı dealt with non linear system modal analysis in [85].

Since hydraulic pump noise emission represents an extremely relevant issue for the NVH improvement within mechanical system, the literature presents several works on this topic. In particular, based on modal analysis techniques, Mucchi et al. in [86] and lately the works [87], [88], [89] and [90] presented studies over the structurborne noise emission of hydraulic pumps. On the other hand, the development of integrated FE and boundary element (BE) models [91], [92], [93] , [94], [95], [96], has given the chance to design noise-effective solutions through validated numerical tools.

The brief description of the evolution and integration of the computational techniques involved into the NVH improvement activities represents the starting point for the implementation of a FE model and for the analysis of the excitation sources. In particular, if the involved system is constituted of several bodies, the post processing of the experimental data is essential to discern the most impacting noise and vibration sources. Furthermore, it is important to understand the operating principles of the whole system and potential design improvement strategies in the early stages of the activity. Within the following sections will be presented the development of a FE model of a portion of a tractor CVT. The study has been required since the noise emission of the involved tractor has result into comfort issues for the final users. Moreover, as will be shown hereafter, the system has already been subjected to an unsuccessful

enhancement study that has not been carried out by our research group. The implementation and validation of the FE model has been performed following the salient aspects showed within previously mentioned dedicated studies. The adoption of a validated FE model for the prediction of the NVH behaviour of such portion of the CVT bounded with the hydrostat and its connections modelling technique, represents a novelty topic that does not find similar cases within dedicated literature. The possibility to straightforwardly implement and evaluate NVH enhancement solutions with absolute reliability, combined with the widespread of such transmission technologies in the automotive and agricultural fields, gives further relevance to the presented study. The initial Section of the current Chapter is devoted to the brief description of the baseline system involved within the study and to the description of the updated layout. Section 4.3 concerns the analysis of the post processed data from the experimental characterization of both system layouts. Then, Sec. 4.4 deals with the description of the FE modelling of the system, presenting also its validation with respect to the operative data. While Section 4.5 is devoted to the analysis and implementation of NVH improvement solutions, Section 4.6 is devoted to the final remarks.

4.2 DESCRIPTION OF THE HYDRAULIC MODULE INTEGRATION ON AN AGRICULTURAL CVT

A continuous variable transmission consists into a transmission system that ensures seamless power transfer from the engine to the wheels and infinitely variable speed at peak mechanical efficiency. The widespread of such families of transmission is essentially linked to the strong comfort improvement ensured by the smooth speed transition and imperceptible shifts. Furthermore, the capability to run the engine at its higher efficiency curtail the fuel consumption [97], [98]. They are used in very demanding applications, which require high-power transmission such as agricultural tractors [99], [100], [101].

A schematic view of the CVT is depicted within Fig. 65. As can be seen, it is straightforwardly constituted by a planetary gearbox, a synchronized mechanical transmission, and an hydrostatic module (HM). The engine drives the solar shaft of the planetary gearbox and simultaneously drives the HM input gear. The output HM shaft is coupled with the planetary gearbox ring while the carrier is connected with the mechanical transmission. Figure 66

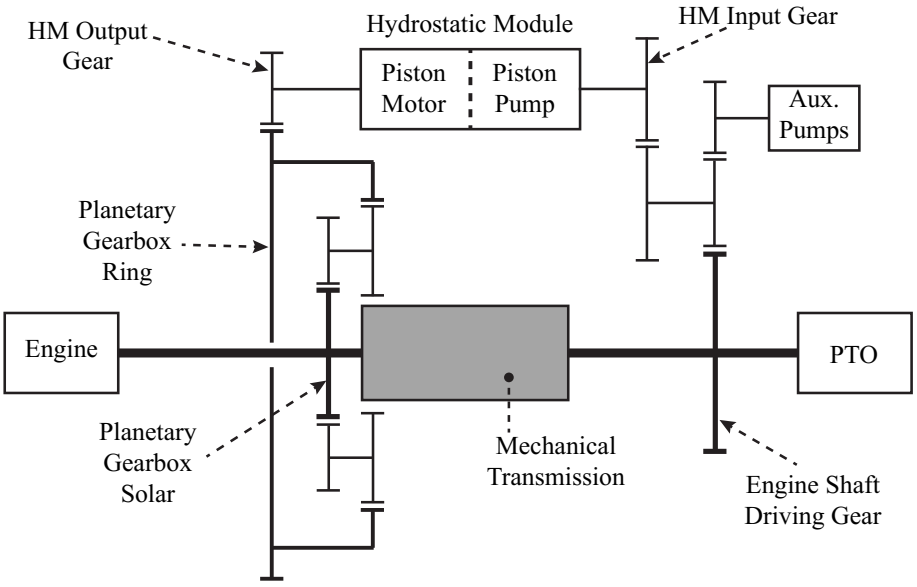

Figure 65: Schematic view of the CVT components

gives the chance to briefly describe the HM operating principles and how it influences the power transmission of the CVT [102]. It is constituted by an axial piston pump, equipped with z_{pump} pistons, integrated with an axial piston motor, equipped with z_{motor} pistons. The angular position of the pump swash plate is the responsible of the delivery pump flowrate variation [103]. Such flowrate also represents the input flowrate of the piston motor. Since the swash plate remains fully swivelled, the HM output shaft speed do not change. In this context, the planetary ring and the solar shaft speed differences do not provoke the carrier rotation and the drive speed of the vehicle remains zero. Moving the swash plate, the flowrate decreases and the piston motor reduces the output shaft rotational speed. In this condition, the ring speed no longer neutralize the rotational speed of the planetary gears causing the power transfer to the wheels. From a dynamic effect point of view, the nature of the pumping action of an axial piston pump introduces axial pressure load components. The inclination of the swash plate also generates radial components that may excite the pump casing resulting into undesired noise issue [104], [105].

The system involved within the here described activity is a portion of the CVT and its 3D representation has been included within 67. Cover, flanges and HM constitute a unique system which is then bolted to the driveline frame

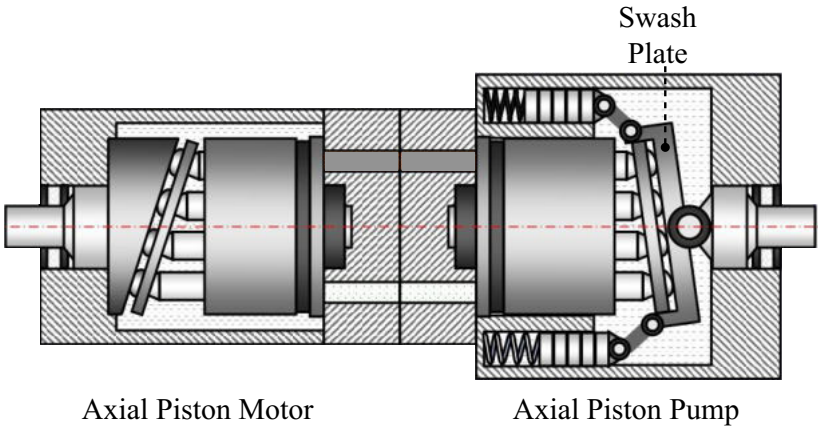

Figure 66: Schematic view of the hydrostatic motor

through the holes of the cover rib. The HM is connected to the cover by means of input and output flanges. Within this context, it is worth underlining that the NVH improvement activity follows an unsuccessful enhancement project, that, for sake completeness has been studied and here described. Hereinafter, the original layout of the system will be named as *baseline*, while the second layout as *suspended*. The main constructive difference between the layouts rely on the HM connections with the input and output flanges. In the *baseline* configuration, the HM has been pinned on the input flange by means of two steel mounts, as shown in Fig. 68(b). On the contrary, with the purpose to isolate the HM from the flange, it is supported by an elastic ring on the output side as shown in Fig. 68(a). In this context, is clear that when the system is connected to the driveline frame, the HM acts as a cantilever beam since the steel mounts stiffness strongly overcome the elastic mount one. Thus, the excitation that arise from the HM operating are completely transmitted by the mounts to the input flange and finally on the end cover. Regarding the *suspended* configuration, the designers have replaced the two steel mounts on the input side with four damped mounts. Contextually, the elastic ring on the output side has been replaced with two equal damped mounts. Figure 69 helps in the comprehension of the proposed layout. The erroneous idea at the basis of such connection scheme, relies on the intention to isolate the HM from the rest cover and flanges systems curtailing the hydraulic excitation transfer.

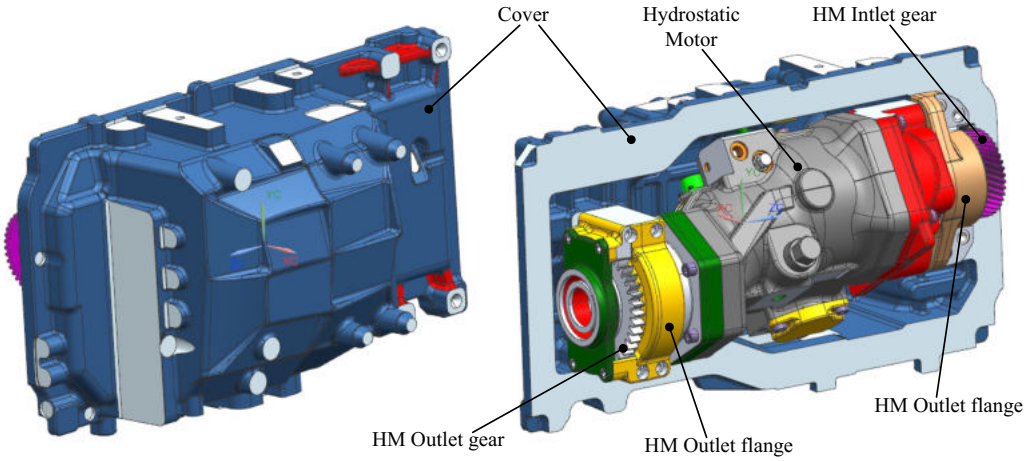

Figure 67: Schematic view of the hydrostatic motor

Aside from the flanges connections, the two configurations have not reported further connection differences. Thus, a particular focus needs to be given to the HM shafts links with the input and output gears. From Fig. 68 it is possible to see that input and output gears are connected to the respectively flanges by means of two bearings while the connection with the HM shafts take place through two steel joints. Such steel spline joints adopted to couple the shafts to the gears theoretically ensure an axial degree of freedom to the HM. As a matter of fact, the constraint ensured by a roller and a ball bearing do not allows axial or radial DOF to the gears. On the contrary the HM may be subjected to slight displacement resultant from mounts or flanges deformations. However, it is worth noticing that during the torque and power transmission, it is allowed to assume that the contact stiffness neglect the axial freedom constituting a virtual unique body from the input to the output gear. From this assumption, it descends that the HM operative excitations are eventually transferred either to the input and the output flange. With a further analysis of the connections, it is clear that the excitations coming from the input and output gears meshing are indisputably transferred to the cover through the bearings and to the HM by means of the spline joints.

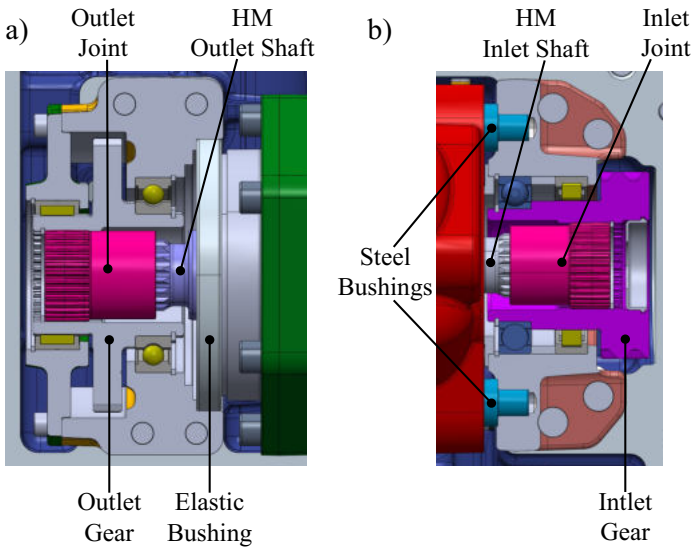

Figure 68: Baseline layout mounts on the output side (a) and input side (b)

4.3 ANALYSIS OF THE EXPERIMENTAL CHARACTERIZATION RESULTS

The experimental characterization of the two layouts has been performed installing the cover equipped with HM, flanges, bearings and gears on the driveline frame and operating a run-up analysis. In particular, for the experimental activity the engine speed has been carried from n_{min} to n_{max} with maximum stationary torque on the tractor axles. Furthermore, the tractor travel speed has been set on the constant value. Such condition is achievable thanks to the hydraulic module of the CVT that, varying the swash plate position, regulates the output shaft speed neutralizing the engine speed increment. The CVT noise emission has been monitored by means of a prepolarized microphone positioned in proximity of the external surface of the cover. Moreover, the vibrational behaviour of the cover has been evaluated by means of 5 triaxial piezoelectric accelerometers positioned as shown within Fig. 70(a). Following the picture framework, such sensors are characterized by letter *P* which stands for passive side. On the contrary, the sensors mounted on the HM surface are shown in Fig. 70(b) and represent the "active" side sensors with reference to the associated letter *A*.

From the brief description of the operating principles provided within Section 65, it is possible to understand *a priori* the most effective frequency

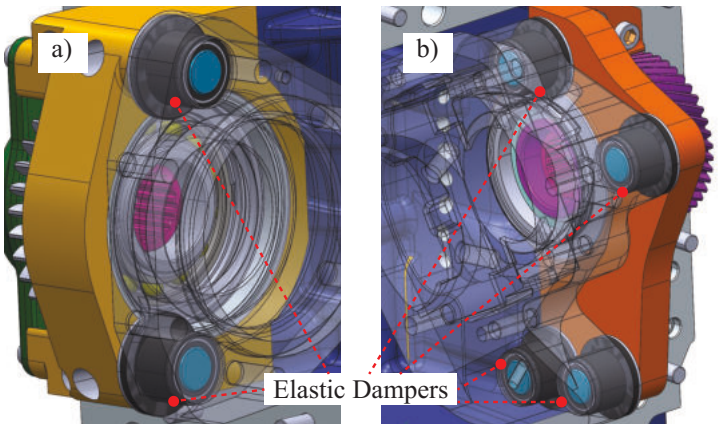

Figure 69: Suspended layout mounts on the output side (a) and input side (b)

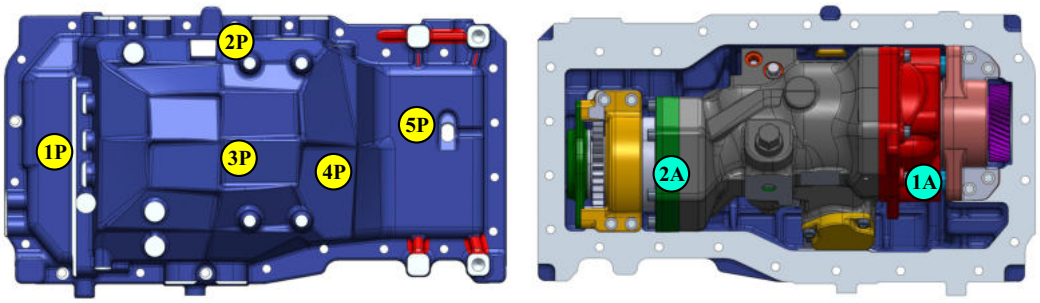

Figure 70: Representation of the accelerometers locations for the experimental measurement setup

components recognizable within spectrum and waterfalls. In first instance, is reasonable to expect that the characteristics frequencies of the piston pump and motor will represent the most effective components detected by the sensors. In this context, the pump and motor characteristic orders (O_{pump}, O_{motor}) may be calculated as follow:

$$O_{pump} = \tau_{eH} \cdot z_{pump} \tag{82}$$

$$O_{motor} = \tau_{eH} \cdot z_{motor} \tag{83}$$

where τ_{eH} represents the transmission ratio between HM input gear and the engine driving shaft gear, z_{pump} is the number of pistons of the pump, while z_{motor} is the number of pistons of the motor.

Furthermore, the microphone and vibrational spectrum may include the input and output gear meshing orders. O_{in} and O_{out}) should be calculated as:

$$O_{in} = \tau_{eH} \cdot z_{in} \tag{84}$$

$$O_{out} = \tau_{eH} \cdot z_{out} \tag{85}$$

where z_{in} and z_{out} represent the number of teeth of input and output HM gear respectively. It is worth underline that to prevent the divulgation of sensible informations, the results and the system data have been reported in adequate non dimensional form.

The analysis of the experimental campaign results may start with the comparison of the microphone waterfall diagrams in baseline and suspended configuration included within Fig. 71. In order to evaluate the effect of the noise emission in terms of human acoustic comfort, the reported SPL are A-weighted and are compared within a reasonable frequency range since higher frequencies are less noticeable for human hearing. While the SPL has been non dimensionalized with respect to a proper maximum value that allows to have a reasonable waterfall scale, the frequency axis has been referred to the maximum investigation value. Symptom of a low effective enhancement, the graphs do not show sensible differences. As expected, the most relevant components of the spectrum are the harmonics of pump and motor orders which are particularly emissive for the entire test. For sake of clarity only the first and second harmonics have been highlighted within the figures. Furthermore, from the graphs arises the absolute relevance, in terms of noise emission, of the meshing order of the output gear. The first and the second harmonic show high SPL values throughout the entire test. To further analyse the acoustic results, within Fig. 72 the SPL octave-third spectrum [106] shows that between the two configurations there are no appreciable differences. The SPL level axis follows the waterfall process while the octave band value have been normalized with respect to the first considered band. The *suspended* condition reports a lower level for the 15.6 band while the 25 one exceeds the *baseline* value generating a resultant 0.0035 gain in terms of overall non dimensional SPL.

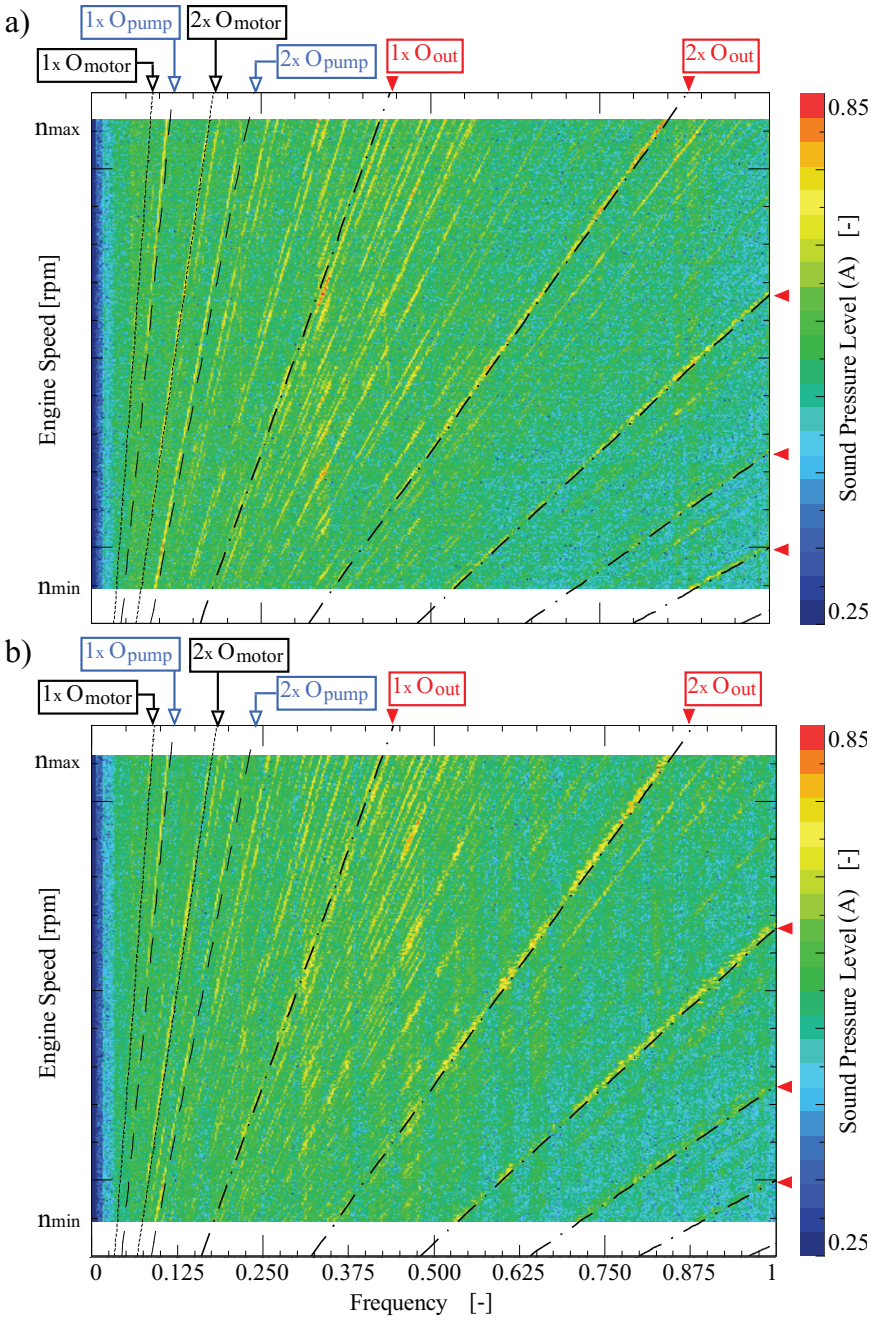

Figure 71: Non dimensional SPL waterfall measured with baseline configuration (a) and suspended configuration (b)

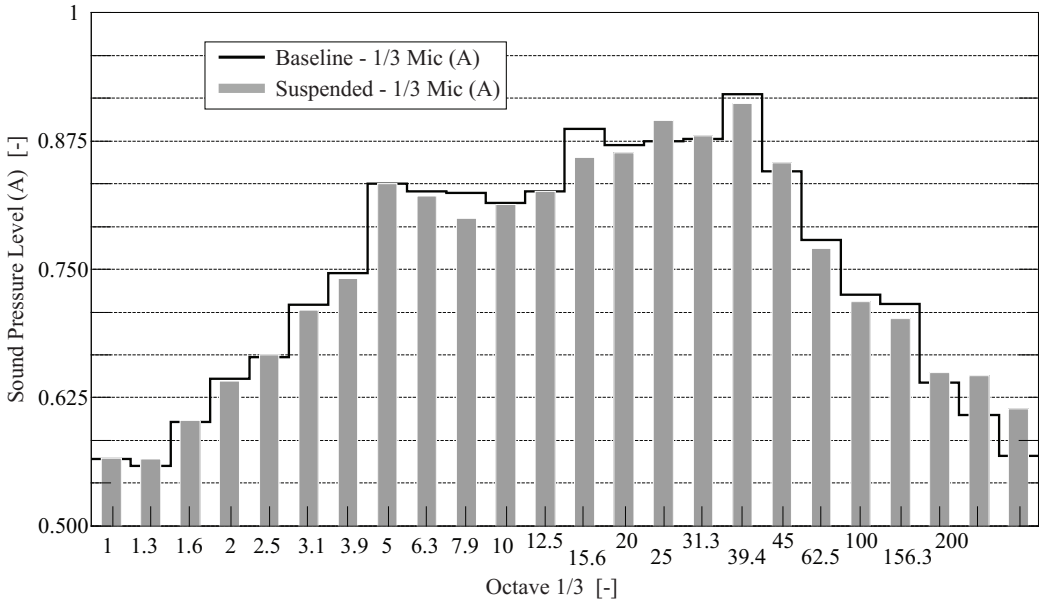

Figure 72: Comparison between baseline and suspended SPL octave-third spectrum

The analysis of the accelerometers acquisitions has been performed considering the upstream-downstream waterfalls, calculated in axial and radial direction. In particular, with reference to Fig. 70, the acquisitions of the accelerometers *1A*, *2A* are considered as upstream signals while *1P*, *5P* are the respectively downstream signals. The figure also shows the reference frame adopted both for the measurement and post-processing. Since the cover usually represents a source of undesired noise emission, such comparison it is mandatory to understand how the cover respond to the excitations coming from the HM pumping actions and from the meshing loads of input and output gears. In this context, it gives the chance to evaluate the correlation between the vibrational response components and the emissive sources displayed by the acoustic waterfalls. On the other hand, the parallel comparison between baseline and modified configuration allows to understand the differences between the layouts both in terms of hydrostat excitations and transmission to the cover.

Figure 73 shows the comparison between the radial components of the signals, measured on the inlet side of the HM. Even for the acceleration signals, the most effective components are the HM orders. In both configurations, the accelerometers located on the hydrostat pump side do not show differences

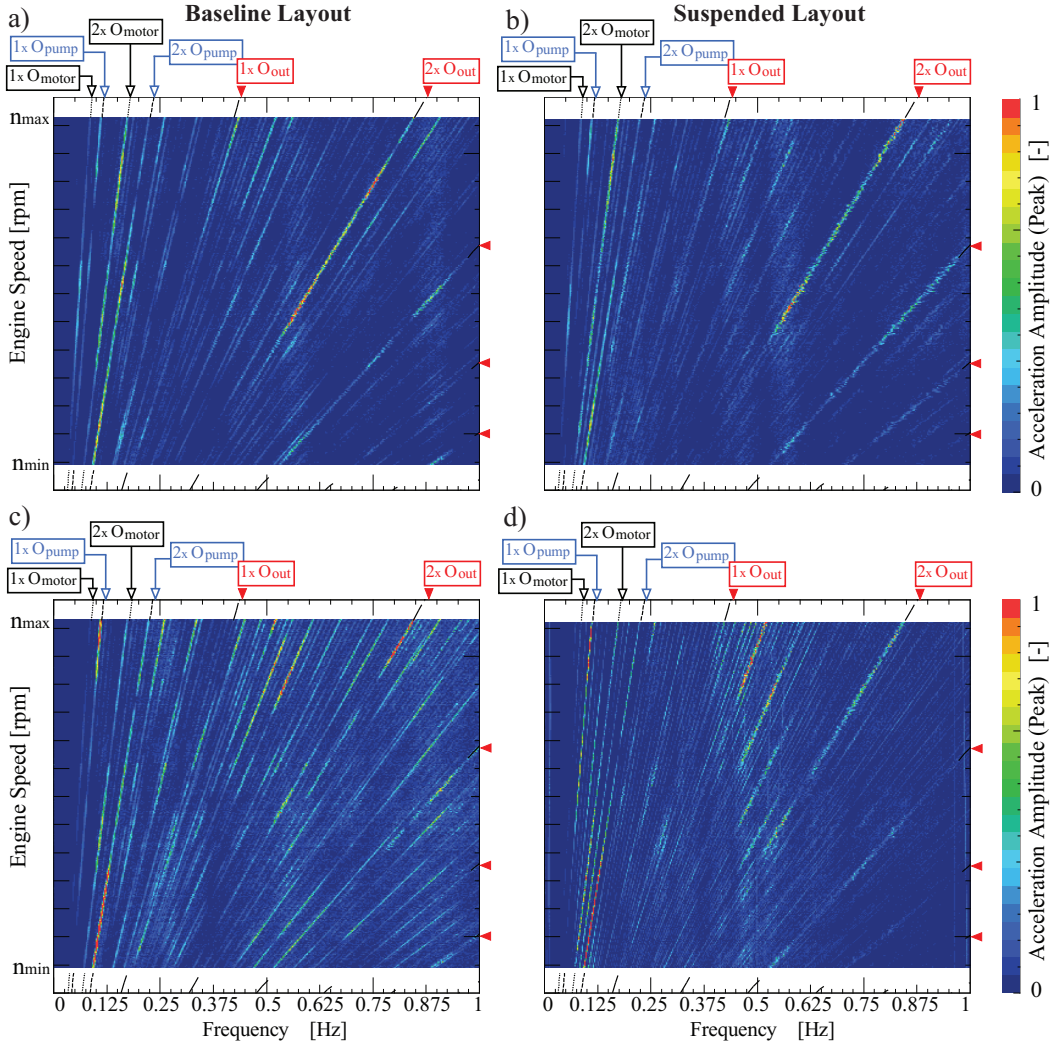

Figure 73: Waterfall diagram for the Z-signal measured by accelerometer 1A in *baseline* configuration (a), 1A in *suspended* configuration (b), 1P in *baseline* configuration (c) and 1P in *suspended* configuration (d)

or remarkable structural resonances (Fig. 73(a),(b)). Otherwise, the second harmonic of the outlet gear meshing order is particularly evident. The downstream signals measured on the cover by accelerometers *1P*, aside from the HM components, show slight differences between the layouts. The rigid connection ensured by the steel mounts in the baseline layout seems to emphasize the HM harmonics on the casing. Despite such phenomena increase the vibratory level,

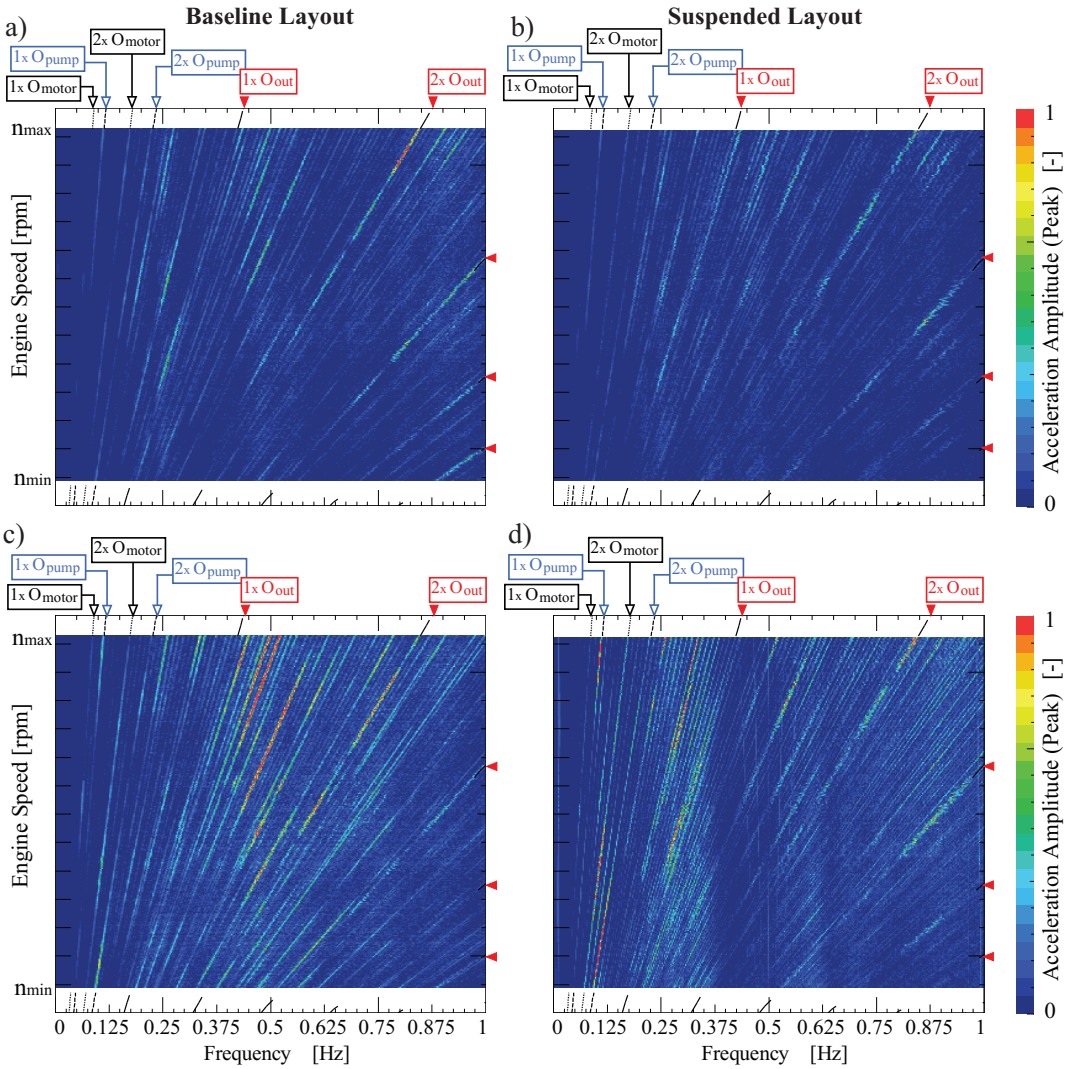

Figure 74: Waterfall diagram for the X-signal measured by accelerometer 1A in *baseline* configuration (a), 1A in *suspended* configuration (b), 1P in *baseline* configuration (c) and 1P in *suspended* configuration (d)

from the acoustic point of view the microphone waterfalls have not shown noise issues. Following the same framework, Fig. 74 shows the comparison for the axial components. The results are similar to the radial direction graphs with a resonance excitation displayed in baseline layout around the 0.5 non dimensional frequency (NDF) that have not shown particular amplification

from the microphone waterfall. The vibrational response on the HM outlet

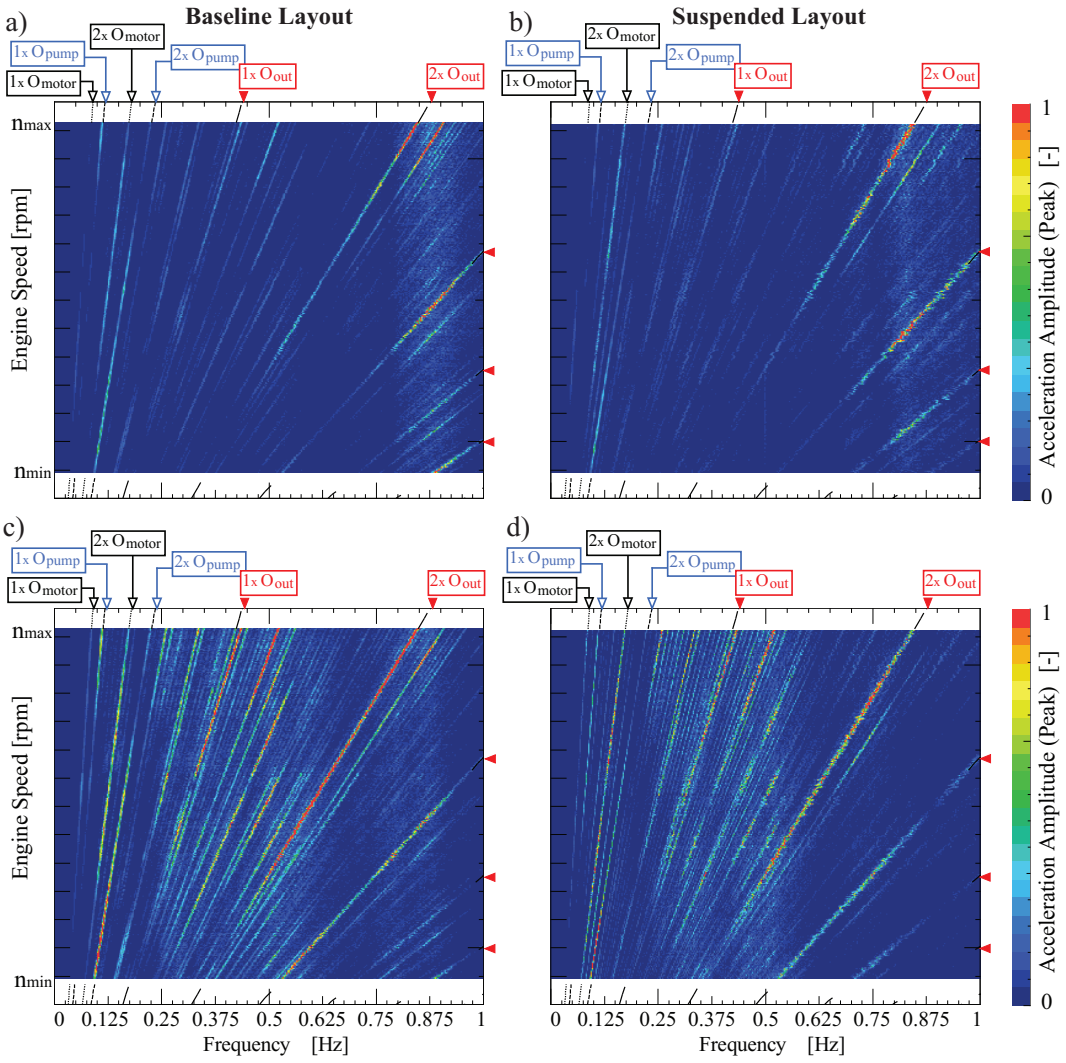

Figure 75: Waterfall diagram for the Z-signal measured by accelerometer 2A in *baseline* configuration (a), 2A in *suspended* configuration (b), 5P in *baseline* configuration (c) and 5P in *suspended* configuration (d)

side may be described with reference to Figure 75 that shows the radial components of the acquired signal. From a first overview, it is clear that even on this side the design modifications have not introduced substantial enhancement. In fact, the motor side accelerometer waterfalls of Fig. 75(a)) and (b) display a

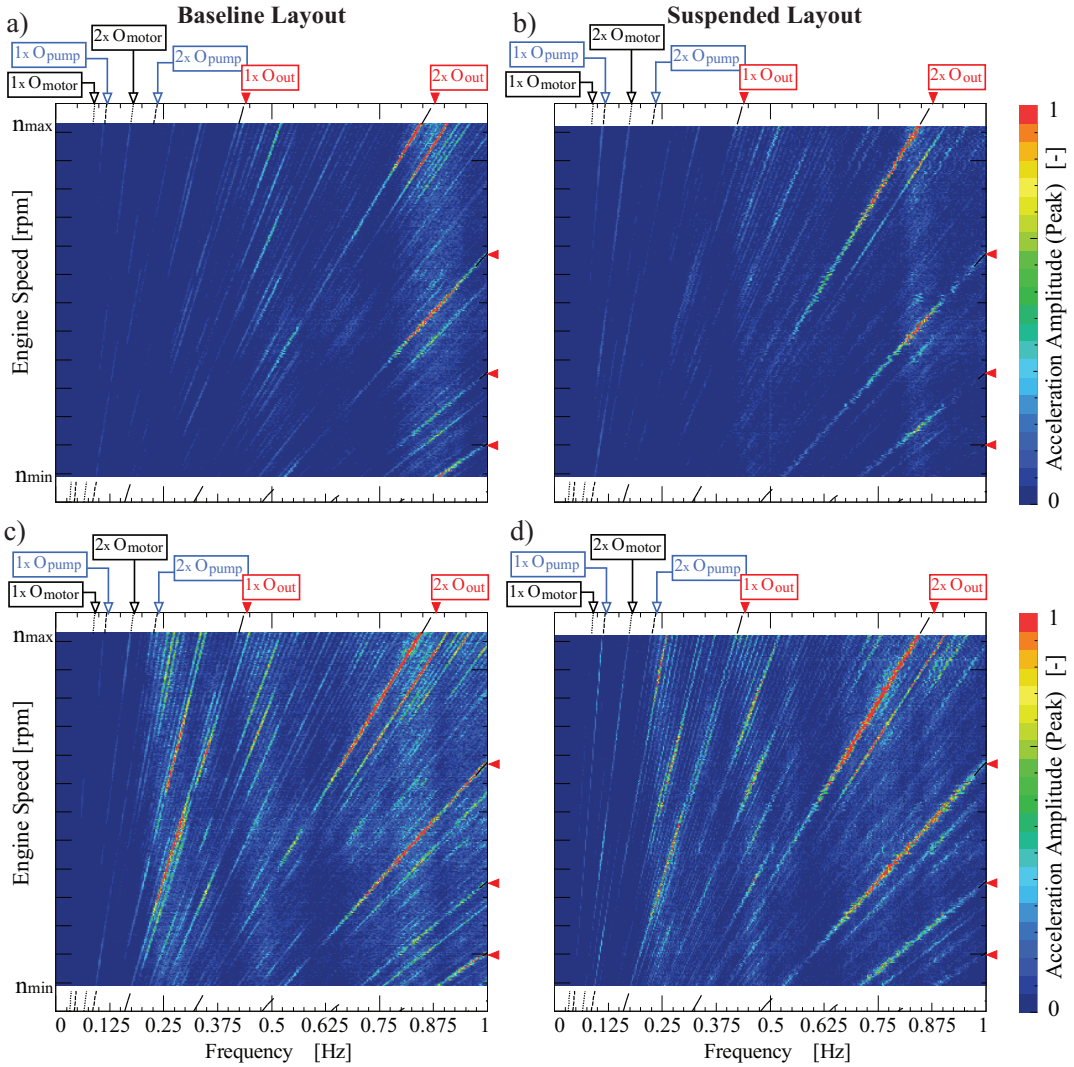

Figure 76: Waterfall diagram for the X-signal measured by accelerometer 2A in *baseline* configuration (a), 2A in *suspended* configuration (b), 5P in *baseline* configuration (c) and 5P in *suspended* configuration (d)

resonance area, around the 0.875 NDF, that emphasize the HM response to the outlet gear meshing order harmonics. It is worth focusing on the downstream response measured on the cover. The outlet gear components are here extremely evident in both layouts. The comparison with the microphone results highlights the correlation between such excitation transfer and the acoustic

Table 4: Mount connections properties

$k_{m1}{}^{x}$ [kN/mm]	$k_{m1}{}^{y,z}$ [kN/mm]	$c_{m1}{}^{x}$ [N · s/mm]	$c_{m1}{}^{y,z}$ [N · s/mm]	$k_{m2}{}^{x}$ [kN/mm]	$k_{m2}{}^{y,z}$ [kN/mm]
4.1	13	0.2759	0.087	1200	18000

phenomena. Moreover, the is evident a large resonance area between 0.25 and 0.575 NDF that might include several modes of the components involved. The axial signals reported within Figure 76 confirm the high response of the casing to the meshing excitation and also highlight a further resonance area within 0.75 and 1.

The brief analysis of the post-processed data has been fundamental to understand and confirm that suspending the hydrostat is not the way to pursue. The introduction of the dampers turns the HM into a labile body which is more free to respond to its internal excitations. In this context, the connections between shafts and gears, obtained by means of the spline joints, became the unique constraints to the hydrostat operative displacements and simultaneously act as transferring points for the internal and external excitations. On the basis of the preliminary assumptions corroborated by the analysis of the operative data, the NVH enhancement strategy has been traced. Otherwise, to evaluate the impact and the magnitude of improvement solutions it is mandatory to have a digital tool that allows to implement them without material and energy wastes.

4.4 DEVELOPMENT AND VALIDATION OF THE SYSTEM FE MODEL

The FE modelling has been performed taking into account only the baseline layout. In this context, since the hydrostatic module is a component produced by a company different from the CVT manufacturer, its natural frequencies, modal shapes or excited resonances are not object of hypothetical improvement solutions. Thus, it has been considered as a concentrated mass m_{HM}, located in its center of gravity and characterized by its proper matrix of inertia J_{HM}. On the contrary, cover, flanges and gears have been modelled as 3D meshed bodies. Finally, bearings, spline joints, elastic ring and mounts have been modelled as 1D connections, attributing their relative stiffness and damping.

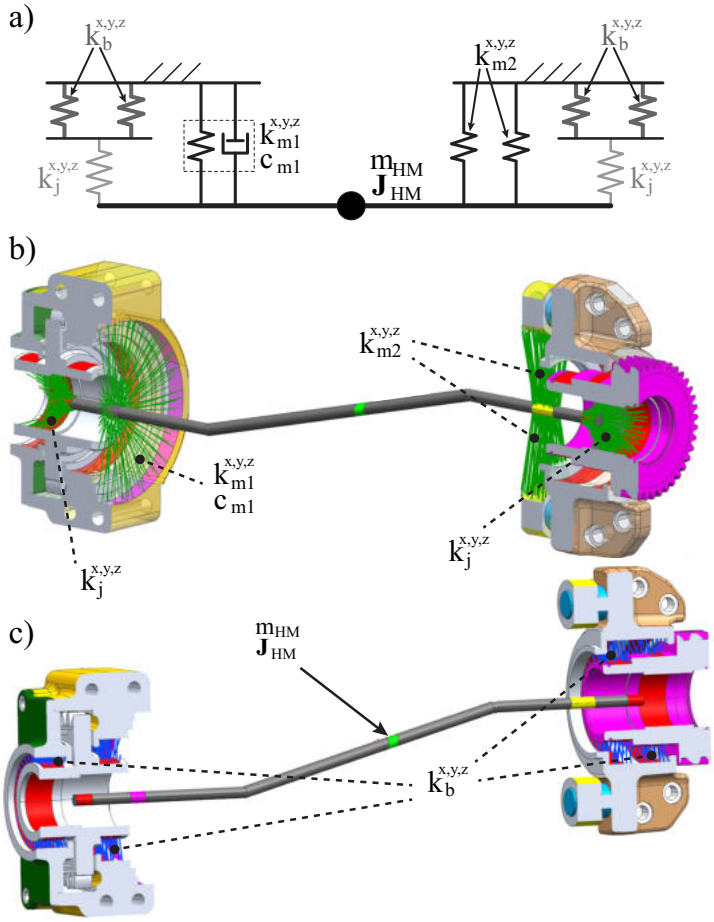

Figure 77: Schematic representation of the connections implemented within the FE model (b) and view of the 1D connecting elements of the model (b)

A schematic view of the connections between the involved components is given within Fig.77(a). The fixed part on the picture represents cover and flanges as a unique body thanks to the bolted joints. The HM is here directly connected through the two steel mounts represented by the in parallel springs characterized by the stiffness k_{m2}. Furthermore, the direct connection is ensured by the elastic ring on the outlet side which has been described introducing its stiffness k_{m1} and the viscous damping coefficient c_{m1}. Input and output gears have been 3D modelled and have been simultaneously connected with the cover through the springs representative of the bearings k_b and with the HM through the spline joints k_j. It is worth noticing that the

Table 5: Bearings and joint connections properties

$k_b{}^x$	$k_b{}^{y,z}$	$k_j{}^x$	$k_j{}^{y,z}$
[kN/mm]	[kN/mm]	[kN/mm]	[kN/mm]
740	7400	29	2900

superscript x, y, z characterized the different stiffness values for the 3 directions. The values attributed to the 1D elements have been included within Tab. 4 and 5. While for the elastic mount the physical properties have been assumed from its data sheet, for the steel mounts the characteristics have been calculated by means of a local FE stress analysis. The difference between radial and axial stiffness of the mounts ($k_{m2}{}^{y,z}$, $k_{m2}{}^x$) is due to the fact that the radial value is the steel pin value while the axial derive from the HM press fitting coupling on the pins. Bearing stiffness k_b has been considered constant for the four bearings involved. Such simplification descends from the results of a dedicated sensitivity analysis to the singular stiffness modulation that have shown slightly perceptible effects. As well as for the steel mounts, the spline joint radial stiffness has been evaluated by means of a FE stress analysis while the axial value has been estimated considering the axial degree of freedom partially constrained by the operating torque transmitted by the teeth in contact.

Figure 77(b) gives the chance to understand how HM and relative connections have been modelled. In particular, the hydrostat has been replaced by a *Z-shaped* beam which is responsible to connect the HM concentrated mass and inertia with the adjacent bodies. In order to avoid the detection of beam proper modes that may affect the results of the frequency analysis, the beam has been modelled with fictitious Young's modulus and density that brought its natural frequencies far from the monitoring zone. The 1D elements connect the target surfaces of the *Z-shaped* beam to the target surfaces of the involved elements. The extension of such surfaces has been modelled on the basis of the contact areas between the elements. Figure 77(c) shows the connections that simulate the bearings between gears and flanges. Within Figure 78, is reported the view of the meshed model with the implemented connections. It is worth noticing that the nodes of the cover rib frontal surface have been entirely constrained simulating the bolted joint with the driveline frame. The material identification has not been communicated by the company owner

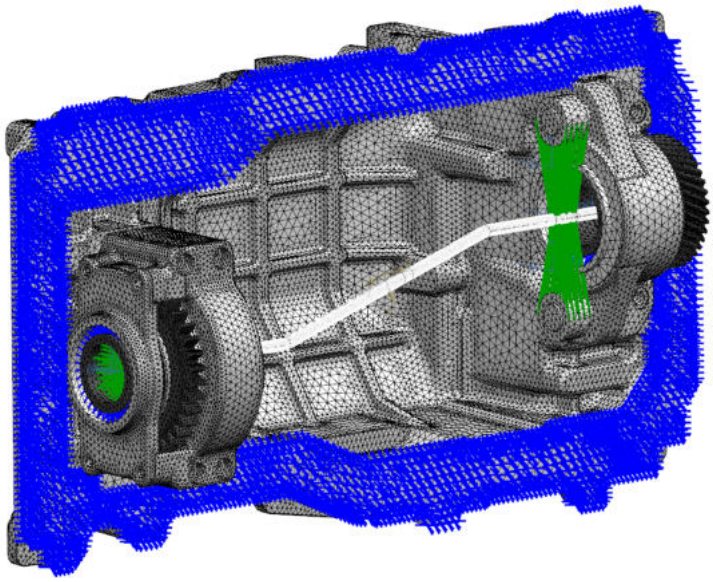

Figure 78: View of the meshed bodies and implemented connections

of the system. Otherwise, for the purpose of the activity, the main physical and mechanical characteristics, such as density, Young's module and Poisson's ratio, have been revealed. Thus, while cover and flanges are constituted by cast iron, the gears are steel made. The beam involved to replace the hydrostat has been modelled with fictitious density equal to $1 kg/m^3$ and Young's module $10^{15} GPa$.

4.4.1 *Numerical Frequency Analysis*

The first step for the assessment of the FE model has been the implementation of a frequency analysis that gives the chance to evaluate the response of the system to a frequency dependent excitation. In order to reproduce the most consistent excitation sources investigated within Sections 4.2 and 4.3, the HM concentrated mass has been excited by means of a triaxial sweep sine load. To contain the computational effort, the sweep has been performed with 1.25% increment steps. Furthermore, the loads have been applied with constant amplitude equal to 1N. Since the excitation is different from the operative excitation generated by the hydrostat, the results of the analysis

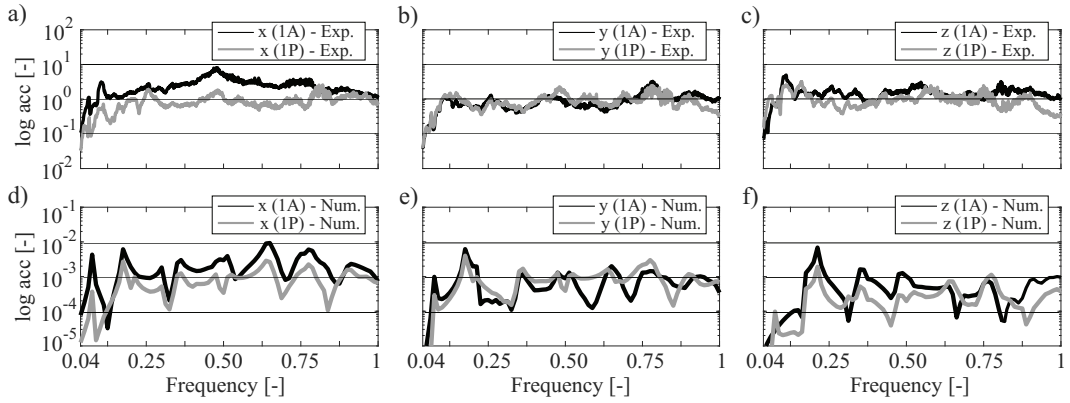

Figure 79: Upstream-downstream spectrum comparison for the signal measured in positions 1A-1P from experimental test (a), (b), (c) and numerical simulation (d), (e) and (f)

will be representative of the shape of the system response frequency. On the contrary, the mean value of the response will not be comparable.

In order to reproduce the experimental results, even for the simulation the response frequency has been monitored on the mesh nodes corresponding to the accelerometers positions. Within Figure 79 the upstream and downstream spectrum for the accelerometers on the inlet side are reported, giving the chance to evaluate the transmissibility on the three directions. In first instance it is possible to see that, aside from the axial direction 79(a), the excitation measured by the accelerometer on the HM is directly transferred on the cover side. The numerical spectrum reported in Figures 79(d)-(f) show the coherence of the results for the reproduction of the compared signals. Despite the numerical analysis has been carried out with an higher sampling frequency and, consequently, lower spectrum resolution, the model is capable to capture the same overlap characteristics of the experimental data. The frequency axis has been normalized with respect with the maximum investigation frequency. The result is further confirmed by the comparison given within Figures 80. Here, the spectrum are referred to the sensors located on the outlet side of the HM. In this context, it is worth noticing that for the radial components showed in 80(b), the cover sensor has measured an intensification of the excitation within the $0.25 - 0.625$ NDF zone and around 0.875, which are frequencies that have shown noise intensification from the microphonic waterfall of Fig. 71(a).

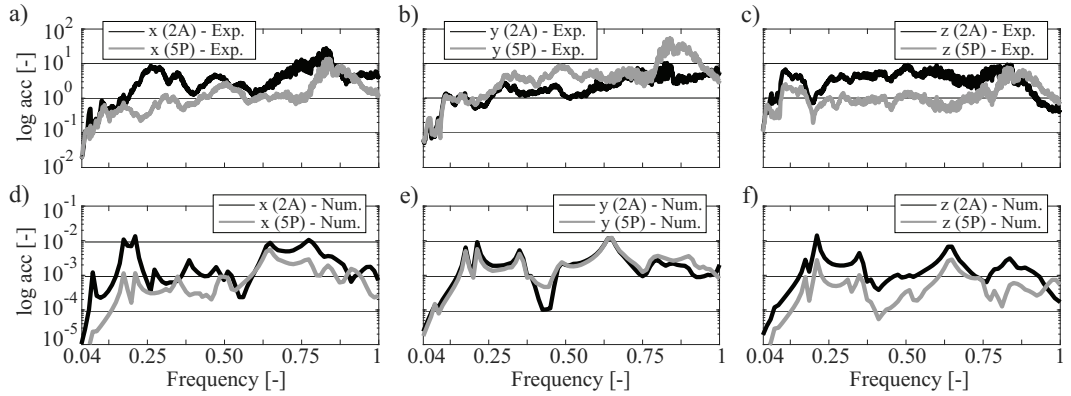

Figure 80: Upstream-downstream spectrum comparison for the signal measured in positions 2A-5P from experimental test (a), (b), (c) and numerical simulation (d), (e) and (f)

Since the model is eligible of a good coherence with the experimental results, it is worth focusing on the shape of the modes excited by the numerical frequency analysis. The focus on the baseline results showed within Figures from 71 to 76 and then on Fig. 81 helps for the evaluation of the coherence of the simulation with the experimental results in terms of noise emission. For sake of clarity, it is worth mentioning that Fig. 81 includes an instantaneous view of the modes excited at certain frequencies. In particular, the pictures report the highest emphasized deformations to ensure a clearer view of the modes. Moreover, the reference frequency assumed for the modes is the frequency where the structure presents the higher displacement. On the contrary, the analysis shows that the modes are excited in a certain range around these peak frequencies. The shape of the first relevant result is shown Within Fig. 81(a). The structure shape highlight that excitations with 0.20 of non dimensional pulsation frequency generates a vertical displacement of the entire flanges and HM system. Such mode is particularly highlighted within Fig. 75(a) where the accelerometer on the motor side of the HM reveals that around 0.20 the pump and motor orders are emphasized at every tested speed. On the contrary, either for the level curtailment given by the A-filtration, the microphonic waterfalls has not shown critical emission in such zone.

Within Fig. 81(b) is presented the deformation highlighted around 0.25 of NDF. A local deformation of the cover on the outlet side suggests that the mode may be originated by a lack of stiffness of the structure in such area. The

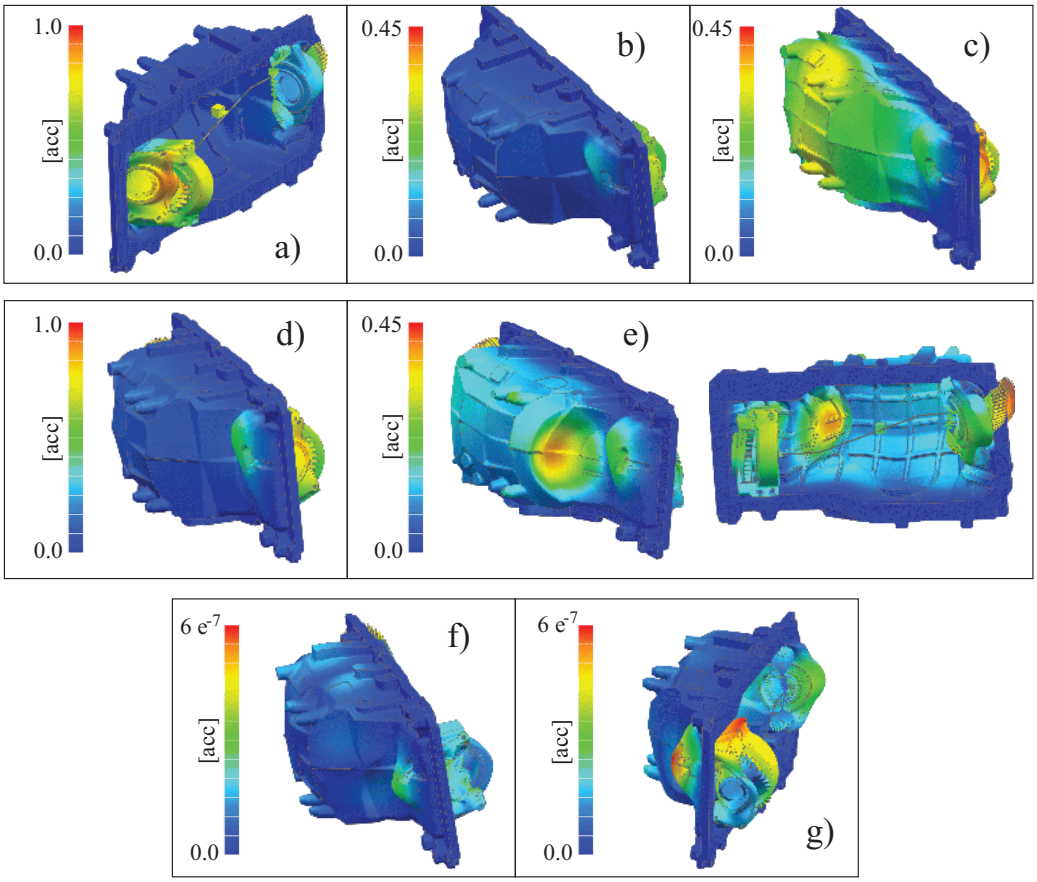

Figure 81: Frequency response analysis results in terms of nodal accelerations at NDF of 0.20 (a), 0.25 (b), 0.31 (c), 0.35 (d), 0.51 (e), 0.65 (f) and 0.88 (g)

resonance band has been clearly revealed from the waterfall of the sensor in 5P positioned in this zone in both direction showed within Figures 76(c) and 75(c). Even in this case the microphone has not measured critical emission. Thus, Figure 81(c) presents the response presented by the cover to the 0.31 excitation. Around such NDF, increments of the sound power level has been presented within the waterfall of Fig. 71(a) and highlighted by the 0.31 bar of the octave spectrum in Fig. 72. It is worth underline that the overall level of such bar might be influenced and emphasized by the response at 0.35 visible within Fig. 81(d). Even in this context, the deformation is localized on the flat surface of the cover on the outlet side. It is reasonable to assume that the resonance

bands displayed in Figures 76(c) and 75(c) between 0.25 and 0.38 are generated by similar cover responses.

A particular focus is required by the response observed at 0.51 of NDF, reported in Fig. 81(e). Even in this case, the flat surface on the cover outlet side is the mainly involved on the response mode presenting an extremely localized deformation. Moreover, the outlet flange connected to the cover generates a rotation of the hydrostat that results into the deformation of the inlet flange and into the consequent deformation of the inlet side of the cover. The analysis of accelerometers waterfalls highlight the presence of an amplifying band within 0.50 and 0.58 visible for the cover accelerometers and even for the HM side sensors. The microphone waterfall also presents an excitation band symptoms that the excited mode provoke noise increment. Increasing the forcing frequency, the simulation has revealed several localized response modes around 0.65. An example has been reported in Fig. 81(f). Such modes are visible from the highlighted band presented by the waterfall of Fig. 75(c) for the radial direction, perpendicular to the cover surface. The last relevant response observed from the analysis has been observed with the 0.88 non dimensional forcing frequency. Such frequency was observed as particularly emissive in terms of SPL both from the waterfall and from the octave spectrum. Furthermore, the acceleration waterfalls have presented the NDF field around 0.90 as a resonance zone. The deformed configuration in Fig. 81(g) confirms that the model is capable to capture the most relevant system responses in terms of acceleration giving robustness to the modelling procedure implemented for the FE approach.

Aside from the response in terms of acceleration, it is worth considering the nodal velocities on the cover external surface. The purpose of the presentation of such numerical results is due to the direct connection between the surface velocity and the radiated sound power. To evaluate the effect of the improving solution designed within the activity, the comparison of the nodal velocities of the cover allows to qualitative obtain a straightforward and fast indicator of the potential sound power emission implications. The results of the baseline configuration in terms of nodal velocities are reported within Figure 82. The results are coherent with the acceleration scheme observed in Fig. 81 and are also representative of the most emissive frequencies observed from the SPL experimental data.

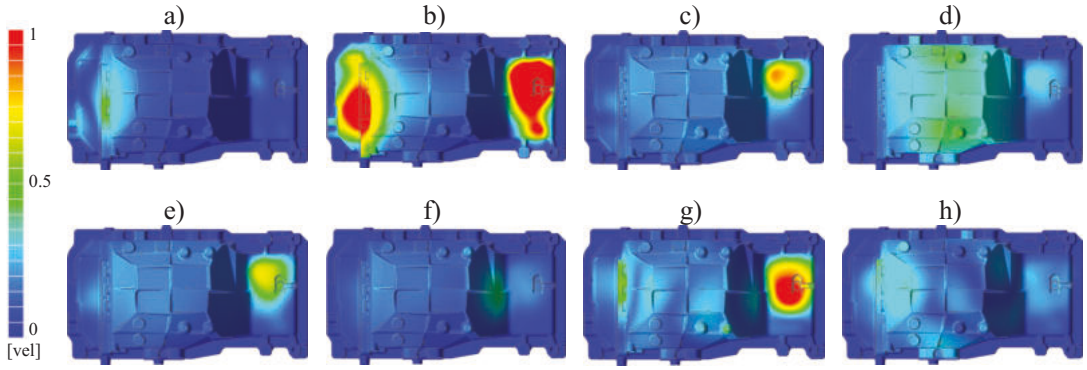

Figure 82: Frequency response analysis results in terms of nodal velocities at NDF of 0.08 (a), 0.20 (b), 0.25 (c), 0.31 (d), 0.35 (e), 0.51 (f), 0.65 (g) and 0.88 (h)

4.5 A STUDY ON NVH IMPROVEMENT SOLUTIONS

The analysis of the experimental results carried out on the baseline layout of the hydrostatic module, has revealed that the excitations coming from the mechanical transmission and from the hydrostat are transferred to the cover without consistent filtration from the HM connections. Moreover, the natural frequencies of the cover have been often excited emphasizing the radiated sound power and the vibrational level. The comparison of the baseline results with the results of an unsuccessful improvement solution has then revealed that the strategy to isolate the HM from the cover by means of cylindrical dampers does not produce the curtailment of the excitation. Since the elastic dampers are placed in series with stiffer connections, e.g. the spline joints between HM and side gears, the dampers stiffness and damping action will be neglected resulting useless for the reduction of the dynamic effects transmissibility.

The frequency response analysis performed on the FE model implemented to reproduce the baseline behaviour has shown a good coherency in the replication of the most excited frequency bands. The results has then allowed to evaluate the shape of the deformations and the most involved areas of the structure. In this context, the flat cover zone where the outlet flange is connected has shown local deformations for a wide part of the excitation frequencies. Similarly, the results have highlighted the frequent involvement of both flanges in the most excited configuration. Since for the flanges have been observed that the deformations present the rigid displacement of such

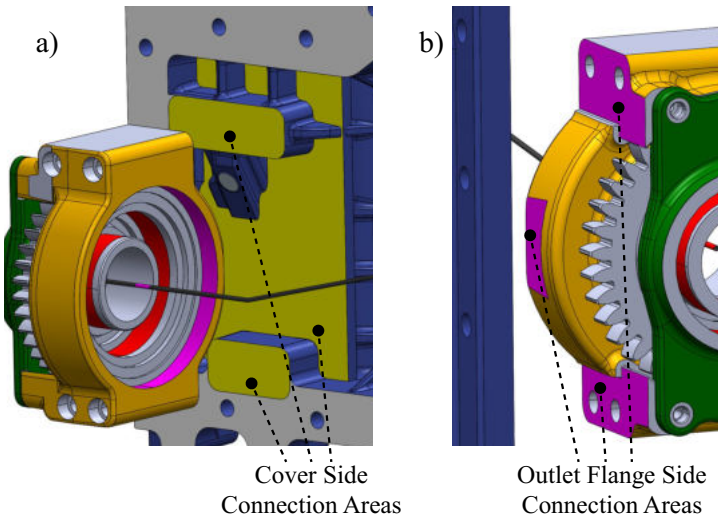

Figure 83: Cover and output flange surfaces involved into design upgrade

components, the main responsible of the modes may be the connections instead of the components themselves.

The integrated analysis of the mechanical system, of the previous improvement solution and of the combined experimental and numerical results, leads to elaborate different strategies for the implementation of novel improvement solutions. For sake of clarity, it is worth underlining that the current activities has been performed within the earliest stage of the improvement project. In this context, the enhancement solutions have been implemented adopting a straightforward but robust approach. In first instance, the improvement of the flanges connections have been taken into consideration. Then, the focus has been oriented on the analysis of the spline joints. Finally, the adoption of a different suspension strategy has been proposed. To present the evaluate the impact of the proposed enhancement, the upstream and downstream spectrum have been calculated on a frequency response analysis and lately compared with the baseline results. The reduction of the transmitted excitation on the cover side plays a crucial role for the improvement of the acoustic behaviour of the system. In parallel, the comparison has been extended to the nodal velocities on the cover side.

With the purpose to reduce the cover deformation that causes the output flange bending in several structural modes, the first improvement solution,

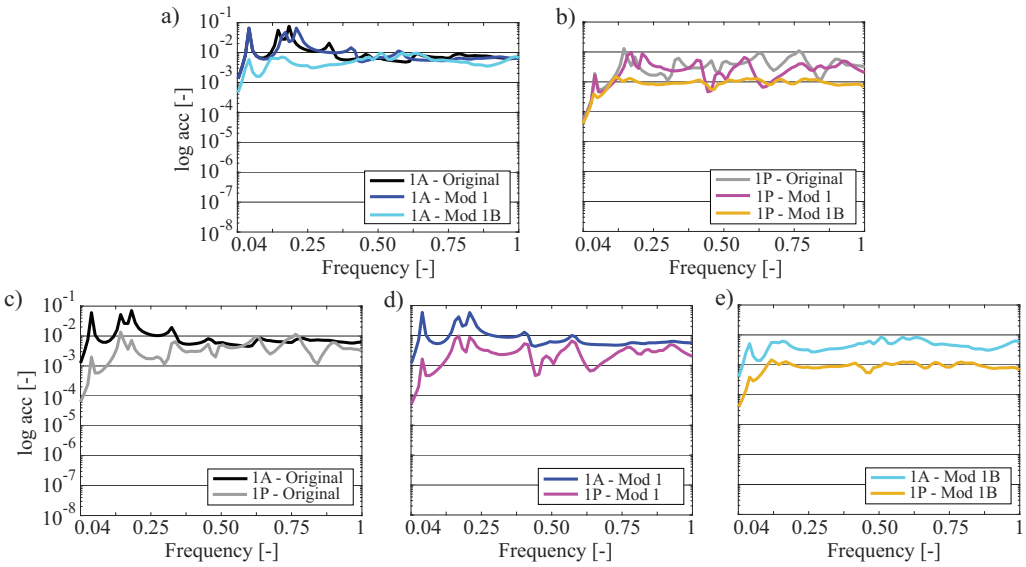

Figure 84: Input side: comparison between numerical upstream response spectrum (a) and downstream response spectrum (b). Upstream-downstream comparison in original layout (c), improved output flange connection *Mod1*(d) and improved joints *Mod1B*(e)

hereinafter named *Mod 1*, deals with the increment of the connection stiffness. The computational approach to evaluate the impact of such modification involves the increment of the connecting surface. Figure 19 shows the target surfaces subjected to the novel connection mode. On the cover side, the yellow surfaces of Fig. 83(a) have been connected by means of 1D rigid connectors to the purple surfaces on the flange side (Fig. 83(b)). It represents a fast approach to assess the modification. The Frequency analysis has been repeated on the novel configuration introducing a triaxial load on the HM concentrated mass and a sweep sine excitation with 1.25% of frequency increment step. The downstream-upstream comparison of the novel layout are reported within Fig. 84 for the inlet side accelerometers, while the responses of the outlet side are reported in Fig. 85.

Before the analysis of the results, it is worth mentioning that a second step of enhancement has been implemented within this configuration. In particular, the layout denoted as *Mod 1B* involves the introduction of a dampers on the steel joints located between HM shafts and the input and output gears. The purpose of such joint modification is to strongly reduce the transmission of

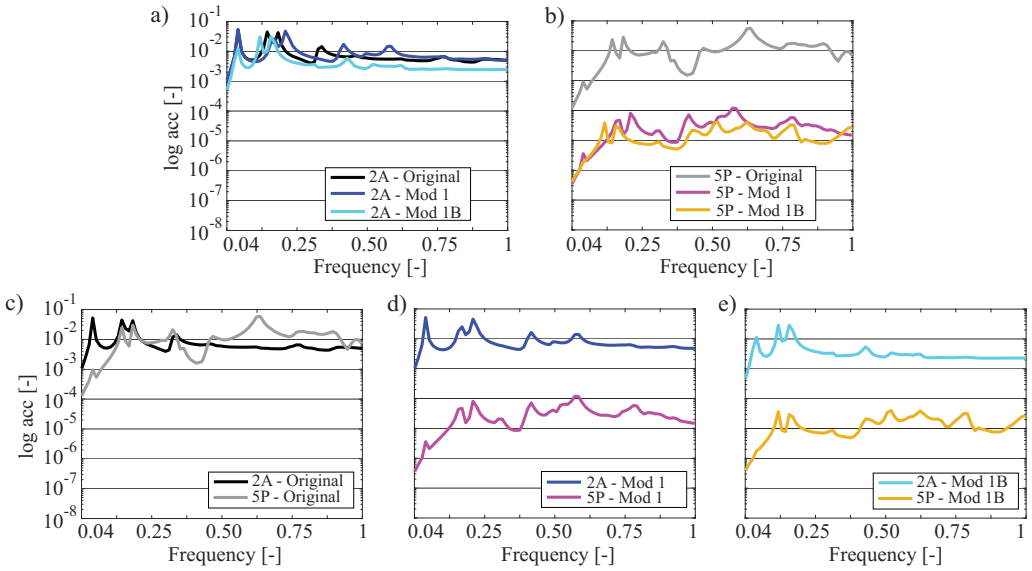

Figure 85: Output side: comparison between numerical upstream response spectrum (a) and downstream response spectrum (b). Upstream-downstream comparison in original layout (c), improved output flange connection *Mod1*(d) and improved joints *Mod1B*(e)

the meshing excitation components to the hydrostat and contextually contain the transmission of the piston pump and motor excitation to the cover. The modification has been introduced within the FE model by means of a different 1D connection between the HM *Z-beam* and the input and output gears. The spring element has been characterized with the same stiffness of the steel joint, including otherwise a proper value of viscous damping calculated on the basis of typical dampers materials involved in such applications. Also the results of this configuration are included within Figures 84 and 85.

Figures 84(a) and 85(a) show the comparison between the response calculated on the inlet and outlet side of the HM respectively. It is worth underline that, contrarily to the validation procedure, for the comparison of the different layouts a singular frequency response curve calculated as sum of the three components has been considered. On the inlet side of the HM the increment of the outlet flange connection stiffness has not revealed sensible benefits. On the contrary, the contextual introduction of the novel joint connections helps to contain the HM excitation in the $0.04 - 0.34$ NDF band. On the outlet side the three configurations presents extremely slight differences. The acceleration

calculated on the hydrostatic module remains on the same path of the original layout since the mass of the hydrostat already performs the damping action of the body connected to the rest of the structure. The increment of the flange connection stiffness does not impact on the HM displacement and acceleration while slight damping action is visible. Otherwise, the enhancements are absolutely noticeable on the cover side. The comparison of the cover responses on the input side has been presented within Fig. 84(b). The *Mod 1* layout follows the original behaviour, reducing the response amplitude among the $0.50 - 0.75$ NDF band. More appreciable is the beneficial impact of the introduction of the dampers on the HM connection with the gears. The response spectrum in *Mod 1B* layout appears extremely smooth and shows an important amplitude reduction. A massive result has been observed on the output side of the HM where the local deformations of the cover have been detected and where the flange has suffered bending response modes for several excitation frequencies. Figure 85(b) highlights how the increment of the stiffness of the flange connection is capable to curtail the cover response. The magnitude of the response acceleration level has been subjected to a reduction of two dimensional orders. Furthermore, the peak observed around the 0.63 NDF has been strongly contained. In this context, the impact of *Mod 1B* is not comparable with the *Mod 1* but it concurs in a further reduction of the components amplitude. The comparison of the upstream-downstream responses for the three configurations here described has been reported on Figures 84(c)-(e) for the input side of the HM and on Figures 85(c)-(e) for the outlet side. From the pictures clearly descends that the improved layouts are capable to strongly cut down the transmission of the excitations coming from the HM. The enhancement is particularly focused on the output side where the flange connection has been directly updated.

Aside from the acceleration point of view, the nodal velocities calculated for the *Mod 1* and *Mod 1B* layouts are reported within Figures 86 and 87. The improvement even in these terms is substantial comparing the pictures with the original layout of Fig. 82. From the velocities contour plot of Fig. 86(b)-(c) arises that the connection improvement is capable to cut down the nodal velocities on the output side. Furthermore, the contour plot of Fig. 86(c) is substantially different from the one observed at similar frequency on the original layout. Among the hazardous frequency band, in terms of perceived noise emission, the improved layout presents considerable reduction of nodal velocities magnitude, suggesting a resultant enhancement of the acoustic

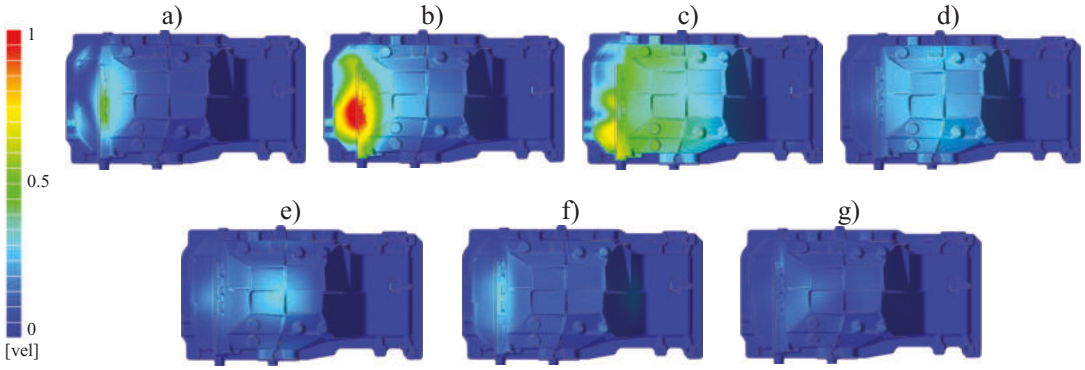

Figure 86: Frequency response analysis results in terms of nodal velocities on the *Mod1* configuration at NDF of 0.08 (a), 0.20 (b), 0.24 (c), 0.33 (d), 0.44 (e), 0.59 (f), and 0.78 (g)

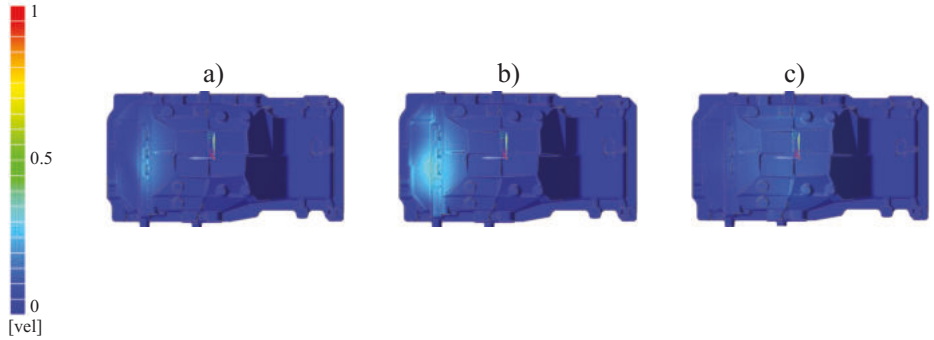

Figure 87: Frequency response analysis results in terms of nodal velocities on the *Mod1B* configuration at NDF of 0.08 (a), 0.16 (b) and 0.32 (c)

behaviour. In this context, the implementation of the *Mod 1B* layout emphasize the improvement. The cover maps reported in Fig. 87 are the responses to the 0.08, 0.20, 0.31 forcing NDF. As can be appreciate the cover excitation has been strongly curtailed. With same scale of Fig. 82, higher excitation frequencies have produced velocities responses slightly appreciable with same proposed scale and for this reason, have been omitted from the figure.

A different approach has been implemented for the configuration named *Mod 2*. Here, the connection layout between hydrostat and flanges has been kept in the original layout. Then, the HM and flanges system has been suspended on the cover by means of cylindrical dampers applied between cover and

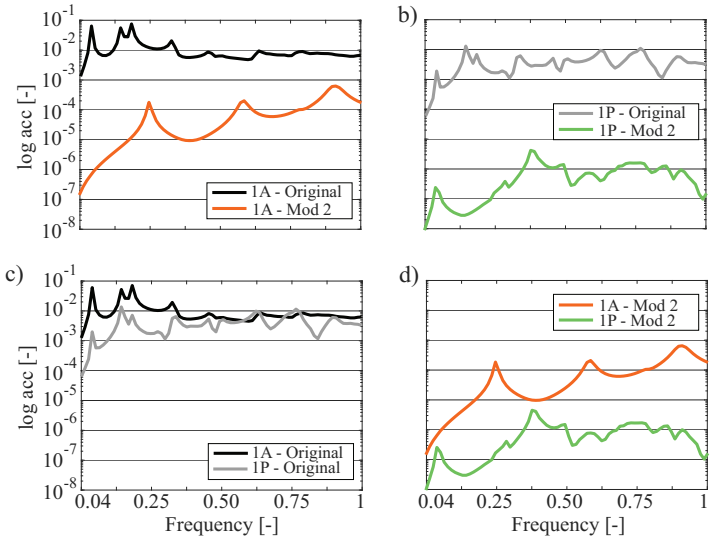

Figure 88: Input side: comparison between numerical upstream response spectrum (a) and downstream response spectrum (b). Upstream-downstream comparison in original layout (c) and improved layout *Mod2*(d)

flanges. The purpose of the modification is to isolate the cover from the HM excitation sources. The modification has been implemented within the FE model connecting cover and flanges surfaces, in contact in the original bolted connection, with four elastic connectors characterized by stiffness and viscous damping of commercial dampers. As well as for the previous solutions, the impact of the improvement solution has been evaluated by means of a frequency analysis. The first comparison has been performed on the basis of the upstream-downstream spectrum which are included within Figures 88 and 89. In this context, since the constraint to the HM and flange system has been strongly decrease and a viscous damping contribute has been included, the resultant response frequency calculated on the HM presents a considerably lower amplitude with respect to the baseline configuration. The reduction is appreciable on both input and output side of the HM as shown by Fig. 88(a) and Fig. 89(a) respectively. As a matter of fact, such consistent curtailment of the excitation indisputably produce a reduction of the cover response. Furthermore, the damping action of properly tailored elements between cover and flanges contributes to the isolation of the cover. The combined effect is visible from the comparison of the downstream spectrum of Figures 88(b) and

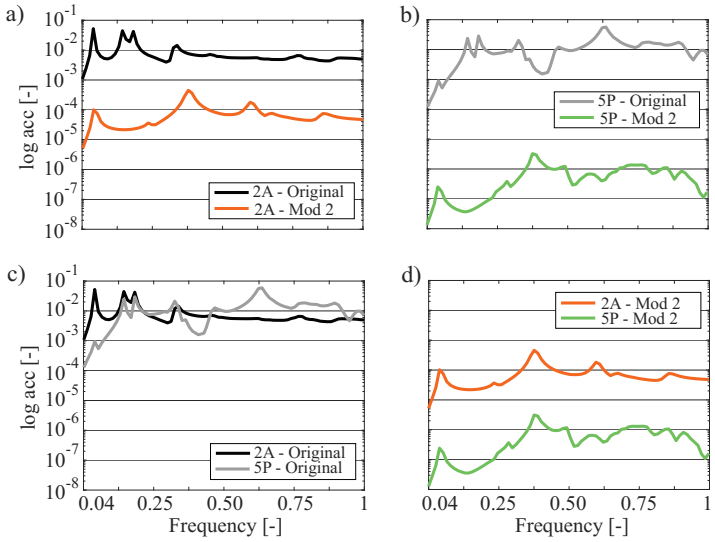

Figure 89: Output side: comparison between numerical upstream response spectrum (a) and downstream response spectrum (b). Upstream-downstream comparison in original layout (c) and improved layout *Mod2*(d)

Fig. 89(b). As predicted the result of the enhancement solution is the reduction of the response acceleration level of four magnitude orders. The final *Mod 2* upstream-downstream comparison is given within Fig. 88(d) and Fig. 89(d) and allows to appreciate the strong isolation of the HM excitations. Thus, for this configuration the comparison in terms of nodal surface velocities has not been included since the contours with equal scale does not capture differences.

For sake of completeness, it is worth clarify that other enhancement strategies have been followed and implemented within the proposed study giving unsatisfactory results. In first instance, following the *Mod 1* strategy, the increment of the input flange connection with the cover has been implemented in addition to the output flange improvement. The results have not revealed particular enhancement in terms of acceleration level and nodal velocities and have been discarded. A completely different approach has been implemented increasing the stiffness of the connections between HM and flanges simulating the introduction of rigid steel mounts on both sides. In such way, the localized deformation of the cover that cause the bending of the flanges involves the whole structure of HM and flanges emphasizing the magnitude of the cover

displacements. It results into an increment of the cover response amplitude in terms of acceleration and velocities.

4.6 CONCLUDING REMARKS

This Chapter has presented a study devoted to the improvement of the vibroacoustic behaviour of an agricultural CVT transmission. In particular, the study has been focused on the hydrostatic module of the transmission which is directly connected to a cover and to the input and output gears that take the power from the engine shaft. The enhancement project has been carried out evaluating the effect of several improvement layouts on the vibrational response of the structure. For the purpose, a validated FE model has been implemented and described within previous sections. The validation procedure has been based on the reproduction of salient aspects observed during a dedicated test campaign. In this context, the transmission has been subjected to a run-up analysis and its vibrational behaviour characterized by means of seven accelerometers mounted both on the HM and on the cover. Furthermore, the radiated noise has been monitored by means of a prepolarized microphone positioned outside the cover.

With the purpose to identify the main excitation sources of the system, the initial part of the activity has been devoted to the processing of the experimental data and to the consequent analysis. The study of the accelerometer waterfall has shown several resonance band excited for the entire run-up test. Furthermore, the coupled analysis of the microphone waterfalls has highlighted how certain resonances are either emphasized in terms of radiated sound power. In addition, the waterfall diagrams have revealed that the most relevant excitations are the harmonic orders of the hydrostatic module pumping actions. The comparison of the upstream and downstream signals has shown that the HM connections transmit the dynamic components to the cover which is often responsible of further increment of the response. Particular relevance in terms of noise and vibration has been shown by the harmonic of the meshing orders of the CVT output gear connected to the HM by means of steel joints. In this first phase the analysis of experimental data has also been carried out on data acquired on a the test campaign performed to characterized the behaviour of a unsuccessful previous improvement project. The study has been fundamental to understand that considering damping solutions, structure

stiffness improvement or layout modifications without deeply understand the connection scheme of the involved components may results into tremendous mistakes and wastes.

The FE model has been developed considering the HM as a concentrated mass characterized by its inertial properties and connected to a rigid beam. Moreover, the rigid beam has been connected to the bodies in contact with the hydrostat by means of 1D connectors. Each connector is representative of the component that connect the HM with the other bodies. The connection of the HM with the input flange has been simulated through spring elements with the stiffness of the steel mounts adopted to suspend the hydrostat. On the other hand, the elastic ring that sustain the HM on the output flange has been substituted by a spring element with a characteristic viscous damping factor. Then, the steel spline joints that connect the HM with inlet and outlet gears have been included. It is worth underline that such components have been considered as the vibrational paths for the transmission of the HM characteristic components to the cover. Finally, the gears have been connected to the relative flanges by means of spring elements that simulate the bearings stiffness. For the validation procedure, a frequency response analysis has been performed loading the HM concentrated mass with a triaxial frequency dependent load with 1N of magnitude. The structure excitation has been performed by means of a sweep sine until the maximum frequency considered within the experimental analysis. The forcing frequency has been incremented from the minimum value with 1.25% steps of the maximum frequency. The stiffness of the elements that simulates bearings, joints and steel mounts has been tailored in order to meet the results of the baseline experimental campaign. The comparison between numerical and experimental results has been performed evaluating the vibrational spectrum of the three axes signals of the accelerometers, mounted on the hydrostat and on the cover. Then, the characteristic frequencies and the shape of the respective deformed configurations have been compared with the vibrational waterfall. The comparison has highlight how the model was capable to reproduce the most emphasized frequencies shown within the waterfalls and also reproduce response modes with local deformations near the accelerometers that have revealed the resonance band.

The validated FE model has been adopted to implement schematic solutions to reduce the noise emission of the structure. As a matter of fact, since the study represents one of the earliest stages of the project, the design of specific parts

for the sensitivity analysis to the modification may represents a useless waste of time and resources. The proposed improved layouts represent the guideline for the designer to the definition of the executive parts and components. In first instance, an increment of the stiffness and of the surface of the connection between cover and output flange has been proposed. The purpose of the solution has been the reduction of the flange bending actions that involve the cover in a zone where it presents weakness and a poor attitude to the noise containment. The frequency analysis has shown a strong improvement on the curtailment of the vibration transmitted from the HM to the cover. Since the model has not been subjected to boundary element modelling to numerically calculate the sound power emission, a fast and straightforward method adopted to evaluate the effect on the noise emission has been the comparison of the cover nodal velocities contour plots. In this context, the novel layout is capable to cut-down the nodal velocity amplitude, especially on the critical surface of the cover on the output side. Then, on the same layout, with the purpose to isolate the input and output gears from the HM, a viscous damping components has been added on the previously equipped steel spline joints. The modification has been implemented simulating the introduction of dampers on these components to avoid the transmission of the characteristic excitations. The analysis has highlight the beneficial effect of the dampers in terms of excitation containment and consequently in terms of cover response. A third approach has been implemented for the study. It involves the introduction of four cylindrical dampers on the four connection surfaces between flanges and cover. In this layout, the frequency response analysis has revealed a massive impact on the curtailment of the excitations and an even more effective reduction of the cover response which has not shown appreciable excitation zones on the velocity contour plots.

As a matter of fact, all the three proposed methodology for the NVH behaviour improvement have shown extremely promising enhancement potential. However, it is clear that the design of operative solution may not be capable to obtain the results showed by the here proposed investigation. In fact, considering the *Mod 1* configuration, the design of a novel flange and cover layout that allows to integrate a consistent increment of the contact surfaces and of the connecting bolts, certainly clashes with space requirement and weight constraints. Citing the *Mod 1B* layout, it is clear that introducing a novel joint with integrated dampers may requires the design of specific tailored

joints or might needs the evaluation of commercial solutions. Even in this case the designer will be claimed to define the most effective solution in terms of NVH improvement combined to the economic effort. With same approach, the *Mod 2* layout, which presents the most fascinating solutions in terms of noise emission, requires a dedicated design activity oriented to the generation of novel flanges capable to house the cylindrical dampers. Even in this case, the space requirement constraints will have a direct influence on the solution and, even in this case, the obtainable results would be mitigate by economic and feasibility implications.

The study here presented gives the chance to appreciate the benefits correlated to the implementation of these novel investigation strategies for the characterization of the NVH behaviour of a volumetric machine. The method considers the hydrostat as a black box that excites the system where it is placed and try to elaborate improvement solutions. It is worth underline that for the purpose the fluid-dynamic behaviour of axial piston pump and motor has not been object of enhancement studies. However, the knowledge of the machine operating principles plays a crucial role into the analysis of the system excitation sources. The FE approach allows to generate a reliable and flexible twin of the system. It also allows to straightforwardly implement schematic solutions that are extremely useful to trace the admissible improvement paths avoiding the detailed design of novel components that may represents improvement strategies.

5

CONCLUDING REMARKS

The thesis here presented addresses the development of advanced techniques for the prediction of the volumetric machines behaviour. In this context, the word *behaviour* includes the performances of the pumps in terms of pressure and flowrate and also the NVH aspects related to the pump operative principles. The proposed methodologies are indisputably oriented to the enhancement of the design phase of these machines, suggesting the necessity to integrate dedicated study to prevent costly unsatisfactory results.

In particular, within the second Chapter a design optimization strategy has been proposed for the design of a specific family of balanced vane pump. The basis of the proposed methodology relies on the deep investigation of the vane-cam ring kinematic. Here, the kinematic of the mechanism has been analytically described bounding the vane lift law with its main geometrical features. Following this strategy, has been possible to extrapolate the explicit formulation of the geometrical acceptance limits imposing the kinematic admissibility constraints to the vane lift law. In this context, since the vanes non eligible of coherent motion result discarded from the admissibility domain, the methodology allows to prevent the adoption of vanes that are not capable to ensure a smooth and continuous motion. A further step to the investigation has been given through the analysis of the forces acting on the vane generated by the centrifugal and inertial actions. Such analysis has allowed to formalize the criteria for the discarding of the vanes that are reasonably hazardous in terms of contact load generation. In fact, while high contact forces are responsible of wear phenomena and high dynamic actions, overly low forces potentially cause contact detachment with consequent lubricant leakages and vibrations. In second hence, a similar analysis focussed on the implications related to

the introduction of pre-compressive cam ring has been included within the Chapter. The implementation of the analytical procedure on a dedicated case study has shown the potential of the method through the development of the vane geometry admissibility maps that acts as a extremely relevant tool for the early stages of the design of novel vane pumps. The research has highlight the relevance of the deep investigation of the kinematic principles of these pumps that are often considered as straightforward machines. It is worth underlining that only through a dedicated study the hazardous implications related to the duality of the contact point that affect such family of vanes are resolvable. Moreover, the analysis has highlighted that introducing simple modification of the cam ring profile to improve the pump pressurization may results into lack of motion regularity, resulting into NVH issues and on the other hand unexpected leakages.

Within Chapter 3 a lumped parameters approach has been applied to the developement of volumetric machines performance enhancement strategies. Even if such investigation methodology might be deployed for the whole population of volumetric machines, within this work the study of external gear pumps has been proposed and discussed. The model has been developed introducing the characterization of the continuity equations, that rule the pressure and flowrate equilibrium, by means of a novel approach. In particular, the equations have been implemented following the Bernoulli's formulation for the flowrate calculation without imposing *a priori* the flow regime. The switch from laminar to turbulent regime has been ensured by means of the punctual calculation of the flow parameters in each resolution angle step. Thus, it allows the model to autonomously impose the flow characteristics also ensuring the transition between the possible regimes. With the purpose to increase the reliability of the calculation, the flow parameters have been properly tailored by means of a meticulous validation procedure detailed in Chapter 3. Furthermore, within the chapter has been highlighted the relevance of the novel orifices area estimation methodology. The passage areas and the vain control volumes have been calculated for each angular step by means of a 2D triangulation mesh. Such approach has allowed to drastically reduce the numerical spikes on the results, often noticeable among these models, that are mostly originated from discontinuities on the orifices estimation. The analysis of a set of experimental results has also suggested the implementation of a shaft bending calculation methodology in each angular step. It has allowed to improve the estimation of

the clearances between gears and housing and consequently of the flowrates here exchanged. The reliability of the model and its sensibility has been assessed from a dedicated validation procedure oriented to the reproduction of the performances of a tested pump. Then, the model has been deployed for the evaluation of the effects of design improvements within a helix gear pump performance enhancement project. Several balancing plates design have been numerically tested with the purpose to identify the most effective in terms of performance improvement. In this context, the extremely accurate post processing tool has allowed to identify a design issue that was affecting the pump generating uncontrolled leakages and a strong efficiency drop in certain condition. The structure of the model has allowed to elaborate and simulate a wide spectrum of solutions to overcome the observed phenomena, avoiding a massive computational effort. The extension of the pressure arc on the suction side of the pump has shown a successfully pressurization enhancement followed by a strong reduction of the return leakages from the pressurized vain to the inlet chamber. Major sensibility to the improvement effect has been observed on the low delivery pressure conditions that were the most affected in terms of volumetric efficiency curtailment. Furthermore, the design of balancing plate grooves shifted on the suction side has shown additional beneficial effects. The shape of the grooves, their dimensions and the timing of the isolation and release of the vain to vain entrapped oil on the meshing zone have been deeply investigated in terms of overall performances and in terms of local flowrtates and phenomena. The most effective solutions have been presented within the chapter and successively implemented by the company that has required the study. Finally, the novel pump layout has been implemented and tested. The results have highlighted the absolute reliability of the tool for the reproduction of the internal phenomena and for the estimation of the efficiency improvement. As a result, the two tested sample pumps have presented a mean 3The possibility to dispose of a flexible and reliable numerical tool similar to the one here proposed, represents indeed an extremely useful ally for the designer. Aside from the representation of the changes derived from macroscopic modifications, *e.g.* balancing plate layout, the model has allowed to finely evaluate also the influence of clearances and slight geometrical variations. As a matter of fact, the integration of these calculations within the early stages of the design may help to avoid time and material waste of the common try and error approaches of the testing phases.

The final Chapter of the thesis has been dedicated to the description of an investigation technique oriented to the evaluation of the NVH behaviour of the volumetric machines. The integration of these machines within the final systems often reveals the necessity to improve the connection path and the casing layout. For the scope of this thesis, the integration of a hydrostatic module within an agricultural CVT has been investigated by means of the implementation of a FE modelling. The model has been validated reproducing the vibrational excitations and the responses measured from an initial operative NVH characterization, by means of a numerical frequency response analysis. The study has been included with the purpose to present the relevance of these advanced techniques even in the early stages of the design of novel projects and not only for the design of enhancement strategy. The knowledge of the operating principles of the piston pump and motor that constitute the HM has represented a crucial aspect for the evaluation of the noise and vibration sources characterized by the operative measurements. Moreover, it has allowed to approach the system modelling following the strategy illustrated in Chapter 4. The HM has been modelled as a non-deformable beam connected with the surrounding components by means of spring elements reproducing the connection stiffness. Steel mount, joints and dampers have been modelled in such way, while, with the purpose to evaluate the deformations and the natural frequencies, cover, flanges and gears have been modelled with 3D finite elements. The concentrated element stiffness has been tailored within the validation procedure. A response analysis has been performed through the introduction of a triaxial sweep sine excitation, with constant amplitude and increasing forcing frequency among the range observed from the operative analysis. The comparison has been performed considering the resonance bands observed by the accelerometers located on the system during the operative characterization and the shape of the numerical contour plot. The correspondence between the local deformation at specific forcing frequencies and the results of the accelerometers has allowed to assessed the FE model validation. Thus, the validated model has been adopted for the evaluation of straightforward enhancement solutions. The analysis of the results has been performed through the comparison of the baseline vibration spectrum with the updated layout responses. Three main modifications have been proposed and numerically evaluated. In particular, the increment of the stiffness of the cover connection in a zone affected by several local emissive modes has shown

the most relevant improvement. Then, a damper has been included between the input and output HM shafts and the relative gears. Such modification has highlighted a the importance to contain the HM excitation transmission toward the cover. In parallel, despite the model has not been structured to directly evaluate the impact of the update in this terms, it has also been oriented to the containment of the excitations arising from the gears meshing and transmitted to the HM and then to the cover. A third approach which relies on the introduction of dampers between cover and supporting flanges has been proposed. In this context, the results have shown a strong improvement in terms of curtailment of the excitations toward the cover. It is worth underlining that even the first two solutions are quite easily implementable, the third requires a major effort and impact on the system design. Since nowadays the CVT systems are extremely widespread and the necessity to control and improve the NVH behaviour of all the components involved within the system, this work has highlighted the necessity to dispose of a reliable tool that allows to evaluate the consistency of the whole system design. The FE approach here proposed gives the chance to contain the computational efforts reducing the number of meshed components keeping the accuracy of the results. Finally, it gives the chance to implement in an extremely straightforward way a great variety of design improvement solutions and evaluate the impact on the overall NVH behaviour. In this context it is possible to discard the less improving updates focusing on the detailed design phase only for the eligible solutions.

Concluding the Chapter, it is worth underlining that despite the methodologies here presented concern apparently different topics, the deep investigation of the phenomena has shown how it is possible to correlate all these aspects. Moreover, the integration of these novel tools within the early stages of the design may represent a crucial aspect for the design of brand new products curtailing the costs related to the trial and error approaches within the testing phases. Considering for example the study of the balanced vane pumps kinematic, it is indisputably fundamental to understand the dynamic sources that such machines may generate. In this context, the development of a FE model of the pump and of the system where the pump would be integrated, may help the designer to design the structures to avoid resonances around the pump characteristic harmonics. Furthermore, as shown, the development of robust LP numerical tools guide the definition of the best solutions in terms of volumetric efficiency with reliability and contained computational effort.

Undoubtedly, this novel comprehensive advanced approach would be implemented not only for balanced vane pumps but also for the entire category of volumetric pumps and the systems where may be located.

BIBLIOGRAPHY

[1] Davide Guerra, Marco Polastri, Mattia Battarra, Alessio Suman, Emiliano Mucchi, and Michele Pinelli. "A design procedure for multistage external gear pumps." In: *BATH/ASME 2020 Symposium on Fluid Power and Motion Control, FPMC 2020* (2020), pp. 1–10. DOI: 10.1115/FPMC2020-2797.

[2] Davide Guerra, Marco Polastri, Mattia Battarra, Alessio Suman, Emiliano Mucchi, and Michele Pinelli. "Design Multistage External Gear Pumps for Dry Sump Systems: Methodology and Application." In: 2021.March (2021). ISSN: 15635147. DOI: 10.1155/2021/8888128.

[3] Davide Guerra, Mattia Battarra, and Emiliano Mucchi. "Kinematics and geometrical admissibility conditions of balanced vane pumps with twin lip vanes." In: *Mechanism and Machine Theory* 167.August 2021 (2022). ISSN: 0094114X. DOI: 10.1016/j.mechmachtheory.2021.104534. URL: https://doi.org/10.1016/j.mechmachtheory.2021.104534.

[4] Davide Guerra, Mattia Battarra, Emiliano Mucchi, and Giorgio Dalpiaz. "Balanced Twin Lip Vane Pumps: A Kinematic Approach to the Design." In: (2022), pp. 69–76. DOI: 10.1007/978-3-031-10776-4_9.

[5] Heiko Neukirchner, Mathias Kramer, and Tilo Ohnesorge. "The controlled vane-type oil pump for oil supply on demand for passenger car engines." In: *SAE Technical Papers* 724 (2002). ISSN: 26883627. DOI: 10.4271/2002-01-1319.

[6] Eiichi Kojima, Masaaki Shinada, and Toshio Yoshino. "Characteristics of fluidborne Noise Genersted by fluid power pump." In: *Bulletin of JSME* 27.225 (1984), pp. 475 –482. ISSN: 13476947. DOI: 10.1299/jsme1958.27.475.

[7] G. G.L. Seet, J. E.T. Penny, and K. Foster. "Applications of a computer model in the design and development of a quiet vane pump." In: *Proc. Inst. Mech. Eng. Part B* 199.4 (1985), pp. 247–253. ISSN: 20411975. DOI: 10.1243/PIME_PROC_1985_199_076_02.

[8] Katsuhiko Hattori, Hideyuki Suzuki, and Junzo Hasegawa. "Design method of small-ripple vane pump." In: *SAE Technical Papers* (1987). ISSN: 26883627. DOI: 10.4271/871681.

[9] Keiichi Nakamura, Akira Hibi, Hideki Yanada, and Yasutoshi Hattori. "Pressure Ripples of a Balanced Vane Pump." In: *Trans. Jpn. Soc. Mech. Eng. Series B* 58.547 (1992), pp. 799–803. ISSN: 03875016. DOI: 10.1299/kikaib.58.799.

[10] Yoshiharu Inaguma and Keiichi Nakamura. "Influence of leakage flow variation on delivery pressure ripple in a vane pump." In: *Proc. Inst. Mech. Eng., Part C* 228.2 (2014), pp. 342–357. ISSN: 09544062. DOI: 10.1177/0954406213484669.

[11] Allan L. Dickinson, Kevin A. Edge, and D. Nigel Johnston. "Measurement and prediction of power steering vane pump fluidborne noise." In: *SAE Technical Papers* (1993). ISSN: 26883627. DOI: 10.4271/931294.

[12] B. L. Jones, D. N. Johnston, and D. K. Longmore. "Simulation of suction flow ripple in power steering pumps." In: *SAE Technical Papers* 724 (1998). ISSN: 26883627. DOI: 10.4271/982023.

[13] E. Mucchi, G. Cremonini, S. Delvecchio, and G. Dalpiaz. "On the pressure ripple measurement in variable displacement vane pumps." In: *Journal of Fluids Engineering, Transactions of the ASME* 135.9 (2013), pp. 1–11. ISSN: 00982202. DOI: 10.1115/1.4024110.

[14] Thomas Lobsinger, Timm Hieronymus, and Gunther Brenner. "A CFD Investigation of a 2D Balanced Vane Pump Focusing on Leakage Flows and Multiphase Flow Characteristics." In: *Energies* 13.13 (2020), pp. 1–24. ISSN: 19961073. DOI: 10.3390/en13133314.

[15] Timm Hieronymus, Thomas Lobsinger, and Gunther Brenner. "A combined CFD-FEM approach to predict fluid-borne vibrations and noise radiation of a rotary vane pump." In: *Energies* 14.7 (2021). ISSN: 19961073. DOI: 10.3390/en14071874.

[16] J. J Watton and K. L. K L Watkins-Franklin. "The Transient Pressure Characteristic of a Positive Displacement Vane Pump." In: *Proc. Inst. Mech. Eng., Part A* 204.4 (1990), pp. 269–275. ISSN: 20412967. DOI: 10.1243/PIME_PROC_1990_204_036_02.

[17] Takao NISHIUMI and Teruyuki MAEDA. "Motion of the Vane in a Variable Displacement Vane Pump. 1st Report: On the Vane Jumping Phenomenon in the Process of Compression." In: *Hydraulics and Pneumatics* 24.2 (1993), pp. 261–268. ISSN: 0286-6900. DOI: 10.5739/jfps1970.24.261.

[18] Myung Rae Cho and Dong Chul Han. "Vane tip detachment in a positive displacement vane pump." In: *KSME International Journal* 12.5 (1998), pp. 881–887. ISSN: 12264865. DOI: 10.1007/BF02945555.

[19] R. Gellrich, A. Kunz, G. Beckmann, and E. Broszeit. "Theoretical and practical aspects of the wear of vane pumps Part A. Adaptation of a model for predictive wear calculation." In: *Wear* 181-183.PART 2 (1995), pp. 862–867. ISSN: 00431648. DOI: 10.1016/0043-1648(95)90208-2.

[20] A. Kunz, R. Gellrich, G. Beckmann, and E. Broszeit. "Theoretical and practical aspects of the wear of vane pumps Part B. Analysis of wear behaviour in the vickers vane pump test." In: *Wear* 181-183.PART 2 (1995), pp. 868–875. ISSN: 00431648. DOI: 10.1016/0043-1648(95)90209-0.

[21] J. Ivantysyn and M. Ivantysynova. *Hydrostatic Pumps and Motors Principles, Design, Performance, Modeling, Analysis, Control and Testing*. New Delhi - India: Tech Book International, 2003.

[22] Y. Inaguma and A. Hibi. "Vane pump theory for mechanical efficiency." In: *Proc. Inst. Mech. Eng. Part C* 219.11 (2005), pp. 1269–1278. ISSN: 09544062. DOI: 10.1243/095440605X32002.

[23] Yoshiharu Inaguma and A. Hibi. "Reduction of friction torque in vane pump by smoothing cam ring surface." In: *Proc. Inst. Mech. Eng. Part C* 221.5 (2007), pp. 527–534. ISSN: 09544062. DOI: 10.1243/0954406JMES225.

[24] Yoshiharu Inaguma and Naohito Yoshida. "Variation in driving torque and vane friction torque in a balanced vane pump." In: *SAE Technical Papers* 1 (2014). ISSN: 26883627. DOI: 10.4271/2014-01-1764.

[25] Shaonian Li, Hao Liu, Yi Li, Shangling Bao, and Pan Yang. "Tribological behavior of friction pairs in a high-pressure vane pump under variable working conditions." In: *Tribology Online* 16.3 (2021), pp. 159–169. ISSN: 18812198. DOI: 10.2474/TROL.16.159.

[26] Feng Wang, Zhenxing Sun, Wieslaw Fiebig, Bing Xu, and Kim A. Stelson. "Lubrication and fluid film study on the vane tip in a vane pump hydraulic transmission considering a fluid and structure interaction." In: *Journal of Tribology* 143.12 (2021), pp. 1–14. ISSN: 15288897. DOI: 10.1115/1.4050350.

[27] Antonio Giuffrida and Rosario Lanzafame. "Cam shape and theoretical flow rate in balanced vane pumps." In: *Mechanism and Machine Theory* 40.3 (2005), pp. 353–369. ISSN: 0094114X. DOI: 10.1016/j.mechmachtheory.2004.07.008.

[28] Mattia Battarra, Alessandro Blum, and Emiliano Mucchi. "Kinematics of a balanced vane pump with circular tip vanes." In: *Mechanism and Machine Theory* 137 (2019), pp. 355–373. ISSN: 0094114X. DOI: 10.1016/j.mechmachtheory.2019.03.034.

[29] Mattia Battarra and Emiliano Mucchi. "On the relation between vane geometry and theoretical flow ripple in balanced vane pumps." In: *Mechanism and Machine Theory* 146 (2020). ISSN: 0094114X. DOI: 10.1016/j.mechmachtheory.2019.103736.

[30] Mattia Battarra and Emiliano Mucchi. "Analytical determination of the vane radial loads in balanced vane pumps." In: *Mechanism and Machine Theory* 154 (2020). ISSN: 0094114X. DOI: 10.1016/j.mechmachtheory.2020.104037.

[31] Robert L. Norton. *Cam design and manufacturing handbook*. Second. 2009, p. 608.

[32] A.J. Robison and A. Vacca. "Performance comparison of epitrochoidal, hypotrochoidal, and cycloidal gerotor gear profiles." In: *Mechanism and Machine Theory* 158 (2021).

[33] K Foster, R Taylor, and I M Bidhendi. "Computer Prediction of Cyclic Excitation Sources for an External Gear Pump." In: *Proceedings of the Institution of Mechanical Engineers, Part B: Management and engineering manufacture* 199.3 (1985), pp. 175–180. DOI: 10.1243/PIME_PROC_1985_199_064_02.

[34] S Mancò and N Nervegna. "Modello Matematico di Pompe Oleodinamiche a ingranaggi esterni." In: *Atti* 8 (1987), pp. 353–360.

[35] S. Manco' and N. Nervegna. "Simulation of an External Gear Pump and Experimental Verification." In: *Proc. JFPS Int. Symp. on Fluid Power* 1989.1 (1989), pp. 147–160. DOI: 10.5739/isfp.1989.147.

[36] S Mancò and N Nervegna. "Pressure transients in an external gear hydraulic pump." In: *Proceedings of the JFPS International Symposium on Fluid Power*. Vol. 1993. 2. The Japan Fluid Power System Society. 1993, pp. 221–227.

[37] C. Bonacini and M. Borghi. "Calculation of the pressures on the teeth of an external gear hydrodynamic machine; [Calcolo delle pressioni nei vani fra i denti di una macchina oleodinamica ad ingranaggi esterni]." In: *OLEODINAMICA-PNEUMATICA* 31.11 Nov. (1990), 128 – 134.

[38] Massimo Borghi, Massimo Milani, F Paltrinieri, and Marco Guidetti. "Influenza del rodaggio sulle condizioni di funzionamento di macchine volumetriche ad ingranaggi esterni." In: *56° Congresso Nazionale ATI* Figura 1 (1997), pp. 1–11.

[39] M. Borghi, M. Milani, F. Paltrinieri, and B. Zardin. "Pressure transients in external gear pumps and motors meshing volumes." In: *SAE Technical Papers* 724 (2005). ISSN: 26883627. DOI: 10.4271/2005-01-3619.

[40] M. Borghi, M. Milani, F. Paltrinieri, and B. Zardin. "Studying the axial balance of external gear pumps." In: *SAE Technical Papers* (2005). ISSN: 26883627. DOI: 10.4271/2005-01-3634.

[41] E. Mucchi, G. Dalpiaz, and A. Fernàndez Del Rincòn. "Elastodynamic analysis of a gear pump. Part I: Pressure distribution and gear eccentricity." In: *Mechanical Systems and Signal Processing* 24.7 (2010), pp. 2160–2179.

[42] E. Mucchi, G. Dalpiaz, and A. Rivola. "Elastodynamic analysis of a gear pump. Part II: Meshing phenomena and simulation results." In: *Mechanical Systems and Signal Processing* 24.7 (2010), pp. 2180–2197.

[43] A. Vacca and M. Guidetti. "Modelling and experimental validation of external spur gear machines for fluid power applications." In: *Simulation Modelling Practice and Theory* 19.9 (2011), pp. 2007–2031.

[44] M. Battarra and E. Mucchi. "A method for variable pressure load estimation in spur and helical gear pumps." In: *Mechanical Systems and Signal Processing* 76-77 (2016), pp. 265–282.

[45] Mattia Battarra, Emiliano Mucchi, and Giorgio Dalpiaz. "A Model for the Estimation of Pressure Ripple in Tandem Gear Pumps." In: *ASME IDETC/CIE*. Aug. 2015.

[46] Pedro J Gamez-montero and Gustavo Raush. "Method for Fluid Flow Simulation of a Gerotor Pump Using OpenFOAM." In: 139.November (2017), pp. 1–9. DOI: 10.1115/1.4037060.

[47] R. Castilla, P.J. Gamez-Montero, N. ErtÃ¼rk, A. Vernet, M. Coussirat, and E. Codina. "Numerical simulation of turbulent flow in the suction chamber of a gearpump using deforming mesh and mesh replacement." In: *International Journal of Mechanical Sciences* 52.10 (2010), pp. 1334–1342. ISSN: 0020-7403. DOI: https://doi.org/10.1016/j.ijmecsci.2010.06.009.

[48] Emma Frosina, Adolfo Senatore, and Manuel Rigosi. "Study of a high-pressure external gear pump with a computational fluid dynamic modeling approach." In: *Energies* 10.8 (2017). ISSN: 19961073. DOI: 10.3390/en10081113.

[49] Sujan Dhar and Andrea Vacca. "A novel CFD - Axial motion coupled model for the axial balance of lateral bushings in external gear machines." In: *Simulation Modelling Practice and Theory* 26 (2012), pp. 60–76. ISSN: 1569190X. DOI: 10.1016/j.simpat.2012.03.008.

[50] Emiliano Mucchi, Mattia Battarra, Alessio Suman, Michele Pinelli, and Giorgio Dalpiaz. *Combining lumped parameter modelling and CFD analysis for the pressure ripple estimation of tandem gear pumps*. Elsevier Inc., 2019, pp. 369–397. ISBN: 9780128169988. DOI: 10.1016/b978-0-12-816998-8.00013-3.

[51] B. Zardin, E. Natali, and M. Borghi. "Evaluation of the Hydro—Mechanical Efficiency of External Gear Pumps." In: *Energies* (2017).

[52] F. Rituraj, A. Vacca, and A. Morselli M. "Modeling of manufacturing errors in external gear machines and experimental validation." In: *Mechanism and Machine Theory* 140 (2019), pp. 457–478.

[53] B Zardin, F Paltrinieri, M Borghi, and M Milani. "About the prediction of pressure variation in the inter-teeth volumes of external gear pumps." In: *Proceedings of the 3rd FPNI-PhD symposium on fluid power, Spain*. 2004.

[54] M. Battarra and E. Mucchi. "On the assessment of lumped parameter models for gear pump performance prediction." In: *Simulation Modelling Practice and Theory* 99 (2020).

[55] Shuai Mo, Zongxiang Yue, Zhiyou Feng, Lijuan Shi, Zhenxing Zou, and Heyu Dang. "Analytical investigation on load-sharing characteristics for multi-power face gear split flow system." In: *Proceedings of the Institution of Mechanical Engineers, Part C: Journal of Mechanical Engineering Science* 234.2 (2020), pp. 676–692. ISSN: 20412983. DOI: 10.1177/0954406219876954.

[56] Mo Shuai, Zhang Ting, Jin Guo-guang, Cao Xiao-lin, and Gao Han-jun. "Analytical investigation on load sharing characteristics of herringbone planetary gear train with flexible support and floating sun gear." In: *Mechanism and Machine Theory* 144 (2020). ISSN: 0094114X. DOI: 10.1016/j.mechmachtheory.2019.103670.

[57] J. R. Colbourne. *The Geometry of Involute Gears*. New York, NY, USA: Springer-Verlag, 1987.

[58] Claudio Bonacini. "Sulla portata delle pompe a ingranaggi." In: 9 (1961).

[59] Claudio Bonacini. *Sulle pompe a ingranaggi a dentatura elicoidale*. 1965.

[60] W. E. Wilson. "Clearance Design in Positive Displacement Pumps." In: *Machine Design* 1.1 (Feb. 1963), pp. 127–130.

[61] Paolo Casoli, Andrea Vacca, Germano Franzoni, and Gian Luigi Berta. "Modelling of fluid properties in hydraulic positive displacement machines." In: 14 (2006), pp. 1059–1072. DOI: 10.1016/j.simpat.2006.09.006.

[62] Jian Ruan and Richard Burton. "Bulk Modulus of Air Content Oil in a Hydraulic Cylinder." In: (2016), pp. 1–11.

[63] Xueliang Li, Lu Zhang, Shujun Yang, and Nan Liu. "Analysis and experiment of HMT stationary shift control considering the effect of oil bulk modulus." In: 12.11 (2020), pp. 1–13. DOI: 10.1177/1687814020968324.

[64] Yash Girish Shah, Andrea Vacca, and Sadegh Dabiri. "Air release and cavitation modeling with a lumped parameter approach based on the Rayleigh–Plesset equation: The case of an external gear pump." In: *Energies* 11.12 (2018). ISSN: 19961073. DOI: 10.3390/en11123472.

[65] Thomas Ransegnola, Farshid Sadeghi, and Andrea Vacca. "An Efficient Cavitation Model for Compressible Fluid Film Bearings." In: *Tribology Transactions* 64.3 (2021), pp. 434–453. ISSN: 1547397X. DOI: 10.1080/10402004.2020.1853864.

[66] Paolo Casoli, Fabio Scolari, and Massimo Rundo. "Modelling and validation of cavitating orifice flow in hydraulic systems." In: *Sustainability (Switzerland)* 13.13 (2021), pp. 1–15. ISSN: 20711050. DOI: 10.3390/su13137239.

[67] Pen Olof Persson and Gilbert Strang. "A simple mesh generator in MATLAB." In: *SIAM Review* 46.2 (2004), pp. 329–345. ISSN: 00361445. DOI: 10.1137/S0036144503429121.

[68] Emiliano Mucchi, Giorgio Dalpiaz, and Alessandro Rivola. "Dynamic behavior of gear pumps: Effect of variations in operational and design parameters." In: *Meccanica* 46.6 (2011), pp. 1191–1212. ISSN: 00256455.

[69] T. Someya. *Journal Bearing Databook*. Berlin - Germany: Springer-Verlag, 1989.

[70] S. Chikamori and N. Yoshikawa. "Analysis of drive train noise and vibration." In: *International Journal of Vehicle Design* 2.4 (1981), pp. 408–427. ISSN: 01433369.

[71] Fazal U. Syed, Ming L. Kuang, and Hao Ying. "Active damping wheel-torque control system to reduce driveline oscillations in a power-split hybrid electric vehicle." In: *IEEE Transactions on Vehicular Technology* 58.9 (2009), pp. 4769–4785. ISSN: 00189545. DOI: 10.1109/TVT.2009.2025953.

[72] Junlong Qu, Wenku Shi, Juncheng Wang, and Zhiyong Chen. "Modeling and Analysis of Clutch Nonlinear Behavior in an Automotive Driveline for Suppressing Torsional Vibration." In: *Machines* 10.9 (2022), pp. 1–18. ISSN: 20751702. DOI: 10.3390/machines10090819.

[73] Yoshihito Kagawa, Iwao Hayashi, and Noboyuki Iwatsuki. "Application of FEM Modal Analysis to the Estimation of Sound Radiation Power." In: *Transactions of the Japan Society of Mechanical Engineers Series C* 63.615 (1997), pp. 3824–3831.

[74] Hans Peter Lahey, Christoph Steffens, and Christof Schultz. "Simulation method for geartrain NVH assessment and optimization." In: *SAE Technical Papers* 724 (2001). ISSN: 26883627. DOI: 10.4271/2001-01-1593.

[75] H Van der Auweraer, S Donders, R Hadjit, M Brughmans, P Mass, and J Jans. "New approaches enabling NVH analysis to lead design in body development." In: *New Technologies and Approaches to NVH Symposium* November (2005).

[76] S. Pakzad, A. K.S. Rajab, M. Mahboubkhah, M. M. Ettefagh, and O. Masoudi. "Modal analysis of the surface grinding machine structure through fem and experimental test." In: *Advanced Materials Research* 566 (2012), pp. 353–356. ISSN: 10226680. DOI: 10.4028/www.scientific.net/AMR.566.353.

[77] Philipp Kotter, David Morisco, Matthias Boesing, Oliver Zirn, Konrad Wegener, and Robert Bosch Gmbh. "Noise-Vibration-Harshness-Modeling and Analysis of a." In: (2017), pp. 1–4.

[78] Emiliano Mucchi, Alessandro Rivola, and Giorgio Dalpiaz. "Modelling dynamic behaviour and noise generation in gear pumps: Procedure and validation." In: *Applied Acoustics* 77 (2014), pp. 99–111. ISSN: 0003682X. DOI: 10.1016/j.apacoust.2013.10.007.

[79] Luca Guj, Theophane Courtois, and Claudio Bertolini. "A FE Based Procedure for Optimal Design of Damping Package, with Presence of the Insulation Trim." In: *SAE International Journal of Passenger Cars - Mechanical Systems* 4.2 (2011), pp. 1291–1303. ISSN: 19463995. DOI: 10.4271/2011-01-1693.

[80] Jun Lu, Zhenfei Zhan, Haozhan Song, Xu Liu, Xin Yang, and Junqi Yang. "Design Optimization of Vehicle Body NVH Performance Based on Dynamic Response Analysis." In: *SAE Technical Papers* 2017-March.March (2017). ISSN: 01487191. DOI: 10.4271/2017-01-0440.

[81] Kenneth A. Ramsey and Anthony Firmin. "Experimental Modal Analysis, Structural Modifications and Fem Analysis - Combining Forces on a Desktop Computer." In: *Proceedings of the International Modal Analysis Conference and Exhibit* February (1982), pp. 443–455.

[82] R. J. Allemang and D. L. Brown. "Experimental Modal Analysis Methods." In: *Handbook of Experimental Structural Dynamics*. Ed. by R. J. Allemang and Peter Avitabile. New York, NY: Springer New York, 2020, pp. 1–81. ISBN: 978-1-4939-6503-8. DOI: 10.1007/978-1-4939-6503-8_36-1.

[83] I. Bucher and D. J. Ewins. "Modal analysis and testing of rotating structures." In: *Philosophical Transactions of the Royal Society A: Mathematical, Physical and Engineering Sciences* 359.1778 (2001), pp. 61–96. ISSN: 1364503X. DOI: 10.1098/rsta.2000.0714.

[84] Yili Peng, Bin Li, Xinyong Mao, Hongqi Liu, Chao Qin, and Huanbin He. "A method to obtain the in-process FRF of a machine tool based on operational modal analysis and experiment modal analysis." In: *International Journal of Advanced Manufacturing Technology* 95.9-12 (2018), pp. 3599–3607. ISSN: 14333015. DOI: 10.1007/s00170-017-1405-8.

[85] Taylan Karaağaçlı and H. Nevzat Özgüven. "Experimental modal analysis of nonlinear systems by using response-controlled stepped-sine testing." In: *Mechanical Systems and Signal Processing* 146 (2021). ISSN: 10961216. DOI: 10.1016/j.ymssp.2020.107023.

[86] Emiliano Mucchi, Valerio Venturi, and Giorgio Dalpiaz. "A hybrid LP/FE model for the dynamic analysis of external gear pumps." In: *ASME International Mechanical Engineering Congress and Exposition, Proceedings* 9 PART C (2008), pp. 1523–1532. DOI: 10.1115/IMECE2007-41933.

[87] Antonino BONANNO and Francesca PEDRIELLI. "a Study on the Structureborne Noise of Hydraulic Gear Pumps." In: *Proceedings of the JFPS International Symposium on Fluid Power* 2008.7-3 (2008), pp. 641–646. DOI: 10.5739/isfp.2008.641.

[88] C. Tang, Y. S. Wang, J. H. Gao, and H. Guo. "Fluid-sound coupling simulation and experimental validation for noise characteristics of a variable displacement external gear pump." In: *Noise Control Engineering Journal* 62.3 (2014), pp. 123–131. ISSN: 07362501. DOI: 10.3397/1/376212.

[89] Eleonora Carletti, Giuseppe Miccoli, Francesca Pedrielli, and Giorgio Parise. "Vibroacoustic measurements and simulations applied to external gear pumps. An integrated simplified approach." In: *Archives of Acoustics* 41.2 (2016), pp. 285–296. ISSN: 01375075. DOI: 10.1515/aoa-2016-0028.

[90] Sangbeom Woo and Andrea Vacca. "Experimental characterization and evaluation of the vibroacoustic field of hydraulic pumps: The case of an external gear pump." In: *Energies* 13.24 (2020). ISSN: 19961073. DOI: 10.3390/en13246639.

[91] Toru Yamazaki and Eiichi Kojima. "Prediction of sound power radiated from oil hydraulic pump using FEM and BEM." In: *Acoustical Science and Technology* 24.2 (2003), pp. 103–105. ISSN: 13463969. DOI: 10.1250/ast.24.103.

[92] Y. Bousseau and L. Gagliardini. "Powertrain acoustic characterization at high frequencies: Acoustic source modeling based on sound intensity measurements." In: *SAE Technical Papers* May (2003). ISSN: 26883627. DOI: 10.4271/2003-01-1457.

[93] Timothy Opperwall and Andrea Vacca. "A combined FEM/BEM model and experimental investigation into the effects of fluid-borne noise sources on the air-borne noise generated by hydraulic pumps and motors." In: *Proceedings of the Institution of Mechanical Engineers, Part C: Journal of Mechanical Engineering Science* 228.3 (2014), pp. 457–471. ISSN: 09544062. DOI: 10.1177/0954406213486591.

[94] Taeho Kim and Monika Ivantysynova. "Active vibration control of swash plate-type axial piston machines with two-weight notch least mean square/filtered-x least mean square (LMS/FxLMS) filters." In: *Energies* 10.5 (2017). ISSN: 19961073. DOI: 10.3390/en10050645.

[95] Shaogan Ye, Junhui Zhang, Bing Xu, Wei Song, and Shiqiang Zhu. "A Hybrid Lumped Parameters/Finite Element/Boundary Element Model to Predict the Vibroacoustic Characteristics of an Axial Piston Pump." In: *Shock and Vibration* 2017 (2017). ISSN: 10709622. DOI: 10.1155/2017/3871989.

[96] Yang Pan, Yibo Li, Minghui Huang, Yashi Liao, and Dedong Liang. "Noise source identification and transmission path optimisation for noise reduction of an axial piston pump." In: *Applied Acoustics* 130.September 2017 (2018), pp. 283–292. ISSN: 1872910X. DOI: 10.1016/j.apacoust.2017.10.009.

[97] Andrea Gaiola, Barbara Zardin, Paolo Casoli, Massimo Borghi, Francesca Mazzali, Francesco Pintore, and Stefano Fiorati. "The Hydraulic Power Generation and Transmission on Agricultural Tractors: Feasible architectures to reduce dissipation and fuel consumption-Part i." In: *E3S Web of Conferences* 197.October (2020). ISSN: 22671242. DOI: 10.1051/e3sconf/202019707009.

[98] Paolo Casoli, Barbara Zardin, Salvatore Ardizio, Massimo Borghi, Francesco Pintore, and Davide Mesturini. "The Hydraulic Power Generation and Transmission on Agricultural Tractors: Feasible architectures to reduce dissipation and fuel consumption-Part 2." In: *E3S Web of Conferences* 197 (2020). ISSN: 22671242. DOI: 10.1051/e3sconf/202019707010.

[99] Sergio M. Savaresi, Francesco L. Taroni, Fabio Previdi, and Sergio Bittanti. "Control system design on a power-split CVT for high-power agricultural tractors." In: *IEEE/ASME Transactions on Mechatronics* 9.3 (2004), pp. 569–579. ISSN: 10834435. DOI: 10.1109/TMECH.2004.835334.

[100] Blake Carl, Monika Ivantysynova, and Kyle Williams. "Comparison of operational characteristics in power split continuously variable transmissions." In: *SAE Technical Papers* 724 (2006), pp. 776–790. ISSN: 26883627. DOI: 10.4271/2006-01-3468.

[101] Yu Xia and Dongye Sun. "Characteristic analysis on a new hydro-mechanical continuously variable transmission system." In: *Mechanism and Machine Theory* 126 (2018), pp. 457–467. ISSN: 0094114X. DOI: 10.1016/j.mechmachtheory.2018.03.006.

[102] Rolf Lasaar, Linde Hydraulics Gmbh, and Co Kg. "Development of a new hydrostatic motor in swashplate design Development of a new hydrostatic motor in swashplate design." In: November (2015).

[103] Paolo Casoli, Mirko Pastori, and Fabio Scolari. "Swash plate design for pressure ripple reduction - A theoretical analysis." In: *AIP Conference Proceedings* 2191.December (2019). ISSN: 15517616. DOI: 10.1063/1.5138771.

[104] Noah D. Manring. "The control and containment forces on the swash plate of an axial piston pump utilizing a secondary swash-plate angle." In: *Proceedings of the American Control Conference* 6 (2002), pp. 4837–4842. ISSN: 07431619. DOI: 10.1109/ACC.2002.1025424.

[105] J. M. Bergada, J. Watton, and S. Kumar. "Pressure, flow, force, and torque between the barrel and port plate in an axial piston pump." In: *Journal of Dynamic Systems, Measurement and Control, Transactions of the ASME* 130.1 (2008), pp. 0110111–01101116. ISSN: 00220434. DOI: 10.1115/1.2807183.

[106] George Maling, Walter Morrey, and William Lang. "Digital Determination of Third-Octave and Full-Octave Spectra of Acoustical Noise." In: *IEEE TRANSACTIONS ON AUDIO AND ELECTROACOUSTICS* 15.2 (1967), pp. 98–104. ISSN: 15237656.